An Experimental and Numerical Study of the Performance of Carbon Black Nanofluids in a Direct Absorption Solar Collector

Agathe Bjelland Eriksen

Master's Thesis in Energy
Integrated Master's Program in Energy at Geophysical Institute
with Specialization in Energy Technology

Department of Physics and Technology
University of Bergen

June, 2023

Acknowledgements

I would like to take this opportunity to thank all those who have supported me in my pursuit of the Integrated Master's Degree in Energy and helped make my time at the University of Bergen unforgettable.

First and foremost, I want to express my deep appreciation to my supervisor, Professor Pawel Kosinski at the Department of Physics and Technology at the University of Bergen, for his invaluable insight, support and guidance throughout the research process. His expertise, feedback, and optimistic outlook have been essential in bringing this thesis to completion.

I would also like to give a heartfelt thanks to my classmates from the Master's Program of Energy at the Geophysical Institute for the amazing journey we have shared together. A special thanks is deserved to my friends Marte, Tora, and Linna from Sal 363 at the Department of Physics and Technology for unwavering support, companionship, and encouragement during this journey. Their feedback and insight have been vital in keeping me motivated and improving the quality of my work.

Lastly, I want to extend deep gratitude to my parents, who have always believed in me and encouraged me in every decision I have made. I am forever grateful to them.

Bergen, June 2023

Agathe Bjelland Eriksen

Abstract

Increasing global climate challenges cause for better utilization of renewable energy resources. Existing solar photovoltaic and solar thermal systems suffer from insufficient solar absorption and high heat loss, resulting in low system performance. Research has suggested that introducing nanofluids in solar collectors could enhance the efficiency of the system, as the thermophysical and optical properties of the working fluid are elevated.

In this study, an experimental and numerical assessment of the performance of carbon black nanofluids in a direct absorption solar collector was executed. A laboratory setup was constructed so that the efficiency of different concentrations of nanoparticles could be investigated and compared under the same conditions. Unlike traditional direct absorption solar collectors, the laboratory set-up in the present work utilized stationary nanofluids for solar absorption. Two nanofluid concentrations were also compared by computational fluid dynamics simulations of the thermal enhancement in a simplified geometry.

The results showed improved efficiencies for nanofluids of all concentrations in the experimental and numerical investigation. Among the six nanofluids in the experimental analysis, ranging from 0.0015-0.05 wt.%, the superior concentration was 0.01 wt.% with a thermal enhancement of 40.4 $\pm$ 3.86% compared to reference distilled water values. The numerical results showed thermal enhancement of 7.43% and 5.16% for a concentration of 0.0015 wt.% and 0.005 wt.%, respectively. Overall, the results revealed great potential for exploiting nanofluids, even at very low volume fractions, in heat transfer applications to enhance performance. At larger volume fractions, however, shortcomings such as large heat loss prove to still pose a challenge.

Contents

List of Figures

List of Tables

List of Symbols and Notations

List of Abbreviations

CB	Carbon Black
CFD	Computational Fluid Dynamics
DASC	Direct Absorption Solar Collector
FPSC	Flat Plane Solar Collector
MWCNT	Multi-walled Carbon Nanotube
NF	Nanofluids
NP	Nanoparticles
SDS	Sodium Dodecyl Sulfate
SPV	Solar Photovoltaic
STE	Solar Thermal Energy

Nomenclature

α	Absorptivity	
$\bar{V}$	Average velocity	$[\mathrm{ms}^{-1}]$
δ_f	Fluid layer thickness	[m]
$\dot{m}$	Mass flow rate	$[\mathrm{kgs}^{-1}]$
η	Thermal enhancement	
η_{eff}	Thermal efficiency	
μ	Dynamic viscosity	$[\mathrm{Pa} \cdot \mathrm{s}]$
ϕ	Particle volume fraction	
ρ	Density	$[\mathrm{kgm}^{-3}]$
σ	Stefan-Bolzmann constant $= 5.672 \cdot 10^{-8}$	$[\mathrm{Wm}^{-2}\mathrm{K}^{-4}]$
ε	Emissivity	
A	Area	$[\mathrm{m}^2]$
C_p	Specific heat capacity	$[\mathrm{kJkg}^{-1}\mathrm{K}^{-1}]$
D	Diameter	[m]
E_{abs}	Absorbed radiation power	$[\mathrm{Wm}^{-2]}$
E_V	Emitted radiation power	$[\mathrm{Wm}^{-2]}$
F	View factor	
f	Fanning friction factor	
g	Gravitational acceleration	$[\mathrm{ms}^{-2}]$

H	Height distance	[m]
h	Heat transfer coefficient	[$\mathrm{Wm^{-2}K^{-1}}$]
h_f	Friction loss	[$\mathrm{Jkg^{-1}}$]
I	Radiation intensity	[$\mathrm{Wm^{-2}}$]
K	Extinction coefficient	[$\mathrm{m^{-1}}$]
k	Thermal conductivity	[$\mathrm{Wm^{-1}K^{-1}}$]
L	Characteristic length	[m]
m	Mass	[kg]
Nu	Nusselt number	
p	Pressure	[Pa]
PP	Pumping power	[W]
Q	Heat	[J]
q	Rate of heat flow	[W]
q_r	Rate of radiation	[W]
Re	Reynolds number	[m]
S	Standard deviation	
T	Temperature	[K]or[$^\circ$C]
V	Volume	[$\mathrm{m^3}$]
x	Propagation length in x-direction	[m]
Z	Elevation	[m]

Subscript

bf	Base fluid
c	Solar collector
f	Fluid
i	Inlet
nf	Nanofluid
np	Nanoparticles
o	Outlet
s	Surface
w	Wall

Chapter 1

Introduction

1.1 Motivation

Human activities over the last centuries have led to global warming and a deteriorated Earth vulnerable to a pressing climate crisis. Decades of overconsumption without consideration of sustainability has made it economically favorable with fossil fuel employment and has essentially created a *Tragedy of the Commons*. Human-caused emissions of greenhouse gases, particularly carbon dioxide (CO_2) and methane (CH_4), have thereby increased the global surface temperature of the Earth by 1.1 °C since 1900. These emissions are expected to persist and intensify in the future, resulting in further temperature increases in the years to come [1]. The effects of this warming are already evident and will escalate at an alarming rate unless immediate and drastic changes are made.

At the same time as the climate crisis is in full effect, the world's demand for energy is only growing larger [2]. Moreover, with increased prosperity, the average population is continuously becoming older, and the world's population is assumed to reach 8.5 billion in 2030 [3]. However, efforts are being made among policy-makers for a green transition. Fit for 55, Paris Agreement, and RePowerEU are important plans and targets to accelerate the green shift in the upcoming years. In light of the current European energy crisis, the motivation for a rapid energy transition is more significant than ever, and many of the proposed solutions coincide with the determined climate targets. Could this mean the start of a turning point within the green transition?

To reach the world's ambitious climate targets, a renewable energy mix where all available energy sources are exploited simultaneously is essential. With the incoming solar energy reaching the Earth‘s surface every day being 200 000 times greater than the world‘s daily electric-generating capacity, solar energy is one of the renewable energy sources with significant untapped potential [4]. Furthermore, the cost of producing solar power has also drastically decreased in the later years, causing solar to become the lowest cost power generation technology available today [5–7].

The two main ways to harvest solar energy are by solar photovoltaic (SPV) and solar thermal energy (STE) systems [8]. These methods differ in the way they produce energy. While SPV converts solar radiation into electrical energy, STE systems produce thermal energy that generates electricity or heat. SPV systems are versatile as they can power several different applications through the produced electricity, and compared to solar thermal systems, they are often simpler if the end goal is electricity production [9]. On the other hand, STE has the benefit of energy storage since the hot working fluid can be stored in a tank for some time with limited energy loss. Furthermore, these systems are less complex for domestic use than SPV.

Solar thermal energy systems can be divided into two types [8], hereby concentrating or non-concentrating types, which are used for electricity production and heat generation, respectively. For many applications, such as domestic hot water heating, space heating, or agricultural applications, collecting the incident solar radiation as heat through non-concentrating systems is beneficial. For this, solar collectors are used, which can convert solar energy into heat [10]. More specifically, a solar collector is a device designed to absorb the energy in incoming solar radiation as heat by an absorbing material. Traditionally, the absorbing material is a solid, and the heat is then transferred to an absorber fluid, thereby increasing the fluid's internal energy, which can be used for further domestic use [11].

Solar collectors can be segregated into surface absorbers and volumetric absorbers [12]. The surface absorbers use a conductive surface metal to absorb the incident solar radiation and convert it into heat. The heat energy is then transferred to a working fluid by conduction and convection. These solar absorbers experience shortcomings such as significant heat loss, corrosion effects, and low conversion efficiency [13]. In volumetric solar absorbers, the absorbing surface is eliminated as the working fluid directly absorbs the solar energy. This results in a reduction in heat loss, and the system's efficiency is only dependent on the absorption ability of the working fluid. The two collector types are illustrated in Fig. 1.1.

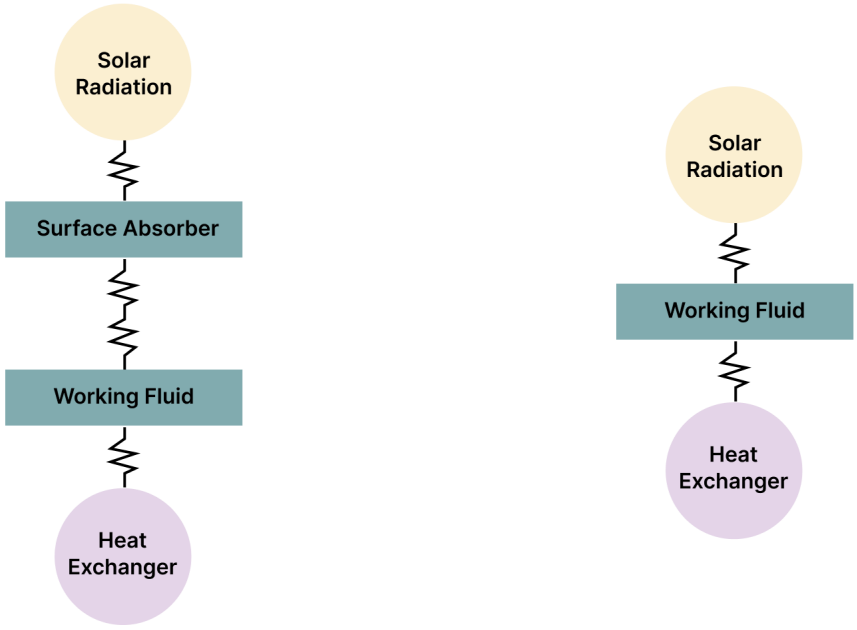

(a) Surface absorber solar collector. (b) Volumetric absorber solar collector.

Figure 1.1: Two types of solar collectors. Inspired by Goel et al. [12].

The most common and cost-effective solar collectors are flat plane solar collectors (FPSC) [14]. These are examples of conventional surface collectors that typically use a black surface to absorb solar energy. However, these collectors suffer from corrosion effects, limitations on incident flux density, and significant heat loss, leading to low efficiency and outlet temperature. The shortcomings with FPSC have led to a new type of solar collector, the direct absorption solar collector (DASC) [14]. DASC stands out from FPSC as it is a volumetric absorption collector that enables the working fluid to directly absorb solar radiation. The direct absorption of incident solar energy minimizes the mentioned limitations associated with FPSC, as the design is less complex. Fig. 1.2 showcases a typical DASC configuration.

However, the goal of solar collectors is not only to minimize heat loss but also to maximize absorption. Traditionally, the working fluid of solar collectors has been fluids such as water, ethylene glycol, etc., that have good heat transfer properties [8]. During their experiment on optical properties for direct absorption solar thermal systems, Otanicar et al. [16] found that water had the best absorption among four typical working fluids. However, water was still found to be a weak absorber, only able to absorb 13% of the incoming energy. Alternative fluids with increased

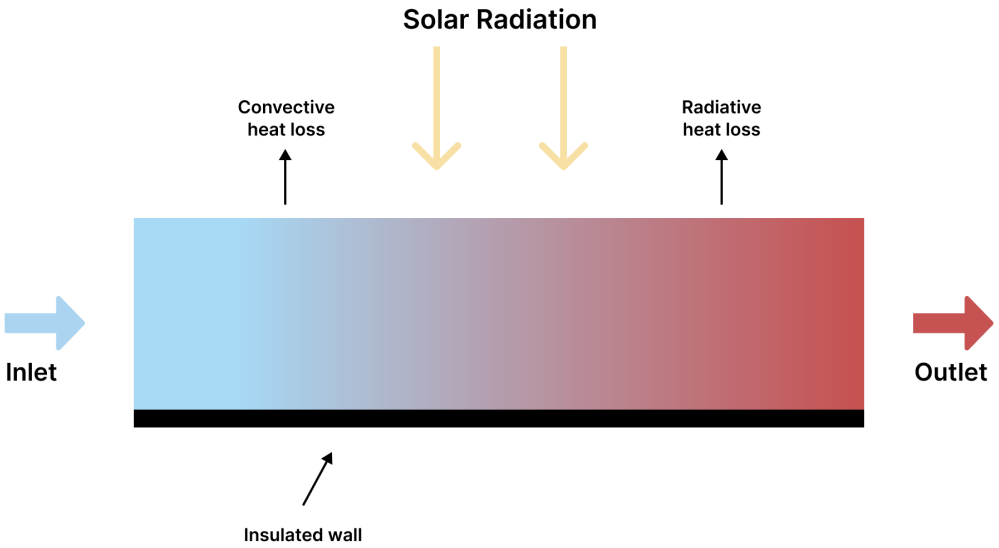

Figure 1.2: Schematic of DASC. Inspired by Qin et al. [15].

absorption abilities have lately been investigated. Mainly, the focus has been on dispersing different nanoparticles (NP) in the traditional base fluids to improve their absorption properties. By adding nanoparticles to the fluid or utilizing so-called nanofluids (NF), scattering of the incident solar energy within the fluid is increased, and accordingly, the absorption of energy [17].

Moreover, utilizing nanoparticles in the working fluid has been demonstrated to elevate a range of thermophysical properties. For instance, inadequate thermal conductivity in the working fluid is an obstacle encountered in numerous industrial applications, resulting in reduced energy efficiency [18]. Through the employment of this new type of working fluid, enhancement in thermal conductivity, thermal diffusivity, convective heat transfer coefficient, and other thermophysical properties have been observed, thereby improving the system's overall efficiency [19].

Nanofluids have potential within a range of applications. Their enhanced heat transfer properties make them promising coolants in various sectors such as electronics, heavy-duty transport, or industrial processes [19]. Their small size and large surface area also make them interesting within the chemical and pharmaceutical industries. When considering improvements within the energy sector, nanofluids have the potential to play a significant role in areas such as energy conversion, storage, and saving. By incorporating nanoparticles into the working fluid of energy systems, more energy can be captured by the improved optical properties of the fluid, elevating the energy conversion of these systems. In energy

storage applications, improved thermophysical properties make them a prominent competitor to traditional heat transfer fluids. Finally, processes exploiting heat exchangers could experience large energy savings by adding nanoparticles to the working fluids.

Nanofluids have been considered to have remarkable potential in enhancing energy efficiency in all of the mentioned applications. The focus of this thesis is the utilization of nanofluids for energy conversion and saving. Specifically, the present work will look into applying nanofluids in a direct absorption solar collector to understand how nanofluids can play a role in the future of solar energy systems.

1.2 Objective

This thesis aims to investigate the performance of stationary nanofluids with different volume fractions of carbon black (CB) nanoparticles as an absorbing fluid in a direct absorption solar collector.

More specifically, this thesis seeks to:

- Create an experimental setup for repeatable and reliable laboratory experiments of a DASC.
- Create a simulation setup in computational fluid dynamics software Simcenter STAR-CCM+ for numerical analysis of a DASC.
- Understand the effect of solid nanoparticles on the optical and thermophysical properties of the fluid.
- Investigate how these properties change with nanoparticle concentration and design.
- Comprehend the potential and challenges with nanofluids in future applications.

Chapter 2

Theory

This chapter provides the theoretical background necessary to understand the utilization of nanofluids as a working fluid in a DASC. In the first section, an introduction to nanoparticles and nanofluids, as well as the stability associated with these, is given. Next, a brief literature review of relevant work in the field of nanofluid and DASC research is offered. The following section is dedicated to the basics of thermal physics as an introduction to heat transfer, which is the essence of this thesis. A short description of fluid mechanics and a section on how to investigate system performance are also included. Finally, the basic theory associated with computational fluid dynamics is explained to lay the foundation for the simulation work later presented.

2.1 Nanofluids

A nanofluid can be defined as a base fluid containing suspended nano-sized particles [11]. The suspended particles can be metal/nonmetals/metal oxides of different particle sizes within the range of 1-100 nm [10, 20]. The options for base fluid are endless, but typical choices are water, mineral oils, or glycol because of their heat transfer properties. Nanofluids can be used as a working fluid in a wide range of applications and industries. However, interest has been specially raised within heat transfer applications as it is suggested that they possess enhanced thermophysical properties [19, 21, 22]. More specifically, replacing traditional working fluids, like water or oil, with nanofluids could increase the thermal conductivity, thermal diffusivity, extinction coefficient, and convective heat transfer coefficient of the fluid [19, 23–25], thereby increasing the efficiency of the system. This stems from the

fact that heat transfer occurs on the surface of particles [11], and since nanoparticles have increased surface area, the rate of heat transfer is improved.

The effectiveness of nanofluids as an absorbing and working fluid in heat transfer applications depends on several factors. Features such as the particle material, base fluid material, particle shape and size, particle volume fraction, and nanofluid stability are essential to the overall collector efficiency of the application [11, 23]. Extensive research has been conducted to study the influence of each parameter on nanofluids' heat transfer abilities. Most research is promising and gives nanofluids an optimistic role in the future of heat transfer applications. However, there are still challenges and uncertainties related to their behavior and properties. Among others, a deeper understanding of the long-term stability, their optical and rheological properties, and the cost-effectiveness and scalability of nanofluid systems is needed.

2.1.1 Stability of Nanofluids

When working with nanofluids, one of the critical challenges is the stability of the fluid. Here, stability is defined as a significantly low rate of aggregation of the solid particles in the fluid [19]. Sufficient stability is important as it affects fluid characteristics such as thermal conductivity, viscosity, and heat transfer efficiency. Increased stability by inhibiting agglomeration is therefore crucial for the overall performance of the system. The agglomeration is a consequence of the inter-particle van der Waals forces that dominate the repulsive forces between the particles [26, 27]. Because of the large surface-to-volume ratio of nanoparticles, the particles possess greater surface energy, which causes a higher tendency to agglomerate [20].

An easy and cost-effective way of enhancing the stability of nanofluids is by adding surfactants to the system [11, 20, 25]. Surfactants are amphiphilic compounds consisting of a hydrophilic polar head and a hydrophobic tail [28]. When absorbed at the interface between the solid and the liquid particles in the fluid, the surfactants decrease surface and interfacial tension by creating electrostatic repulsion [27]. This promotes a level of uniformity and consistency of the nanoparticles dispersed in the base fluid, thereby increasing the system's stability. Surfactants can be divided into four classes according to their hydrophilic group [19, 28]. These are anionic, non-ionic, cationic, and amphoteric surfactants. Which surfactant is suitable depends on the nanoparticle's surface charge and the base fluid type.

In the experiments in this thesis, sodium dodecyl sulfate (SDS) was used as a surfactant. This is one of the most widely used ionic surfactants. Other impor-

tant surfactants are salt and oleic acid, dodecyltrimethylammonium, and hexadecyltrimethylammoniumbromide [25]. However, it must be noted that surfactants are not a favorable solution for increased stability in systems with high temperatures. The bond between the surfactant and the nanoparticles can be damaged in these environments, resolving in lower efficiencies. Other methods that can increase stability are surface modification techniques, pH control of the nanofluids, magnetic stirrer, high-pressure homogenizer, or ultrasonic agitation [25, 27]. The addition of SDS to the fluid was used to prevent agglomeration in this thesis.

As of today, the most elementary and common way to measure the stability of nanofluids is by visual inspection (sedimentation) [25]. According to research, the fluid is considered stable if the concentration of the supernatant particles remains constant with time. Other applicable methods include measuring Zeta potential, centrifugation method, and spectral analysis. In this thesis, stability was determined by visual inspection of the fluids.

2.1.2 Basic Properties of Nanofluids

Density

Density is one of the most fundamental and important physical properties of any material and is defined as the mass of the material per unit volume [29]. Generally, the theoretical research on the density of nanofluids is limited, but it is agreed upon that the addition of nanoparticles to a base fluid present increased density of the fluid [30]. The final density of the nanofluid can be assumed to be a mixed property of the density of the nanoparticles ρ_{np} and the base fluid ρ_{bf} [20, 26, 31]. By the most commonly used model in the literature, the density can then be calculated by

$$\rho_{nf} = \phi \cdot \rho_{np} + (1 - \phi) \cdot \rho_{bf}. \tag{2.1}$$

Here, ϕ is the particle volume fraction, defined as

$$\phi = \frac{V_{np}}{V_{np} + V_{bf}} \approx \frac{V_{np}}{V_{bf}}. \tag{2.2}$$

V_{np} and V_{bf} represent the volume of nanoparticles and base fluid, respectively. The linear model has been demonstrated to be consistent with experimental results.

However, other models are also available for more specific conditions, such as a given temperature or chemical composition.

Viscosity

Viscosity is a fluid's resistance to movement or change [32]. Nanofluids with suspended solid particles have a higher viscosity than the adjacent base fluid [33], which will affect the pressure drop and required pumping power in fluid flow systems. Understanding how the viscosity changes with the addition of nanoparticles is, therefore, important when developing thermal systems with nanofluids as the working fluid.

There are several existing models for estimating the viscosity of nanofluids. The most referred equation is also the pioneer theory, the Einstein model. The model assumes spherical particles and dilute fluids with low concentrations ($\phi \leq 2\%$), so the particles are not in contact with each other. For such a case, the viscosity can be predicted by [30, 33]

$$\frac{\mu_{nf}}{\mu_{bf}} = [1 + 2.5\phi], \tag{2.3}$$

where μ_{nf} and μ_{bf} are the viscosities of the nanofluid and base fluid, respectively. As seen from the linear model, the addition of nanoparticles to the fluid results in a higher viscosity. For fluids with larger volume fractions of particles, the interaction between the particles will affect the viscosity of the mixture [30]. Batchelor et al. [34] proposed a model valid for volume fractions up to 15%, which reflects the Brownian motion of the particles:

$$\frac{\mu_{nf}}{\mu_{bf}} = [1 + 2.5\phi + 6.2\phi^2]. \tag{2.4}$$

2.1.3 Specific Properties of CB Nanoparticles

Numerous researchers have investigated the performance of nanofluids in solar collectors, and a large number of different nanomaterials have been tested. This thesis focuses on carbon black nanoparticles, as research has suggested that carbon nanomaterials have high potential in solar utilization applications. Among other properties, the particles possess higher thermal conductivity and heat transfer coefficient compared to other nanomaterials [8], thus increasing the efficiency of the

heat applications. It was shown by Han et al. [35] that there exists a nearly linear correlation between the volume fraction and thermal conductivity of CB.

In their study, Han et al. also pointed out the noticeable absorption abilities of CB NFs. They found that CB has good absorption in the whole range of sunlight. As illustrated in Fig. 2.1, carbon black nanofluids have a much lower transmittance than water for wavelengths ranging from 200 to 1400 nm. Also for wavelengths longer than 1400 nm, CB NFs exhibit excellent absorption. This way, CB NFs will better exploit incoming solar radiation than traditional heating fluids such as water.

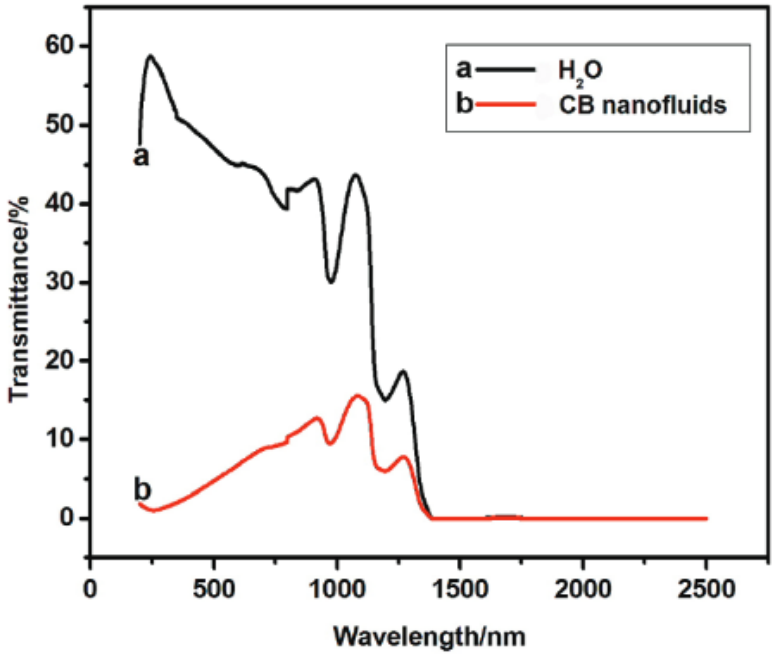

Figure 2.1: UV-Vis-NIR transmittance spectra for a) water and b) carbon black nanofluids. Reproduced from Han et al. [35].

Additionally, carbon nanomaterials exhibit a lesser density and smaller size than other alternatives, making them easy to handle and transport [8]. Combined with elevated stability and low erosion and corrosion effects, CB is a prominent material in solar collectors.

2.2 Literature Review

The following section presents some of the progress made in the field of nanofluids, with emphasis on the recent developments regarding nanofluids in DASC and CB NFs as working fluids.

The concept of utilizing fluids with suspended particles to augment thermophysical properties has been previously explored. Specifically, the use of micron-sized particles in heat transfer applications has been a subject of long-standing research interest. However, problems with erosion, clogging, increased pumping power, and poor stability caused by the size of these particles led to the development of a new class of working fluids [12, 17, 26, 35]. The subject of nanofluids was first explored in 1995 by Choi and Eastman, who suggested that suspending nano-sized metallic particles in conventional heat transfer fluid would increase the thermal conductivity of the fluid [18]. Since the surface area of nanoparticles is 1000 times greater than that of microparticles [11], and heat transfer occurs on the surface of the particles, the higher surface area of nanoparticles compared to microparticles would be able to enhance heat conduction in these fluids. This way, the nano-sized particles not only had the potential to reduce erosion and clogging, decrease pumping power, and reduce the inventory of heat transfer fluid but also significantly save energy by increasing the efficiency of heat applications [11, 25].

Since Choi and Eastman first suggested that the suspension of nano-sized particles in a base fluid would increase the thermal conductivity in heat transfer applications, extensive research has been conducted. In later years, research has also increased in relation to nanofluids in DASC. The concept was first suggested by Tyagi et al. [14], who theoretically predicted the efficiency of a low-temperature DASC utilizing nanofluids and compared this to traditional FPSC. The authors found that the presence of nanoparticles, in this case, aluminum particles, increased the absorption of incident solar radiation by more than nine times over pure water. The research also indicated an increased efficiency of 10% (on an absolute basis) of a DASC using nanofluids compared to an FPSC under the same conditions.

Otanicar et al. [36] experimentally and numerically investigated the effect nanofluids have on the efficiency of a direct absorption solar collector. Experiments with volumetric absorption of incident solar radiation showed a 5% enhancement in the efficiency of the DASC when utilizing nanofluids. Three different nanomaterials suspended in water were considered, hereby carbon nanotubes, graphite (CNT), and silver. For all materials, results showed an initial increase in efficiency with increased volume fraction. At volume fractions above 0.5 vol%, the efficiency

slightly decreased before leveling out. Further, the results revealed the significant effect of nanoparticles' size, shape, and volume fraction on widening the spectral absorption of solar energy throughout the absorbing fluid [17].

Studies have also been conducted on the efficiency of nanofluids in parabolic trough collectors (PTC), another form of concentrating solar collector. Through experiments using TiO_2/water nanofluids in a PTC, Kasaeian et al. [37] found up to 9% enhancement in thermal efficiency compared to traditional fluids. In another study, comparing a DASC with a conventional PTC, Khullar et al. [20] found 5 to 10% thermal efficiency enhancement in the DASC, making DASC an interesting alternative to PTC.

The optical and thermal properties of nanofluids in a DASC were explored by Karami et al. [38]. Experiments measured the incident radiation absorbed by functionalized CNT (f-CNT) nanoparticles dispersed in water. The research confirmed elevated optical properties due to the improvement of light extinction levels, even at low volume fractions. A significant increase in thermal conductivity was also registered. At a concentration of 150 ppm f-CNT, the increase in extinction coefficient of pure water was about 4.1 cm^{-1} while the thermal conductivity was enhanced by 32.2%. The research agrees with the findings by Taylor et al. [39], who found that over 95% of sunlight could be absorbed by a nanofluid with an extremely low volume fraction of nanoparticles.

Similar results were found during Ladjevardi et al. [40] evaluation of the direct absorption of solar radiation in a volumetric solar collector using graphite nanofluids. The results revealed more than 50% absorption of incident solar radiation using a low graphite volume concentration of 0.000025 vol%, compared to absorption of 27% for pure water. Through numerical analysis, Luo et al. [41] assessed the performance of a DASC using different nanofluids (graphite, long and short CNTs, SiO_2, Ag, and Cu). Their analysis predicted the photothermal efficiency by a simulation model that combines the radiative heat transfer in particulate media with conduction and convection heat transfer in the DASC collector. The simulation results showed an improved outlet temperature and efficiency of 30-100 K and 2-25% compared to the base fluid. The study concluded that even low concentrations of graphite have good solar absorption abilities, thereby the potential to enhance system efficiencies.

Several different nanofluids have been researched as solar absorption efficiency enhancers in solar thermal systems. In their experiments with carbon black nanofluids in a DASC, Han et al. [35] found CB NPs to have good solar absorption abil-

ities. The results showed increased temperature with CB NFs compared to both pure water as well as nanofluids such as TiO_2/water, SiO_2/water, and ZrC/water. The CB NPs also showed very good absorption abilities in the whole UV-Vis-NIR absorption spectra. Enhanced properties were found in the wavelength ranging from 200 to 1,400 nm compared to pure water. Further, the experiments indicate a nearly linear increase in thermal conductivity with the increase of volume fraction and temperature of CB.

In summary, research conducted in recent years shows great potential for exploiting nanofluids in solar thermal applications in order to increase system efficiency. Properties such as spectral absorption and thermal conductivity are improved compared to traditional working fluids, thus optimizing heat transfer and reducing energy consumption. Future work is still necessary to reduce costs and increase the technological readiness level, where investigation of the effect of concentration, system development, and chemical composition of the working fluid on the overall performance are some interesting aspects.

2.3 Thermal Physics

2.3.1 Heat Transfer

From the first law of thermodynamics, it is stated that energy transfer takes place between a body and a surrounding medium of a different temperature until thermal equilibrium is reached [42]. The transfer of energy will always be directed from the higher temperature to the lower temperature. Here, energy transfer happens in the form of heat, which is defined as "the form of energy that is transferred between two systems (or a system and its surroundings) by virtue of a temperature difference." Heat may flow by three different mechanisms: conduction, convection, and radiation [43]. All three mechanisms require a temperature difference and are directed from high to low temperatures.

Conduction

Conduction is heat transfer as a result of interactions between particles with different energy content. This form of heat transfer can take place in solids, liquids, or gases. The heat flow caused by conduction is unaccompanied by any observable motion of matter [42]. The rate of heat conduction is given by Fourier's law

$$\frac{\mathrm{d}q}{\mathrm{d}A} = -k\frac{\mathrm{d}T}{\mathrm{d}x}, \tag{2.5}$$

where q is the rate of heat flow in the direction normal to a surface, A is the surface area, T is temperature, and x is the distance normal to the surface [43]. The thermal conductivity is given by k and is a measure of the ability of a material to conduct heat [42]. As seen from the equation, the rate of heat conduction in a direction is proportional to the temperature gradient in the same direction. Since heat is transferred in the direction of decreasing temperature, a negative sign is included in the equation so that the heat transfer is positive in the positive x direction.

Convection

Heat transfer between a solid surface and an adjacent liquid or gas in motion is called convection [42]. The two types of convection are natural and forced. Heat transfer is called forced if the fluid flow is forced by an external force such as a pump or fan. If buoyancy forces cause the fluid motion led on by density differences due to the variation in temperature, the action is natural convection. The convective flux is given by Newton's law of cooling

$$\frac{q}{A} = h_c(T_s - T_f). \tag{2.6}$$

Here, T_s is the surface temperature, T_f is the bulk temperature of fluid far from the surface, and h_c is the convection heat transfer coefficient. The heat transfer coefficient is a theoretically or experimentally determined parameter that depends on the system variables that influences convection. The coefficient can be expressed in relation to the dimensionless Nusselt number, Nu, which is the ratio between the convective heat transfer to the conductive heat transfer across a fluid [43]. The local Nusselt number is expressed as

$$\mathrm{Nu} = \frac{h_c L}{k}, \tag{2.7}$$

where L is a characteristic length, and k is the thermal conductivity. If the convective heat transfer is to a Newtonian fluid with a fully developed laminar flow inside a pipe, the Nusselt number is expressed with the film coefficient, h_i. This is a measure of the ability of the solid pipe surface to transfer heat to the fluid. The new expression for the Nusselt number then becomes [43]

$$\mathrm{Nu} = \frac{h_i D_i}{k}. \tag{2.8}$$

Here D_i is the inner diameter of the pipe. In the case of a constant wall temperature, the film coefficient is given by

$$h_i = \frac{\dot{m} C_p}{\pi D_i L} \ln\Big[\frac{T_w - T_i}{T_w - T_o}\Big], \tag{2.9}$$

where $\dot{m}$ is the mass flow rate of the fluid, C_p is the specific heat capacity, and T_w, T_i, and T_o are the wall temperature, inlet temperature, and outlet temperature, respectively.

Radiation

All bodies with a temperature above absolute zero (0K) emit thermal radiation in the form of electromagnetic waves [43]. Thermal radiation is mostly electromagnetic radiation in the infrared region and does therefore not include radiation such as x-ray or gamma-rays [44]. Unlike conduction and convection, radiation can be transferred without any medium. Also, in contrast to the other two modes of heat transfer, radiation can occur between two bodies separated by a colder medium. Radiance from the sun to the earth is such an example.

The absolute maximum radiation a body can emit to its surrounding is proportional to the fourth power of the absolute temperature and is given by the Stefan-Boltzmann law

$$q_r = \sigma A T^4, \tag{2.10}$$

where q_r is the rate of radiation, σ is the Stefan-Boltzmann constant and equal to $5.67 \cdot 10^{-8}$ W/(m$^2\cdot$ K^4) and T is the absolute temperature of the surface. The Stefan-Boltzmann law equals the radiation from an ideal blackbody that emits the maximum rate of radiation. However, real surfaces radiate less heat than a theoretical blackbody and are therefore called grey bodies. The effectiveness of a surface in emitting energy is called emissivity, ε. This property is in the range $0 \leq \varepsilon \leq 1$, where $\varepsilon = 1$ defines a blackbody. When including the emissivity of a surface, the rate of radiation becomes

$$q_r = \varepsilon \sigma A T^4. \tag{2.11}$$

From Eq. (2.11), the net radiational heat transfer between two surfaces can be defined. The net heat transfer from body 1 to body 2 is defined as

$$q_{1\to 2} = \varepsilon \sigma A_1 F_{1\to 2}(T_1^4 - T_2^4), \tag{2.12}$$

where A_1 is the surface of body 1, and $F_{1\to 2}$ is the view factor, that is the fraction of radiation from body 1 falling on body 2. T_1 and T_2 is the temperature of body 1 and body 2, respectively.

2.3.2 Thermal Properties of Fluids

Specific Heat Capacity

Specific heat capacity is a thermophysical property that affects a fluid's ability to transfer heat [20]. More specifically, the property is defined as the amount of energy required to raise the temperature of a unit mass of a substance by one degree [42]. A high specific heat capacity means that the substance can absorb more heat per unit mass without a significant increase in temperature. This is often desired in heat transfer applications, as a fluid with high specific heat capacity will be able to absorb and dissipate large amounts of energy while minimizing temperature differences. The specific heat capacity of nanofluids depends on the specific heat capacity of the base fluid, $C_{p,bf}$, the specific heat capacity of the nanoparticles, $C_{p,np}$, density, ρ, and the volumetric concentration of nanoparticles, ϕ, and is given by [20, 31]

$$C_{p,nf} = \frac{\phi \cdot (\rho C_{p,np}) + (1-\phi) \cdot (\rho C_{p,bf})}{\rho_{nf}}. \tag{2.13}$$

This is the so-called thermal equilibrium model. Other models for calculating the specific heat capacity of nanofluids are also available, but common for several of them are significant deviations between the model and experimental results. Heat capacity is dependent on temperature, phase, and chemical composition [45]. In Table 2.1, some specific heat capacities of different substances under standard conditions are listed. The high specific heat capacity of water is the reason why water plays an important role in many thermal energy systems.

Table 2.1: Some specific heat capacities at 25°C [45, 46]. Unit is [kJ/kg K].

Substance	**Phase**	**Specific Heat Capacity**
Steel	Solid	0.466
Uranium	Solid	0.116
Air	Gas	1.0035
Ethanol	Liquid	2.44
Water	Liquid	4.18

In their study on the effect of different specific surface areas on the properties of nanofluids, Sobczak et al. [47] experimentally found the specific heat capacity of two distinct carbon black nanoparticles to be 1.017 kJ/kg K and 1.148 kJ/kg K at a temperature of 25 °C. Other reported values for similar compounds are 0.716 kJ/kg K for amorphous carbon [48] and 0.770 kJ/kg K for dense graphite [49]. The difference in values highlights the considerable variance in specific heat capacity that exist across different nanoparticle compounds and underscores the dependence of nanofluid specific heat capacity on the type of nanoparticle employed.

Thermal Conductivity

Thermal conductivity, denoted k, is the ability of a material to conduct heat [42]. The conductivity of a material differs depending on the chemical composition and temperature, and the value is larger for materials that transfer heat well and lower for materials that transfer heat poorly.

The general agreement in the literature is that nanofluids exhibit higher thermal conductivity than their associated base fluids [8, 19, 21]. In their experimental study on the thermal conductivity of ethylene glycol-based nanofluids with 0.07 vol% hybrid graphene carbon nanotubes, Van Trinh et al. [50] found an increased conductivity of 18% and 50% at 303 K and 323 K, respectively. Khosrojerdi et al. [51] also reported an intensification in thermal conductivity during their experiments with graphene oxide nanoplatelets dispersed in deionized water as the working fluid in a DASC. The research emphasizes that the augmentation of thermal conductivity was impacted by the chemical composition and temperature of the fluid, as shown in Fig. 2.2.

The thermal conductivity augmentation could be caused by several factors. Some authors ascribe the enhancement to the intensified turbulence and energy transfer between particles caused by the increase in Brownian motion [8]. Others propose a thicker interfacial layer or nanoparticle clustering as the responsible factor. The disagreement in the literature on the mechanisms responsible for the enhancement

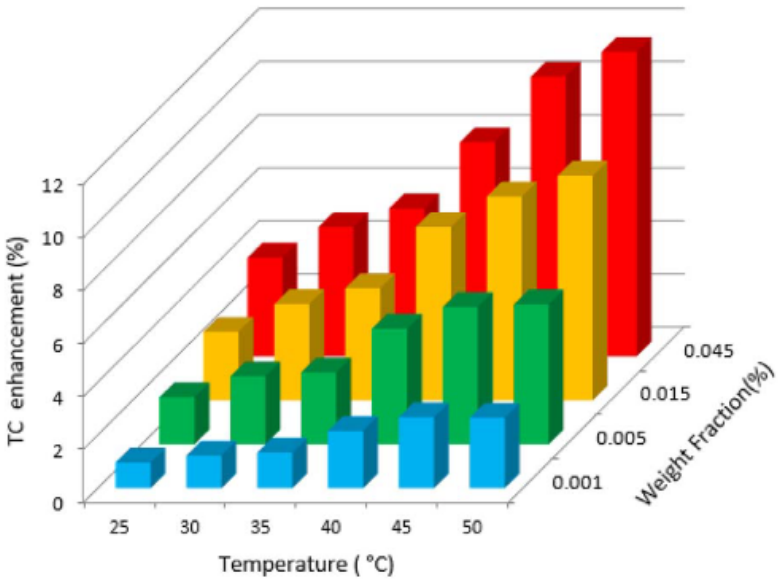

Figure 2.2: Increased thermal conductivity of nanofluids considering weight fractions and temperatures in the range 25-50 °C. Reproduced from Khosrojerdi et al. [51].

highlights the requirement for more research and understanding of this property in future work.

One of the proposed expressions for predicting the thermal conductivity of nanofluids is the Maxwell theory. Using this approach, the conductivity of nanofluids is determined based on the thermal conductivity of the base fluid, k_{bf}, the thermal conductivity of the nanoparticles, k_{np}, and the volume fraction of nanoparticles dispersed in the fluid, ϕ. The effective thermal conductivity, k/k_f, is then [21]

$$k_{eff} = \frac{k_{np}}{k_{bf}} = \frac{1 + 2\beta\phi}{1 - \beta\phi}, \tag{2.14}$$

where β is given by

$$\beta = \frac{(k_{np} - k_{bf})}{(k_{np} + 2k_{bf})}. \tag{2.15}$$

Although the Maxwell model is well-known, the expression fails for larger volume fractions of nanoparticles. Other attempts at finding a robust physical model for predicting the thermal conductivity of nanofluids have been made, but none prove to be sufficient for all situations.

Absorption

In order to exploit the energy in solar thermal systems, the incoming solar radiation must be converted into thermal energy. The energy conversion in STE consists of two steps; first, the solar energy is absorbed by the surface of the working fluid; second, the absorbed energy is transferred to the rest of the fluid through conduction and convection [52]. The working fluids' ability to absorb solar radiation is, therefore, crucial for the efficiency of the system. Absorbance differs from absorptivity as it also includes scattering and reflection within the medium. When a fluid is assumed to be homogeneous, the maximal radiation intensity, I_0, is at the surface of the fluid, $x = 0$. The Lambert-Beer law describes the exponential decay in intensity as light travels into the medium as

$$I = I_0 \exp[-Kx]. \tag{2.16}$$

Here, x is the distance that the light has traveled through the medium, and K is the extinction coefficient, which depends on the frequency of the light and the nature of the material [45]. The exponential decay, as described by Lambert-Beer, is illustrated in Fig. 2.3. By differentiating Eq. (2.16) with respect to x, the decay in the volumetric intensity becomes

$$\frac{dI}{dx} = -I_0 K \exp[-Kx]. \tag{2.17}$$

By rearranging Lambert-Beers law, the energy absorbed in a volumetric absorber is [52, 54]

$$E_{abs} = I - I_0 = I_0[1 - \exp(-Kx)]. \tag{2.18}$$

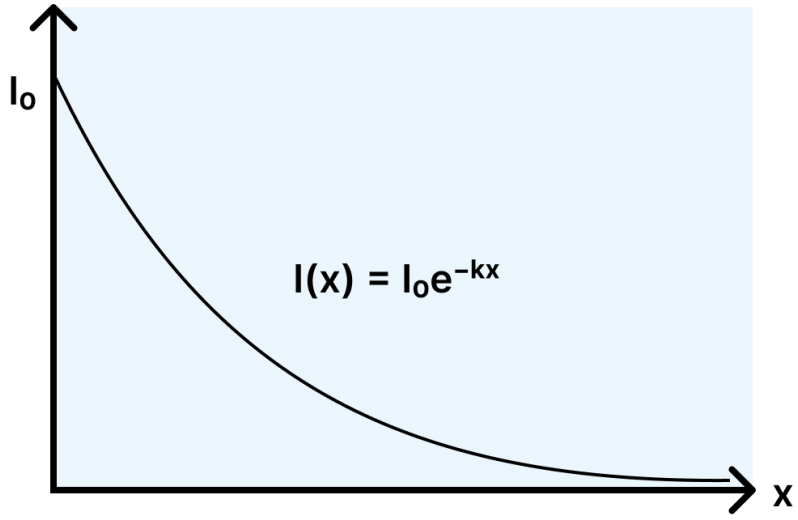

Figure 2.3: Sketch of the decay in light intensity through a fluid by Lambert-Beer law. Inspired by Nguyen et al. [53].

Heat Loss

As described in Section 2.3.1, all bodies with a temperature above absolute zero emit thermal radiation. The radiative losses from the absorbing fluid as a result of thermal radiation depend on the temperature of the surrounding. Thermal equilibrium is achieved when the rate of radiation and absorption is equal, that is $T = T_s$. For such a case, the rate of absorption can be expressed by Eq. (2.11), the Stefan-Boltzmann law. If we assume an idealized black body in thermal equilibrium, Kirchoff's radiation law says that the body emits and absorbs the same amount of energy, that is, $\alpha = \varepsilon$. Combining these two laws, the radiative losses from a volumetric absorber is [52, 54]

$$E_v = [1 - \exp(-Kx)]\sigma T_f^4. \tag{2.19}$$

E_v is the emissive power and T_f is the temperature of the fluid. Fig. 2.4 illustrates absorption and radiative losses in a traditional volumetric absorption system.

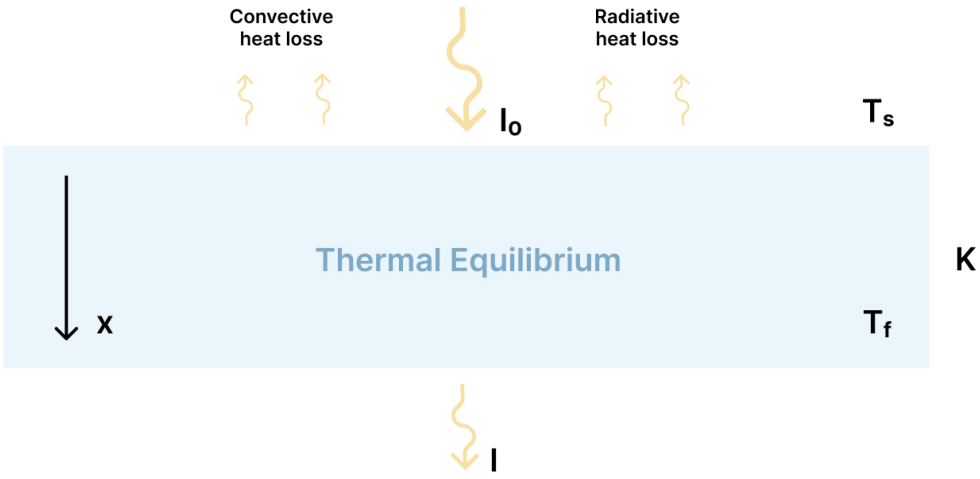

Figure 2.4: Sketch of the absorption and radiative and convective heat losses in a volumetric absorber.

2.4 Fluid Mechanics

2.4.1 Bernoulli's Equation

An important relation, showing the mechanical energy balance in a fluid flow, is the Bernoulli equation. When we assume a steady flow, with no viscosity and flow only in the z-direction between two points a (inlet) and b (outlet), the equation is expressed as [43]

$$\frac{\alpha_a \bar{V}_a^2}{2} + \frac{p_a}{\rho} + gZ_a = \frac{\alpha_b \bar{V}_b^2}{2} + \frac{p_b}{\rho} + gZ_b + h_f. \tag{2.20}$$

Here, $\bar{V}$ is the average velocity, p the pressure, and Z the elevation in the two points a and b. The equation includes two correction factors, α_a and α_b, that take account of the velocity distribution in the flow. Finally, the term h_f represents all the friction generated per unit mass of fluid between points a and b. The terms in the equation can be described as

- I: kinetic energy of a unit mass of fluid
- II: work done by an external force
- III: potential energy of a unit mass of fluid

The unit of all terms in Eq. (2.20) is energy per unit mass [J/kg].

Simplified Version

For simplicity, some assumptions have been made to execute calculations. Firstly it is assumed that the inlet and outlet are at the same elevation, which is set as zero. Further, the flow is assumed to be laminar, so $\alpha_a = \alpha_b = 2$. Lastly, the velocity is assumed to be constant throughout the system; thus, $\bar{V_a} = \bar{V_b} = \bar{V}$. With these assumptions, Eq. (2.20) is reduced to

$$\Delta p = \rho h_f. \tag{2.21}$$

Here, the total friction can be written as

$$h_f = \left(4f\frac{L}{D_i} + K_c + K_e + K_f\right)\frac{\bar{V}^2}{2}, \tag{2.22}$$

where f is the Fanning friction factor, and L and D are the total length and diameter of the pipe, respectively. The equation also includes three loss coefficients, K_c, K_e, and K_f, that represent friction loss from contraction, expansion, and fittings. When assuming no friction losses from the three loss coefficients, the final equation for estimating the pressure drop in the pipe is

$$\Delta p = \frac{32\mu L\bar{V}}{D_i^2}. \tag{2.23}$$

2.4.2 Reynolds Number

The Reynolds number, denoted Re, is a dimensionless number that describes under which conditions a laminar flow changes to turbulent [43]. The number is dependent on four quantities grouped as followed

$$\mathrm{Re} = \frac{\rho \bar{V} D_i}{\mu}, \tag{2.24}$$

where ρ is the density of the fluid, $\bar{V}$ is the average velocity, D_i is the inner diameter of the pipe, and μ is the fluid dynamic viscosity. For fluid flows where the viscous forces dominate (slow flow, low Re), the flow is laminar, while for flows where the inertial forces are strongest (faster flow, larger Re), the flow is turbulent [55]. For practical purposes, a laminar flow is assumed for a Reynolds number under 2000, and turbulence is assumed for a Reynolds number greater than 3500.

2.5 System Performance

2.5.1 Solar Collector Efficiency

The goal of any solar collector is to maximize solar absorption and minimize heat loss. The collectors' ability to reach this goal can be defined as the solar thermal efficiency of the system, which is given by the useful energy gained divided by the available energy. As shown in the literature [12, 14, 17], this relation can be expressed as

$$\eta_{eff} = \frac{Q}{A_c I_0} = \frac{\dot{m} C_p (\bar{T}_o - \bar{T}_i)}{A_c I_0}. \tag{2.25}$$

Here, Q is the useful heat gained by the solar collector, A_c is the area of the collector, I_0 is the incident solar radiation, $\dot{m}$ is the mass flow rate of the working fluid flowing through the system, and $\bar{T}_i$ and $\bar{T}_o$ are the mean inlet and outlet fluid temperatures, respectively. Another practical relation for estimating the performance of a nanofluid-based solar collector is the comparison of the heat gain by the working fluid compared to the base fluid. In order to understand the thermal enhancement obtained by the nanofluids, the following relation is used

$$\eta = \frac{Q_{nf}}{Q_{bf}}, \tag{2.26}$$

where Q_{nf} and Q_{bf} are the useful heat gained by the working fluid and base fluid, respectively.

2.5.2 Extinction Coefficient

The extinction coefficient is a measure of the ability of a medium to absorb light and is a summation of absorption and scattering coefficients [56]. Similar to thermal conductivity, the general trend in the literature is an enhanced extinction coefficient for nanofluids. During an experimental study of the performance of a tubular direct absorption solar collector with carbon-based nanofluids, Struchalin et al. [57] determined the extinction coefficient of five different concentrations of nanoparticles in two wavelength regions of the solar spectrum. The reported values indicate augmentation in the coefficient even at small weight fractions. The same conclusion was reached in the course of numerically assessing the performance of a DASC by Bardsgard et al. [58].

A relation for calculating the extinction coefficient, K, can be derived from Lambert-Beer law, Eq. (2.16) [51, 56, 58–60]

$$\frac{I}{I_0} = e^{-K\delta_f}, \tag{2.27}$$

where δ_f is the propagation length within the medium, that is the fluid thickness. When solving for K, the expression for the extinction coefficient becomes

$$K = -\frac{1}{\delta_f} \ln \frac{I_f}{I_0}. \tag{2.28}$$

2.5.3 Pumping Power

Upon evaluating the performance of systems with fluid flow, another important measure is the required pumping power. From Eq. (2.21) the pressure drop of a laminar fluid flow with constant velocity in a pipe can be calculated. The pressure drop can then be used to predict the pumping power by [20, 61]

$$PP = \frac{\dot{m}}{\rho_{nf}} \cdot \Delta p. \tag{2.29}$$

Here $\dot{m}$ is the mass flow rate, ρ_{nf} is the density of the nanofluid, and Δp is the pressure drop. Since the pressure drop is dependent on viscosity, and the pumping power is dependent on the pressure drop, both properties will increase with the increasing volume fraction of nanoparticles in the fluid.

2.6 Computational Fluid Dynamics

Computational Fluid Dynamics (CFD) is the simulation of physical phenomena in fluid flow processes, that are solved numerically [62]. The simulations can work as a substitute for experimental results in cases where experiments can be challenging or in addition to experimental research to compare with numerical results. Several comprehensive software offers CFD, where STAR-CCM+ was used in this thesis.

When working with multiphase fluid flows the ideal numerical model would be able to identify the dynamic and thermal properties of each particle in the fluid. However, such an ideal model becomes unpractical and idealistic for fluids containing millions of particles. Instead, three simplified models are developed in which bulk properties are investigated for simulating the fluid flow [63].

In the first method, the Discrete Element Method (DEM), each particle is investigated and their motion, including the working forces, is analyzed. The method is illustrated in Fig. 2.5a, where the open ball is one particle in a particle cloud. Fig. 2.5b shows the Discrete Parcel Method (DPM). Here, a parcel of particles with the same dynamic properties is identified and treated as one computational particle. These methods are a part of the Lagrangian approach which is characterized by the following of the particle or parcel. In the last method, the Two-Fluid model (TF), the particles are treated as a continuum similar to a fluid. Properties of the continuum or particle cloud are found by solving a set of algebraic conservation equations simultaneously. This approach is called the Eulerian model and is illustrated in Fig. 2.5c. In this method, the particles are not followed along a path but instead considered within a fixed control volume.

CFD is based on three fundamental principles: conservation of mass, momentum, and energy [62]. These basic principles relate to the following well-known equations

- Continuity equation
- Newton‘s Second Law
- First Law of Thermodynamics or Energy Equation

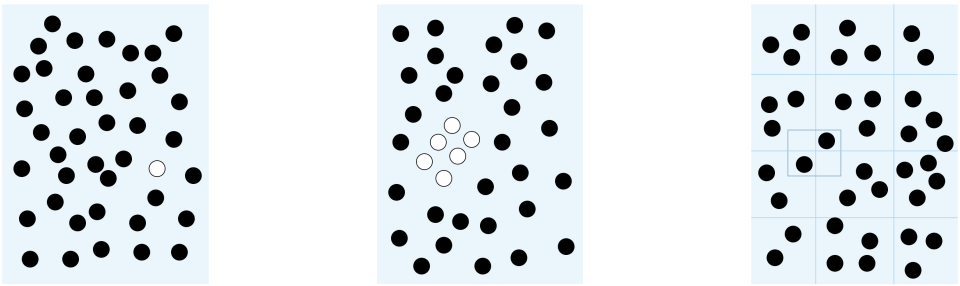

(a) Discrete Element Method

(b) Discrete Parcel Method

(c) Two-Fluid Method

Figure 2.5: Three simplified models for simulating fluid flow. Inspired by Crowe et al. [63].

2.6.1 Continuity

In any fluid, the mass balance is given by: (Rate of mass flow in) - (Rate of mass flow out) = (Rate of mass accumulation) [43]. From this simple expression, the conservation of mass through a control volume can be expressed as

$$\frac{D\rho}{Dt} + \rho(\nabla \cdot \mathbf{v}) = 0. \tag{2.30}$$

The velocity is given by $\mathbf{v}$, while ∇ is the gradient operator. For incompressible flows ($\rho = \text{const.}$), $\frac{D\rho}{Dt} = 0$, so that Eq. (2.30) is reduced to

$$\nabla \cdot \mathbf{v} = \frac{\partial u}{\partial x} + \frac{\partial v}{\partial y} + \frac{\partial w}{\partial z} = 0. \tag{2.31}$$

2.6.2 Momentum

The equation of momentum, also called the Navier-Stokes equation, is derived from Newton's Second Law: $\mathbf{F} = m\mathbf{a}$ [62]. When applied to a moving fluid element, the law says that the net force ($\boldsymbol{F}$) acting on the element equals mass (m) times the acceleration ($\boldsymbol{a}$) of the element. The net force consists of *body and surface forces*, which act at a distance from the mass (gravitational, electric, and magnetic) and directly on the mass surface (pressure and shear stress), respectively [58]. The equation is given by

$$\frac{\partial}{\partial t}(\rho \mathbf{v}) + \nabla \cdot (\rho \mathbf{v}\mathbf{v}) = \rho \mathbf{g} + \nabla \cdot \boldsymbol{\tau} - \nabla \rho. \tag{2.32}$$

Here, p is static pressure, τ shear stress, and $\rho\mathbf{g}$ the gravitational force. For an incompressible flow with constant viscosity (μ), the equation can be simplified as

$$\rho \frac{D\mathbf{v}}{Dt} = -\nabla p + \mu \nabla^2 \mathbf{v} + \rho \mathbf{g}. \tag{2.33}$$

2.6.3 Energy

The energy equation is based on the first law of thermodynamics which states that energy in a system remains constant, but may change form. Therefore, added heat or work to a system will result in increased energy in the system, or

$$dE = dQ + dW, \tag{2.34}$$

where, dE is the increment of energy in the system caused by added heat, dQ, and work done, dW. When applied to a control volume, the equation for conservation of energy can be written as [64]

$$\frac{\partial(\rho E)}{\partial t} + \nabla \cdot \big(\rho E \mathbf{v}\big) = \boldsymbol{F_b} \cdot \mathbf{v} + \nabla \cdot (\mathbf{v} \cdot \boldsymbol{\sigma}) - \nabla \cdot \mathbf{q} + S_E, \tag{2.35}$$

where E is the total energy, $\boldsymbol{F_b}$ is the resultant of body forces, $\boldsymbol{\sigma}$ is the stress tensor, q is heat flux, and S_E is an energy source per unit volume.

Chapter 3

Methods

The following section gives a description of the experimental and numerical setup used to investigate the performance of a volumetric solar absorber with carbon black nanofluids of different concentrations. Experiments were conducted for both distilled water and carbon black nanofluids of six different concentrations [wt.%]. Finally, a simplified simulation was attempted in a computational fluid dynamics software, Simcenter STAR-CCM+, to compare the heat transfer properties of distilled water with CB nanofluids.

3.1 Experimental Setup

This work aims to investigate the difference in the performance of a direct volumetric solar absorber with different absorbing fluids. An explanation of the experimental setup and method exploited is given below.

3.1.1 The Experimental Setup - DASC Design

An experimental setup was developed in order to conduct repeatable and reliable experiments. The setup is similar to a DASC, as the nanofluids directly absorb the incoming solar radiation. However, unlike a traditional DASC, which usually involves flowing nanofluids, the present design utilizes stationary nanofluids for absorption. The absorbed heat is then transferred directly through convection to a flowing working fluid which can be exploited in heat-demanding applications. This setup eliminates the need for pumping of nanofluids, which is associated with issues like erosion of piping, the lifetime of pumps, etc.

As illustrated in Fig. 3.1, the design consists of two main elements: an outer transparent glass pipe with the absorbing fluid (water or nanofluids), as well as a separate inner looped glass pipe with working fluid (water). The working fluid was pumped through the inner pipe by a Perciflow LAMBDA Peristaltic pump. The given flow rate for such a pump with an inner diameter of 3 mm and pump setting 999 is ca. 360 ml/h. Experiments and calculations were made to validate this flow rate. The internal pipe had a diameter of 6 mm and spiraled with a pitch of 10 mm. The coil had an outer diameter of 30 mm. The outer pipe, with a diameter of 38 mm and a length of 500 mm, was filled with the absorbing fluid at the beginning of each experiment.

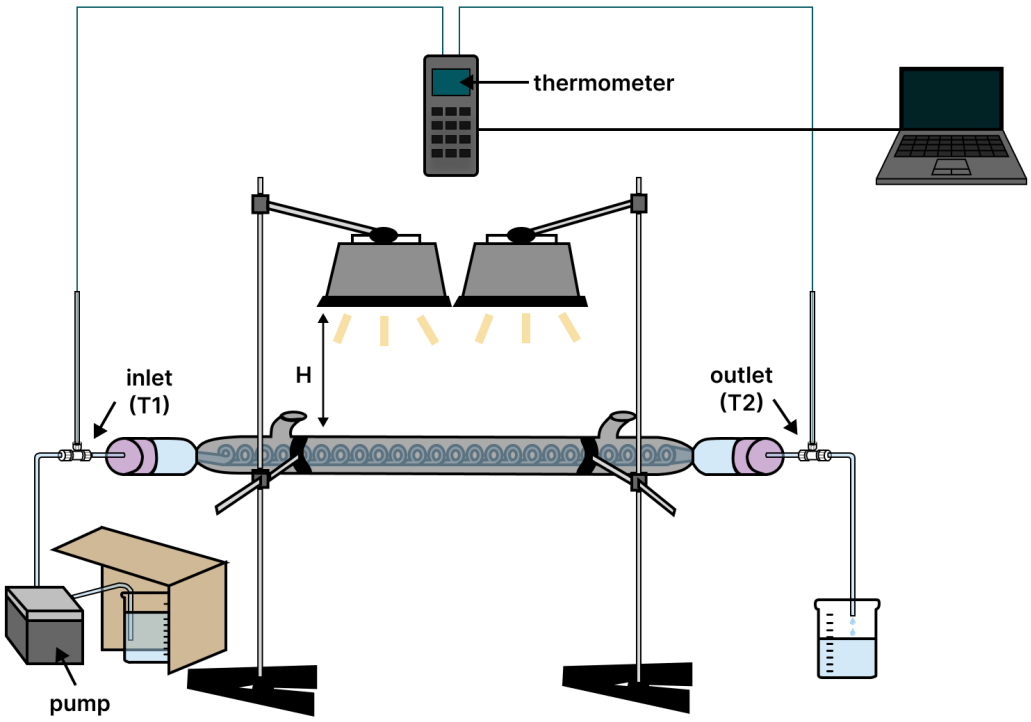

Figure 3.1: Sketch of the experimental setup.

To simulate a light source, two floodlight halogen lamps were used (400 W / 220-240 v). Experiments were conducted for two distances between the pipe system and lamps, $H = 8$ cm and $H = 12$ cm. Before each experiment, both the lamps and the pipe were leveled. The total irradiated pipe length of the system was assumed to be 46 mm. The temperature was measured with K-type thermocouples through T-junctions at the inlet and outlet of the system. Temperature logging was done using the Multilogger Thermometer from Omega Engineering and a personal

computer. As the experiments were carried out, the temperature of the system increased. The outer pipe was equipped with two openings extended by rubber pipes so that the absorbing fluid could freely expand due to the temperature rise. A cardboard cutout was placed in front of the beaker and pump to prevent heating of the experimental equipment.

Two kinds of absorbing fluid were investigated in this thesis: (i) the base fluid consisting of distilled water for reference values and (ii) carbon black nanofluids of different concentrations. Table 3.1 summarizes the equipment and instruments used in the experiments.

Table 3.1: List of the important experimental equipment.

Equipment	**Manufacturer**	**Usage**	**Uncertainty**
Precision scale	Sartorius	Used to weigh the correct amount of CB and SDS.	0.0001 g
Magnetic stirrer	VWR Collection	Used in the synthesis of nanofluids to mix CB and SDS with base fluid.	-
3510 Ultrasonic cleaner	Branson	Used in the synthesis of nanofluids to break nanoparticle clusters.	-
Perciflow Peristaltic pump	LAMBDA	Used to pump working fluid through the inner pipe of the system.	3.60 mL/h
Multilogger thermometer	Omega Engineering	Used in the experiments to measure the temperature at the inlet and outlet of the inner pipe.	0.3 °C
LS122 Infrared power meter	Linshang Technology	Used to measure the intensity of radiation from the light source for radiation mapping and estimation of extinction coefficient.	1 W/m^2

3.1.2 Preparation of Nanofluids

Nanofluids can be prepared by two different methods; one-step or two-step preparation. In the first method, the nanoparticles are made and dispersed in the base fluid simultaneously [11, 19, 20, 25, 27]. In the two-step preparation, however, the nanoparticles are first produced as a dry powder before being dispersed in the base fluid in a second step. Both methods have advantages and disadvantages. The one-step method tends to give more stable nanofluids as the process of drying, storage, transportation, and dispersion of nanoparticles are avoided. This will minimize the agglomeration of the nanoparticles. However, this way of preparing nanofluids is less economical as the nanofluids cannot be synthesized on a larger scale.

In this experiment, a two-step method of preparing the nanofluids was practiced. In all the experiments, ENSACO (TM) 350G carbon black nanoparticles from Timecal were used. These particles have a bulk density of 2 250 kg/m^3 [65] and are suitable for solar absorption purposes as they have an absorption close to that of a black body. The nanofluids were prepared by a weight percent, denoted wt.%, which is the mass, m, of a solute present in a solution. This way, the concentration can be calculated by

$$\frac{m_{solute}}{m_{solution}} \cdot 100 = \frac{m_{solute}}{m_{solute} + m_{solvent}} \cdot 100 = wt.\% \tag{3.1}$$

As mentioned in Section 2.1.1, the addition of surfactants increases the stability of the nanofluid as the agglomeration of nanoparticles decreases. An equal amount of SDS as the amount of CB was added to the fluid for stabilization. Both substances were calculated by Eq. (3.1) and weighed with the Sartorius precision scale before being dispersed in the correct amount of base fluid, in this case, distilled water. The particles were then mixed in the fluid for 20 minutes using a magnetic stirrer. Finally, the fluid was sonicated in a Branson 3510 ultrasonic bath for 60 minutes, with a frequency of 50-60 kHz. The bath is an example of an indirect sonication used to physically disperse nanoparticle clusters [26]. Fig. 3.2 summarizes the two-step method used in this thesis.

Six different concentrations of CB NFs were made: 0.0015 wt.%, 0.005 wt.%, 0.01 wt.%, 0.015 wt.%, 0.02 wt.%, and 0.05 wt.% by the use of this method.

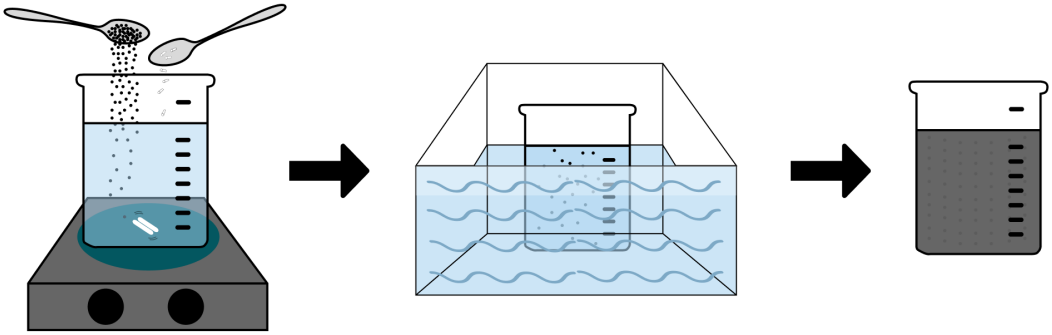

Figure 3.2: Nanofluid preparation steps. Inspired by Sezer et al. [26].

3.1.3 Radiation Source

Two floodlight halogen lamps with a maximum power of 400 W each were used as the source of radiation. The intensity of the radiation (heat flux) was measured with a Linshang LS122 IR power meter with an uncertainty of 1 W/m^2 [66]. This device is limited to a spectral range of 1000-1400 nm, that is, infrared radiation. Therefore, the measured radiation may be an understatement of the actual intensity.

In order to understand how the intensity of radiation is dependent on the distance to the radiation source, measurements were made of the intensity at four different heights. Five measurements were made at the center of the beam for each height: 0 cm, 8 cm, 10 cm, and 12 cm. The average radiation intensity at each height is displayed in Fig. 3.3 together with a fitted trend. For simplicity, radiation was assumed to be evenly distributed across the illuminated area.

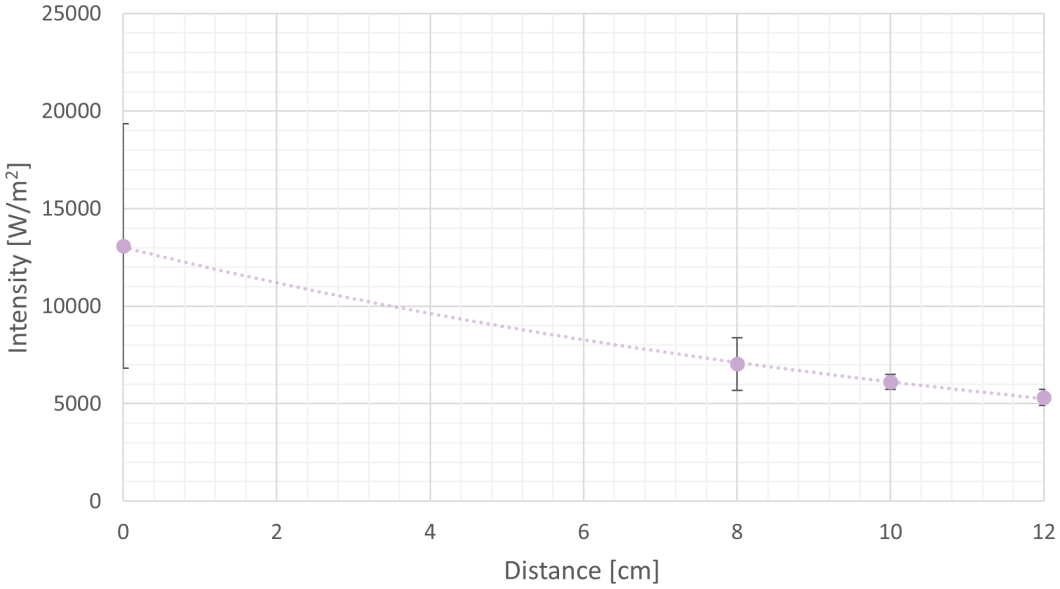

Figure 3.3: Measured radiation intensity as a function of distance with error bars.

Further, a characterization of the intensity distribution of the beam was done prior to the experiments. For this, radiation was measured with the Linshang power meter through 32 cutout holes in a cardboard plate in the dimensions of the halogen lamp, which was 14.2 x 18.0 cm. Measurements were made three times in each hole and repeated for the heights: 0 cm, 8 cm, 10 cm, and 12 cm between the lamp and the cardboard plate. The resulting average distribution at 10 cm is illustrated in Fig. 3.4. As depicted, the beam's radiation intensity is not evenly distributed, as first assumed. However, due to simplicity, an even heat flux of 6000 W/m^2 is assumed in later calculations for the radiation intensity at a distance of 10 cm from the halogen lamp. The distribution of intensity across the beam for the remaining distances are included in Appendix H.

3.1.4 Experimental Procedure

As previously mentioned, water was pumped through the inner pipe by a Perciflow LAMBDA peristaltic pump. The outer pipe was filled with the absorbing fluid, that is, water or the different concentrations of carbon black nanofluids, before initiating each experiment. The temperature was sampled in the two T-junctions of the inner pipe every other second for 60 minutes from when the lamps were turned on. After each experiment, the equipment was cooled to near-equilibrium temperatures as the surroundings before a new experiment was carried out. Experiments

Figure 3.4: Intensity distribution in [W/m^2] at a distance of 10 cm from the light source.

were repeated five times for all absorbing fluids. In addition, experiments were conducted for two different heights between the DASC and the light source, H = 8 cm and H = 12 cm. In total, 70 experiments were therefore completed.

Estimation of Extinction Coefficient

The extinction coefficient was found by adopting a similar method as the one used by Kosinska et al. [56]. As illustrated in Fig. 3.5, the same halogen lamp used in the experiments was placed in an upwards direction parallel to a cardboard plate. In the middle of the plate, a round hole the size of a 600 mL beaker was cut out, allowing radiation to escape the hole. A beaker with different fluid thicknesses, δ_f, of water and 0.0015 wt.% and 0.005 wt.% carbon black nanofluids was then placed in the cutout. The radiation intensity traveling through the fluids was measured for each case with the Linshang power meter. Three different heights, H, between the lamp and cardboard plate was measured, i.e. H = 8 cm, H = 10 cm, and H = 12 cm. For each distance, all measurements were repeated three times and then averaged to increase accuracy.

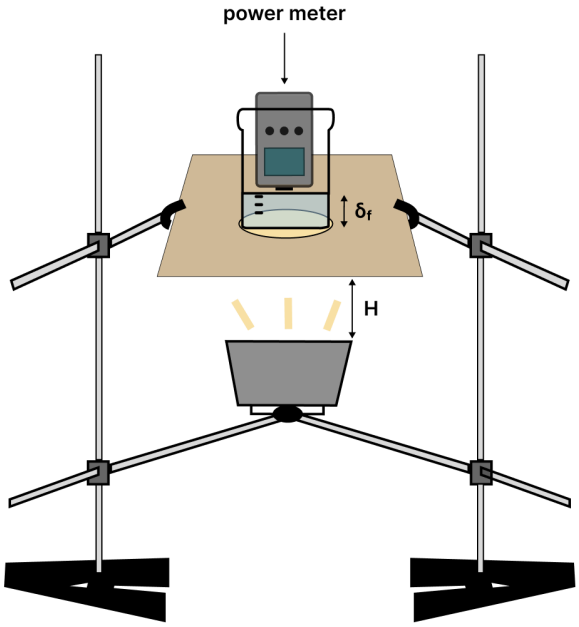

Figure 3.5: Sketch of the experimental setup for estimating the extinction coefficient.

After measuring the radiation intensity, Eq. (2.28) was used to calculate the extinction coefficient. The coefficient was only estimated for water and carbon black nanofluids of concentrations 0.0015 wt.% and 0.005 wt.%. The remaining nanofluids with a higher carbon black concentration became non-transparent when using this setup, and the extinction coefficient could, therefore, not be estimated for nanofluids of higher concentrations from this method.

Validation of Pump Flow Rate

A simple experimental setup was made to validate the stated flow rate of the Perciflow LAMBDA Peristaltic pump. A beaker was filled with 100 mL of water, including the hose of the pump. The other end of the pump was connected to another beaker. The pump was then turned on for 5 minutes. The amount of water pumped from the beaker during this time was noted. The experiment was repeated three times and revealed an average flow rate of 0.112 mL/s = 403 mL/h. This is slightly higher than the stated flow rate by the manufacturer of 360 mL/h with an uncertainty of 3.60 mL/h [67].

3.2 Simulation

Simulations were carried out by use of CFD software Simcenter STAR-CCM+. The purpose of computational fluid dynamics is to use mathematical models and numerical methods to predict flow physics. In this thesis, the simulation aims to solve the governing equations presented in Section 2.6, thereby obtaining accurate solutions for physical problems concerning nanofluids.

3.2.1 Geometry

For computational time reduction purposes, a simplification of the experimental setup was used as the simulation geometry. Fig. 3.6 illustrates the geometry, including its dimensions, used in the simulation. As portrayed, a flat plate structure was employed, which closely approximated the dimensions of the experimental setup. The geometry is divided into three sections, where the top, middle, and bottom layers represent the absorbing fluid, the glass, and the flowing base fluid, respectively.

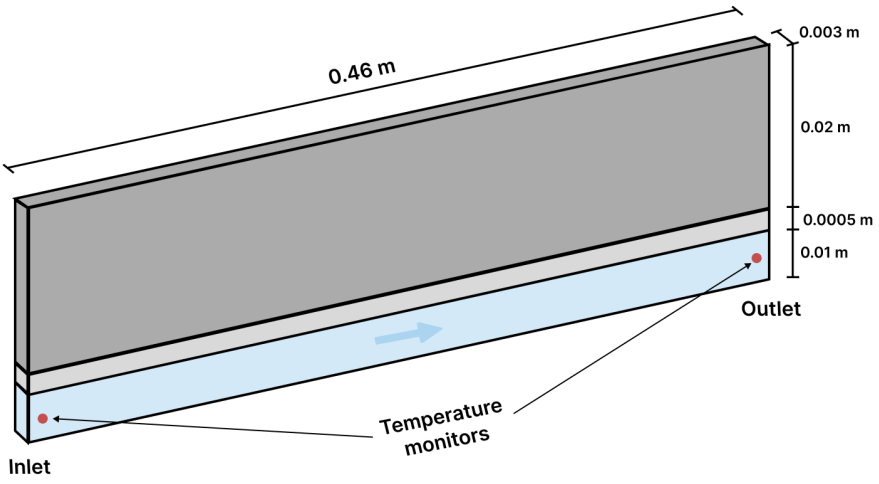

Figure 3.6: Geometry used for simulation with dimensions. Not to scale.

As the geometry is strongly simplified from the laboratory setup, the simulation results will not work as a direct comparison to the experimental results but rather deepen the understanding of the optical and physical properties of the presented fluids.

3.2.2 Mesh

Generating a good mesh is essential for the accuracy of the simulation. Essentially, each cell in the mesh represents an individual solution to the governing equations in Section 2.6. When combined, the cells form a volume mesh, and a solution for the entire system is obtained. A finer mesh will therefore ensure more accurate results but also increases the computational time. Generally, an optimal mesh should provide similar results as a finer mesh without having too long a computational time.

To find a satisfactory mesh, a mesh independence study was conducted. Depending on the system in question, different shapes and refinements of meshes should be considered. For the flat plate approach in this thesis, a mesh where the following meshers were invoked: Surface Remesher, Polyhedral Mesher, and Prism Layer Mesher, was used [64]. Different base sizes were investigated in order to compare result accuracy and computational time, which is presented later. The final mesh is shown in Fig. 3.7.

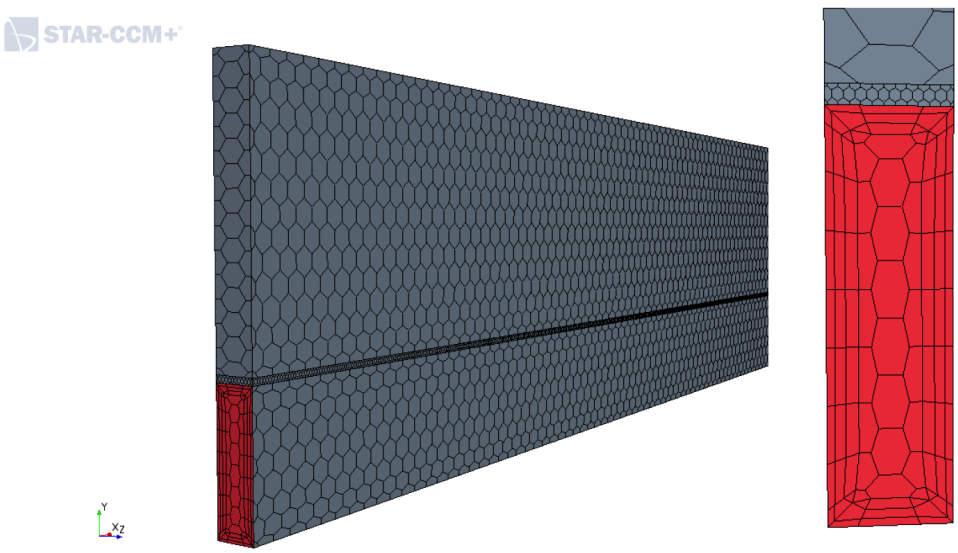

Figure 3.7: Computational mesh with a base size of 10 mm for fluid sections and 1 mm for the solid section. The number of prism layers is set as four.

3.2.3 Initial Conditions

Before executing the simulations, initial conditions defining the starting values for each solution has to be established. The fluid flow in the bottom layer was set as laminar based on the experimental velocity resulting in a low Reynolds number, validated by Eq. (2.24). The pressure and temperature of all regions were set to standard state, i.e. 1 atm and 25 °C. For the nanofluid region, the velocity was kept static, while the water region was defined to have a velocity of 0.00397 m/s in the positive x-direction based on calculations from laboratory experiments. Gravity was set as 9.81 m/s^2 in the negative y-direction.

3.2.4 Boundary Conditions

Boundary conditions are the necessary constraints needed to solve the differential equations of boundary value problems [62]. The inlet boundary conditions were set to a constant static temperature of 25 °C and velocity corresponding to the velocity calculated from experiments, that is, 0.00397 m/s. All outer walls except the top were defined as adiabatic, and all walls were set as no-slip. The no-slip condition means that the fluid velocity relative to the wall velocity is zero. The top wall of the DASC was set as the wall exposed to solar radiation, with the energy source set as a volumetric heat field function corresponding to Eq. (2.17). This boundary was also identified as the only boundary with heat loss.

3.2.5 Thermodynamic Properties

The following section describes the thermodynamic properties chosen for the three regions in the simulation geometry. All material properties for water were kept as the default operating values stated by STAR-CCM+. Some of the remaining properties were also kept as the default values, while other values were found in the literature or calculated based on experimental results. Table 3.2 summarizes the specified material properties.

Table 3.2: Material Properties at 25°C used as input in STAR-CCM+.

Property	**Water**	**0.0015 wt.%**	**0.005 wt.%**	**Glass**
Density [kg/m^3]	997.56	997.89	999.90	2702.0
Dynamic Viscosity [10^{-4} Pa s]	8.8871	10.471	17.151	-
Specific Heat [J/kg K]	4180	4174	4162	903.0
Thermal Conductivity [W/m K]	0.620271	0.620271	0.620271	0.8
Thermal Expansion [10^{-4}/K]	3.91427	3.91427	3.91427	-

The density of the two nanofluids was calculated by Eq. (2.1), where $\rho_{np} = 2250$ kg/m^3 [54]. For estimating the viscosity of the same fluids, the Einstein model mentioned in Section 2.1.2 was assumed to be applicable. Further, specific heat capacity followed Eq. (2.13), with $C_{p,np} = 710$ J/kg K [54]. Considering the lack of robust physical models, as well as the low volume fraction of nanoparticles in the applied nanofluids, the thermal conductivity was assumed to be equal to water for both situations. In reality, the thermal conductivity would probably be somewhat higher for the nanofluids, resulting in a small error. Also the thermal expansion coefficient was set as the same value as water.

Due to the lack of information on the properties of the laboratory equipment from the producer, the density and specific heat of the glass were kept as the default setting for solids by STAR-CCM+. The thermal conductivity was chosen based on literature and set as 0.8 W/m K [29].

Three heat transfer situations were identified for the simulation setup, hereby heat transfer between absorbing fluid and glass, between glass and working fluid, and heat loss from absorbing fluid to the environment. There is currently little reported data on estimating theoretical heat transfer coefficients for nanofluids. However, the available literature data suggests an increase in the coefficient with increased nanoparticle volume fraction. During their experiments on nanofluids of aluminum oxide and copper oxide, Zamzamian et al. [68] found a considerable enhancement in the convective heat transfer coefficient for nanofluids compared to the base fluid. They also reported an increase in the coefficient with increasing nanoparticle concentration, with the greatest increase reported to be 49%.

To calculate the heat transfer coefficient between the absorbing fluid and the inner glass in this thesis, Eq. (2.9) and the experimental results were used. A coefficient of 80 W/m^{2}K for low nanoparticle concentrations and 35 W/m^{2}K for distilled water was obtained. For the convective heat loss to the environment at the top boundary of the system, a heat transfer coefficient of 15 W/m^{2}K was assumed [69], while the rate of heat transfer between the inner glass and the working fluid was assumed to have a coefficient of 10 W/m^{2}K.

3.2.6 Physical Models

This section describes the enabled physical models used in the simulations. The physical model defines the mathematical formulations used to obtain solutions, and choosing an appropriate combination of the available models is therefore important to determine the physical continuum. Table 3.3 lists the physical models that were enabled for the three separate regions.

Table 3.3: Models used in the simulations for the fluid and solid sections.

Fluid	**Solid**
Three Dimensional	Three Dimensional
Liquid	Solid
Segregated Flow	-
Gradients	Gradients
Constant Density	Constant Density
Implicit Unsteady	Implicit Unsteady
Laminar	-
Boussinesq Model	-
Gravity	-
Segregated Fluid Enthalpy	Segregated Solid Energy

The implicit unsteady model is activated when the simulation is time-dependent. The solver allows for the governing equations to be solved in a coupled manner, which results in a more stable and accurate solution for problems with unsteady flow. The model is able to solve complex problems in time but also requires more computational time. Boussinesq model is enabled because of the small variations in density due to temperature differences resulting in buoyancy [64].

3.2.7 Solar Absorption

The simulations were carried out for a heat flux corresponding to a 10 cm distance from the heat source used in the experimental setup. A field function for the decay in radiation intensity, defined in Eq. (2.16) according to Lambert-Beer law, was applied as the volumetric heat source. At the chosen distance, I_0 was set as 6 000 W/m^2 based on measurements explained in Section 3.1.3. Radius was set as 0.02 m, which from Fig. 3.6 equals the absorbing fluid section of the geometry. The final function was then

$$I = I_0 k e^{k(y-r)} = 6000 k e^{k(y-0.020)}, \tag{3.2}$$

where K was calculated and changed for each applied fluid. The decay in incoming solar radiation through the fluid is illustrated in Fig. 3.8 for distilled water.

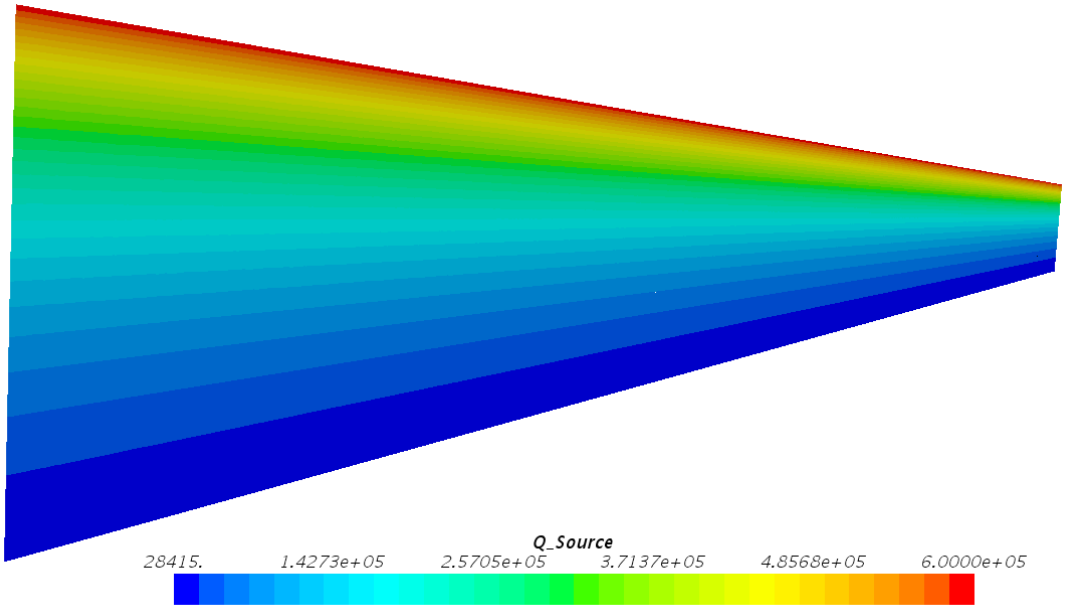

Figure 3.8: The applied heat source for water simulations in STAR-CCM+ with an extinction coefficient of $K = 100\ \mathrm{m}^{-1}$ and radiation intensity $I_0 = 6\ 000\ \mathrm{W/m}^2$.

Chapter 4

Results and Discussion

This chapter presents an investigation of the performance of distilled water and CB nanofluids of different concentrations as an absorbing fluid in a direct absorption solar collector, using both experimental and numerical techniques. First, the experimental results are presented and discussed, with emphasis on the difference in temperature increment and, thereby, the overall performance of the various fluid compositions. Subsequently, the focus will shift to the simulations that have been executed, with a comparison of thermal enhancement for three fluids. Finally, an uncertainty analysis is conducted to highlight the accuracy of the presented results in this study. Some important basic fluid properties used for calculations presented in the current chapter are listed in Appendix F.

4.1 Prerequisite

4.1.1 Specific Heat Capacity

The specific heat capacity of the nanofluid was calculated based on Eq. (2.13), and the resulting heat capacities are displayed in Fig. 4.1. As shown, it can be observed a linear decrease in the specific heat capacity with increasing mass fraction of nanoparticles. For the highest fraction of nanoparticles investigated in this thesis, the decrease reaches 4.05%. Although different models are available for deciding the specific heat capacity of nanofluids, the results are in good agreement with the general trend reported in experimental literature data [11, 47, 61], and therefore assumed applicable.

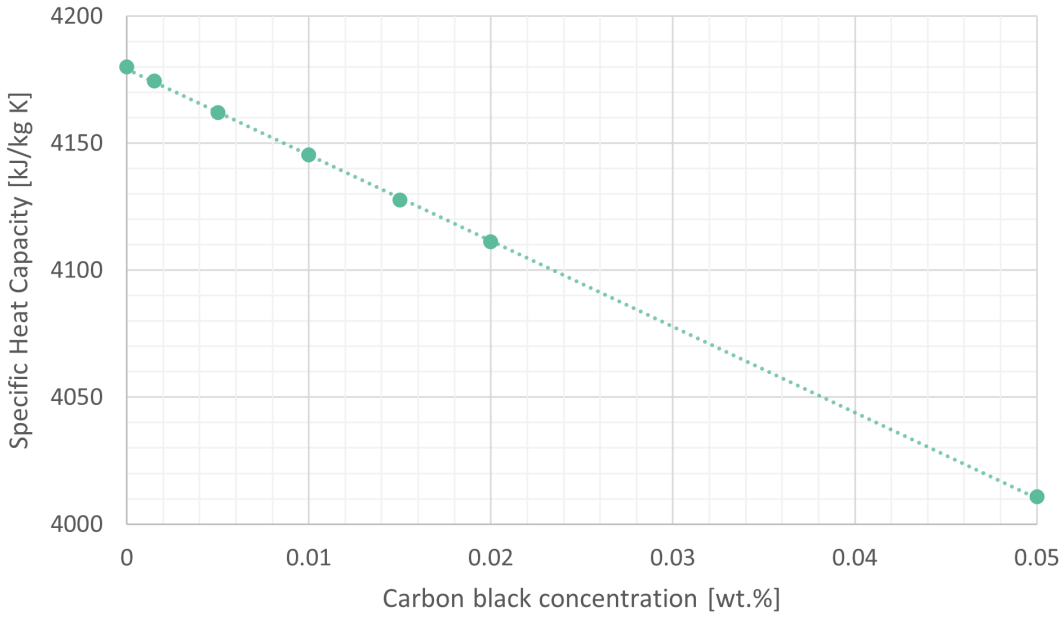

Figure 4.1: Specific heat capacity as a function of carbon black concentration.

4.1.2 Extinction Coefficient

Based on the experimental results and procedure explained in Section 3.1.4, the extinction coefficient was found for distilled water and two concentrations of CB NFs for three distances from the lamp. The extinction coefficient is essential as input during the simulation in order to express the radiation intensity decay through the fluids, by Eq. (3.2). Since the adapted method for estimating the extinction coefficient only was efficient for a very small volume fraction, and the simulation was only executed for two of these concentrations, the remaining extinction coefficients were not estimated.

Fig. 4.2 displays the estimated extinction coefficients for distilled water and two concentrations of CB NFs at a distance of 10 cm from the light source. It can be seen from the figure that the extinction coefficient increased with carbon black nanoparticle concentration. When averaging the calculated coefficients the resulting extinction coefficients are $K = 100 \pm 9.39$ m^{-1}, $K = 162 \pm 8.22$ m^{-1}, and $K = 287 \pm 23.7$ m^{-1} for distilled water, 0.0015 wt.% CB NF, and 0.005 wt.% CB NF, respectively. Additional extinction coefficient results for a distance of 8 cm and 12 cm from the light source are included in Appendix G.

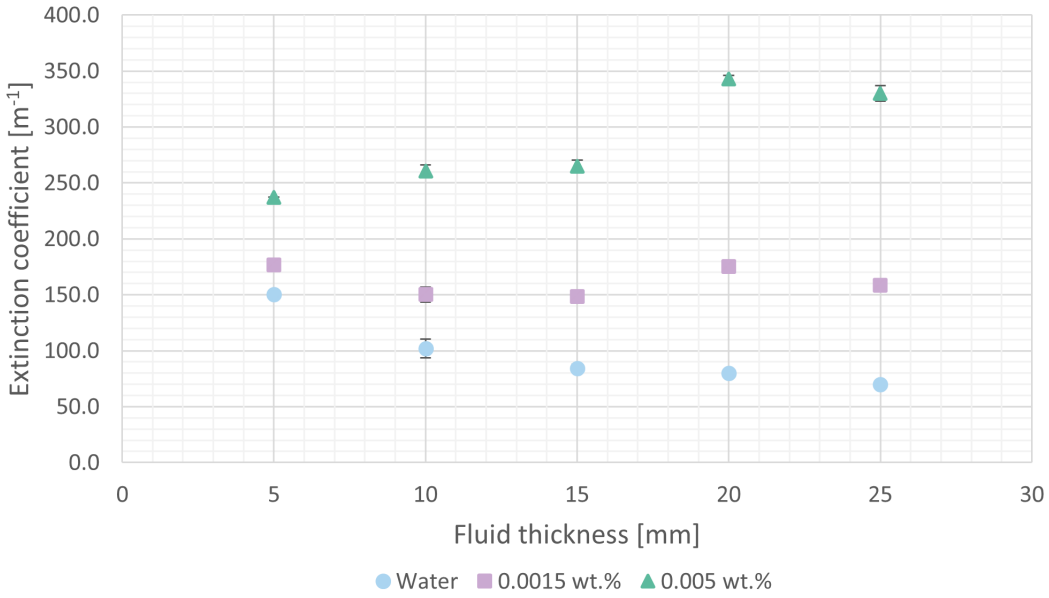

Figure 4.2: Estimated extinction coefficient for water and two concentrations of carbon black nanofluids at $H = 10$ cm with error bars.

In their study on the performance of carbon-based nanofluid in a DASC, Struchalin et al. [57] estimated the extinction coefficients of nanofluid with multi-walled carbon nanotubes (MWCNT) to be in the range $K = 220$-1255 m^{-1} considering different nanoparticle concentrations. The measurements were made with consideration of wavelengths in the spectral range and separated into two parts of the spectrum: 400-1100 nm and 1100-1700 nm. For the first range, the authors reported an extinction coefficient of $K = 25$ m^{-1} and $K = 220$ m^{-1} for weight concentrations of 0.000 and 0.008, respectively. In the second range, the coefficients were significantly higher and corresponded to $K = 161$ m^{-1} and $K = 378$ m^{-1} for the same concentrations. In both ranges, the coefficient increased with increasing particle concentration, with the highest considered weight fraction of 0.100 wt.% resulting in the highest extinction coefficient.

A similar increase in extinction coefficient with increased nanoparticle concentration was found by Khosrojerdi et al. [51] in their research on graphene oxide nanoplatelets nanofluids in a DASC. At a weight fraction of 0.005 wt.%, the extinction coefficient increased to 400 m^{-1} at the most optimal wavelength. Also Bardsgard et al. [58] reported an increase in extinction coefficient during their numerical analysis of a DASC with nanofluids. They found the extinction coefficient for particle concentrations in the range 0-0.1 vol.% to be between 0.8 and

10000 m^{-1}. Another comparable study, conducted by Nguyen et al. [53], found an increasing coefficient as a function of nanoparticle mass fraction, with $K = 730.5$ m^{-1} at a concentration of 0.01 wt.% carbon black.

When compared with the data found in the literature, the experimentally calculated extinction coefficients have similar tendencies. As with the mentioned research above, the extinction coefficients are enhanced with increased nanoparticle concentration. However, since the chemical composition of the exploited nanoparticles and the experimental approach differs from those studied in the present work, the coefficients cannot be directly compared. The applied method for estimating the extinction coefficient in this study also fails for nanofluids with a concentration above 0.005 wt.%. As a consequence, an investigation of further development of the extinction coefficient with increased weight fraction was not conducted and can, therefore, not be compared with the literature data for the specific carbon black nanofluids used.

It is interesting to notice that the coefficients do not seem to change significantly with distance to the light source. As presented in Fig. 4.3a, 4.3b, and 4.3c, the measured values are consistent at each height. The largest deviation is found for the nanofluid with a weight concentration of 0.005 wt.%, where the trend for $H =$ 10 cm differs from the other two heights.

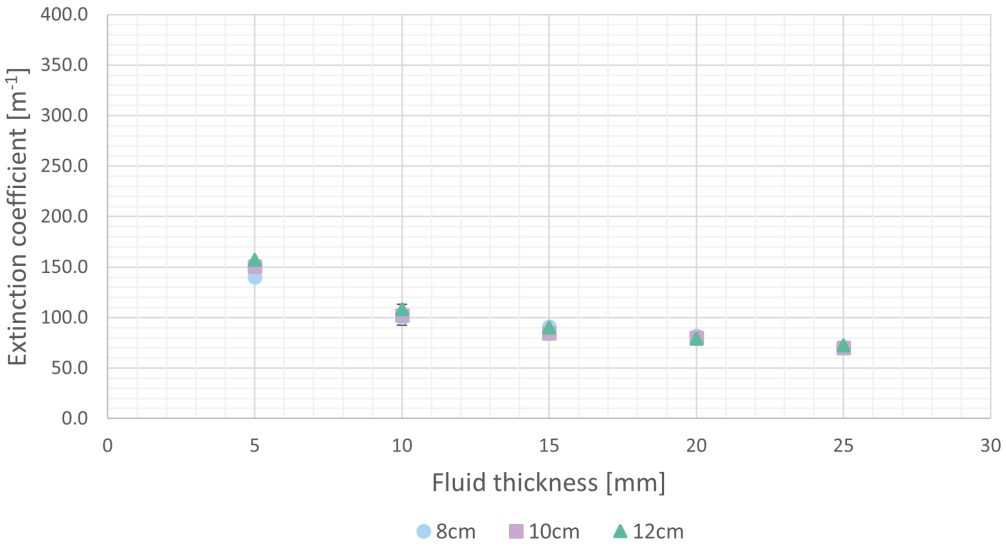

(a) Estimated extinction coefficient for water at three different distances to the light source.

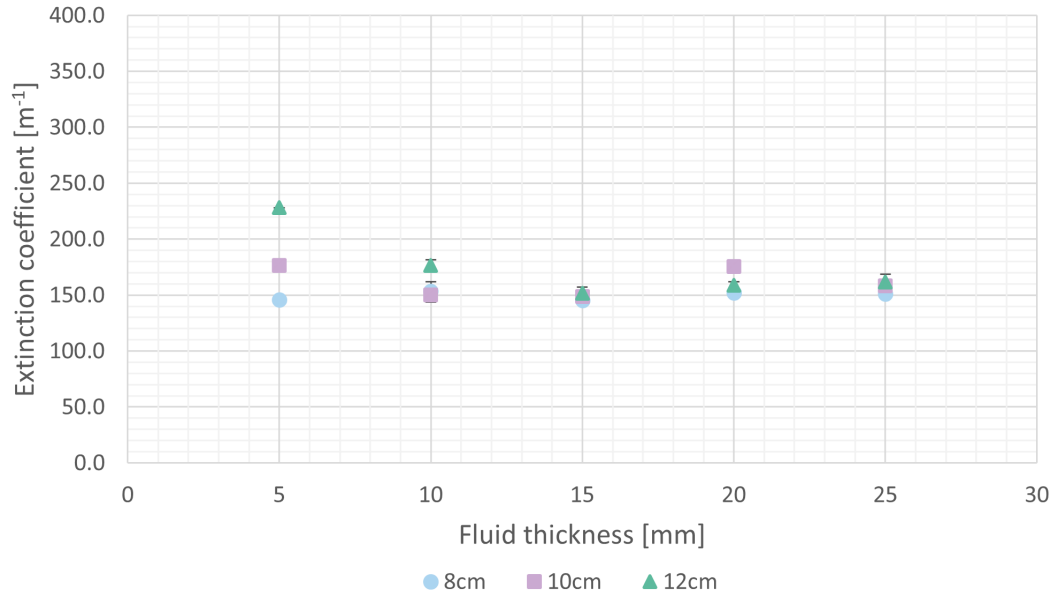

(b) Estimated extinction coefficient for 0.0015 wt.% nanofluids at three different distances to the light source.

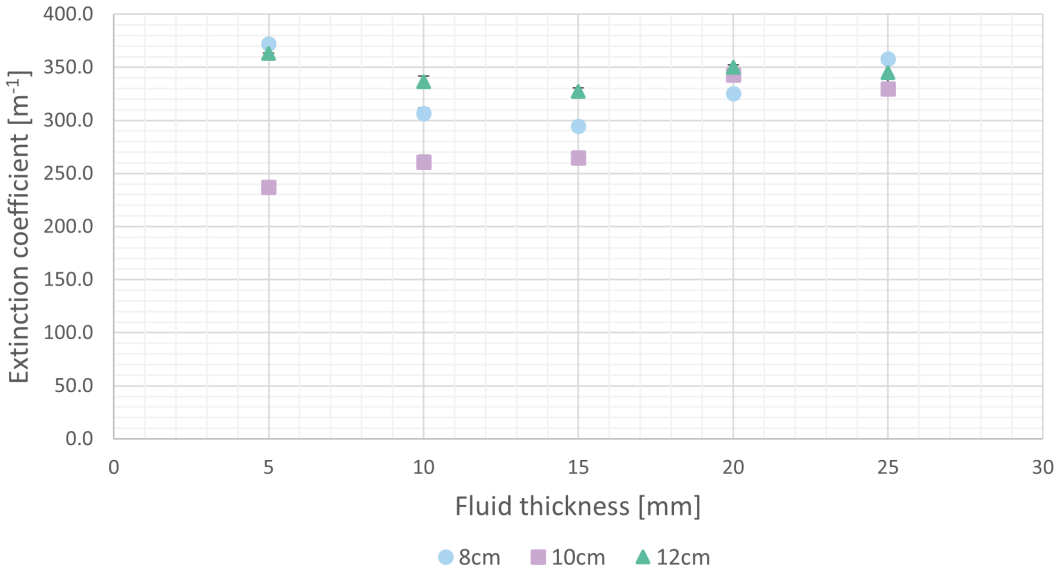

(c) Estimated extinction coefficient for 0.005 wt.% nanofluids at three different distances to the light source.

Figure 4.3: Extinction coefficient for water and nanofluids of concentrations 0.0015 wt.% and 0.005 wt.% at 8 cm, 10 cm, and 12 cm from the light source.

4.1.3 Pressure Drop in Inner Pipe

Introducing nanofluids in solar applications may lead to thermal enhancement but is also associated with increased pressure drop in the fluid flow [11, 17]. As shown in Section 2.4, the pressure drop of a laminar fluid flow with constant velocity in a pipe can be calculated by Eq. (2.21). From the equation, an increase in the viscosity of the fluid in question will increase the pressure drop through the pipe. As nanofluids have a greater viscosity than base fluid, the pressure drop is more substantial in situations where nanofluids are used as the working fluid. Fig. 4.4 presents the calculated pressure drop for the relevant nanofluid concentrations in the present work. The values are calculated based on Eq. (2.21), where the viscosity was found using the Einstein model explained in Section 2.1.2.

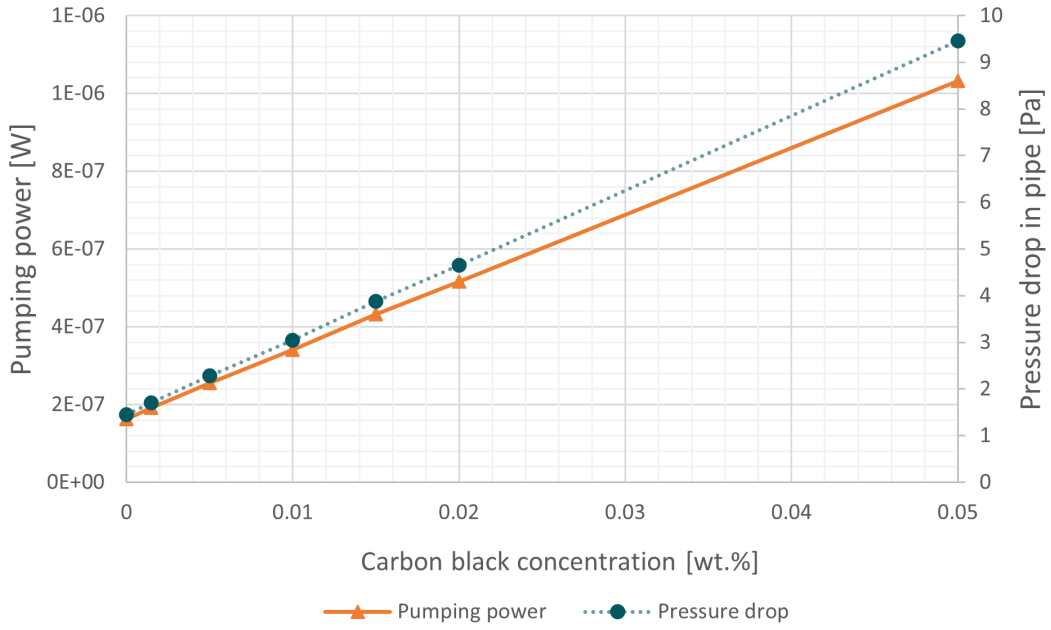

Figure 4.4: Estimated pressure drop and pumping power through the inner pipe as a function of carbon black concentration.

From Eq. (2.29), increased pressure drop requires higher pumping power to the system. The related pumping power given increased pressure drop is also included in Fig. 4.4 and clearly increases with nanoparticle concentration. As the experimental design in this thesis utilizes stationary absorbing nanofluids and water as a flowing working fluid, the design does not require increased pumping power with an increased concentration of nanofluids. This makes the present design an interesting and desirable alternative to more traditional DASC systems.

4.2 Photothermal Experimental Results

The following section presents the experimental results. All experiments had a duration of 60 minutes, and the temperature was sampled at the inlet and outlet every other second. The average initial room temperature was 21.9 ± 0.316 °C at the start of the experiments and 23.3 ± 0.290 °C at the end. The solar collectors gained heat, efficiency, and enhancement were calculated based on the theory explained in Section 2.5.1 with the data presented in Table F.4.

4.2.1 Temperature

Inlet Temperature

Fig. 4.5 presents the average temperature change at the inlet based on the initial inlet temperature of each concentration at H=12 cm and H=8 cm. As shown, the different fluid samples had a range in initial temperature of 20.8-22.4 °C. Although the inlet temperature increased for all conducted experiments, the increment was small compared to the final outlet temperature discussed in the next section. Still, it is important to notice that this has an effect on the overall results. Although some efforts were made to prevent heating of the fluid at the inlet, such as the cardboard cutout positioned in front of the experimental setup, the observed increase was due to heating from the light source.

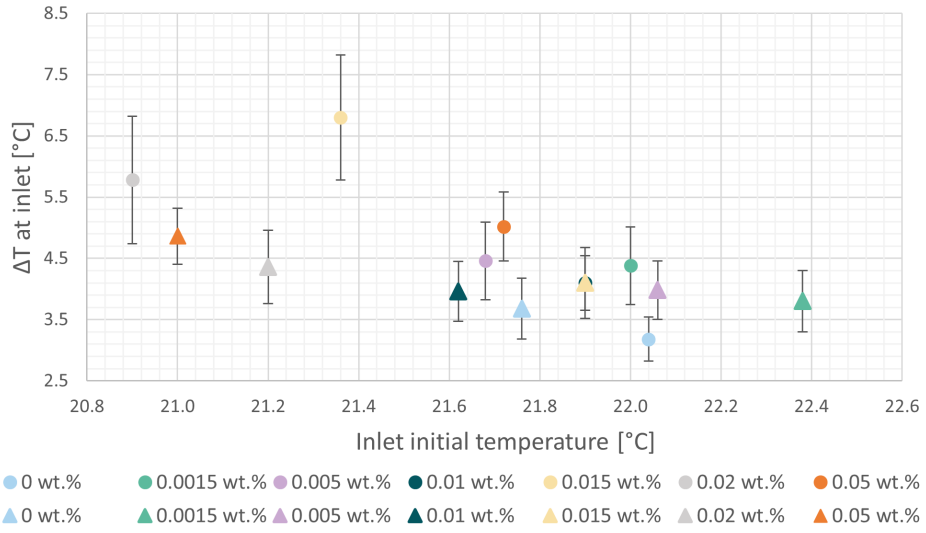

Figure 4.5: Average temperature change at the inlet as a function of starting temperature. Dots represent values for H = 12 cm, while triangles represent H = 8 cm.

Outlet Temperature

Fig. 4.6 displays the average temperature at the outlet for water and the different concentrations of CB after 30 and 60 minutes and at two distances from the light source. An increase in the fluid temperature for all concentrations of CB compared to that of water is easily observed. The ratio of temperature change during the first 30 minutes versus the last 30 minutes of the experiments is illustrated in Fig. 4.7. Interestingly the temperature increase was most dominant for all fluids during the first 30 minutes. On average, the temperature increment was 72.5±10.5% and 77.9±10.1% of the total increase during the first 30 minutes at $H = 12$ cm and $H = 8$ cm from the light source, respectively. The greatest outlier was for a concentration of 0.0015 wt.% at 8 cm, which only increased by 67.9±3.29% during the first 30 minutes.

The prominent increase in temperature during the first 30 minutes, as seen in Fig. 4.7, is an effect of stagnation in temperature development as the system reaches thermal equilibrium with the environment. As the temperature at the surface increase, the rate of heat transfer to the environment through radiation and convection also increase. Eventually, the rate of heat transfer to the environment will surpass that of heat transfer to the fluid, and the system achieves a steady-state value. An illustration of such a situation was presented in Fig. 2.4.

In all experiments, oscillation tendencies in the fluid temperature were registered. The oscillation is a consequence of local boiling in the fluid due to high temperatures, which was visible during the experiments as small bubbles formed in the pipes. The oscillation tendencies were smoothed out by applying a moving average trendline to the experimental results. The trendline was calculated by averaging 100 samples and then plotting the average over time, thereby reducing the noise in the data. This way, a more clear and smooth picture of the underlying temperature development trend could be observed and analyzed.

As mentioned, five experiments were executed for each fluid sample. The average outlet temperature result of each experiment are listed in tables in Appendix B and displayed in the figures in Appendix D for $H = 12$ cm and $H = 8$ cm.

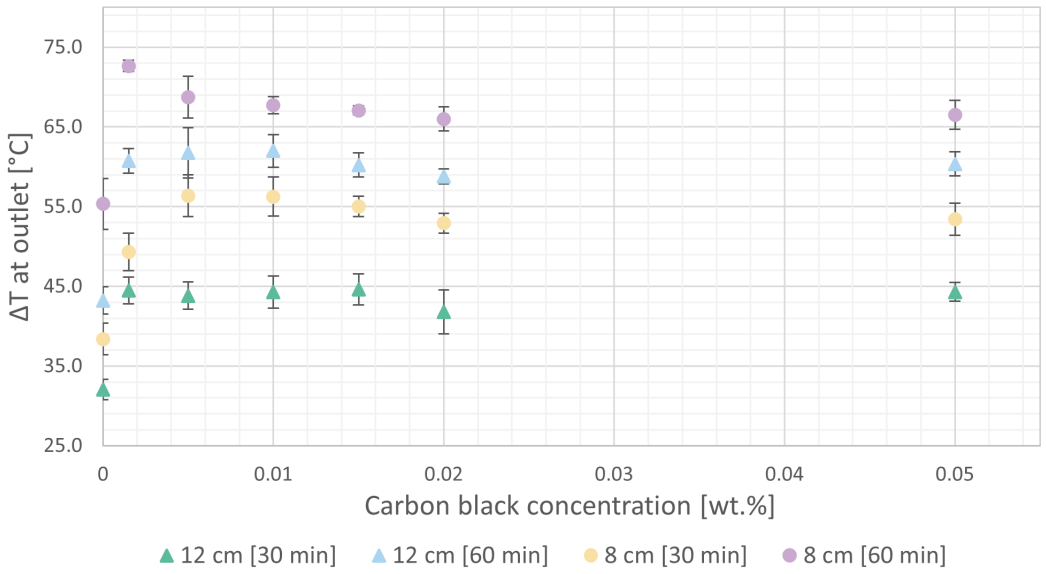

Figure 4.6: Average ΔT at the outlet at both distances, $H = 12$ cm and $H = 8$ cm, for water and for all six NF concentrations after 30 and 60 minutes.

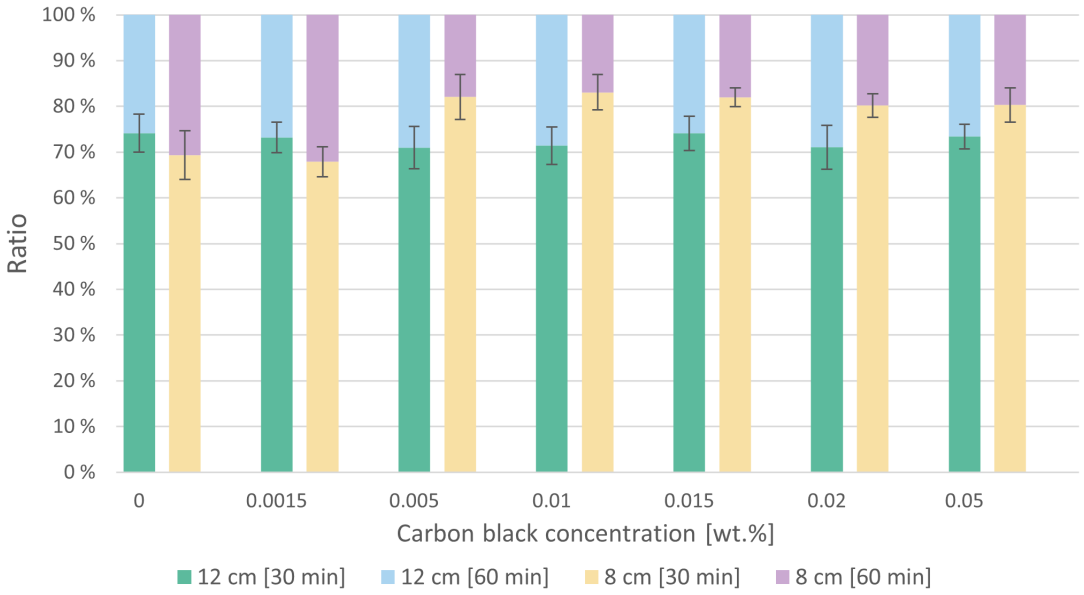

Figure 4.7: Ratio of temperature increase during the first and last 30 minutes as a function of carbon black concentration.

Outlet Temperature of Distilled Water

Measurements were made for distilled water to create reference values for the performance of nanofluids in the DASC. Fig. 4.8 displays the moving average of the recorded values in the five water experiments at $H = 8$ cm. After 60 minutes, the final ΔT at the outlet was 43.2 ± 1.70 °C and 55.4 ± 3.19 °C for water at a distance of 12 cm and 8 cm, respectively. The resulting temperatures equal a thermal efficiency of 19.6 ± 1.69% and 18.7 ± 3.80%, found by Eq. (2.25), for the two distances.

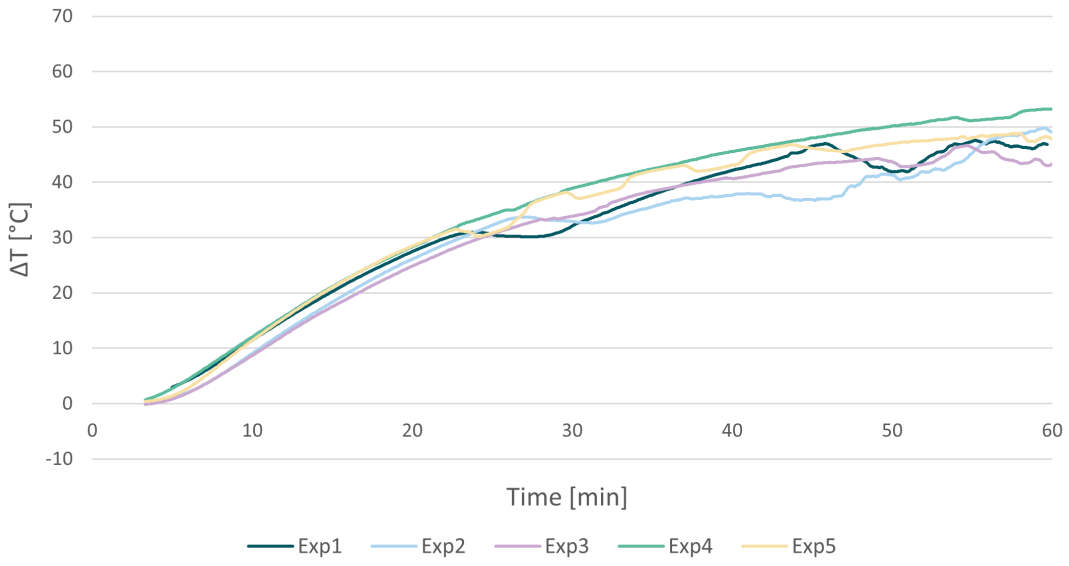

Figure 4.8: Average ΔT at $H = 8$ cm of each distilled water experiment.

Outlet Temperature of Carbon Black Nanofluids

As presented in Fig. 4.6, all experiments with nanofluids outperformed those of distilled water. The highest recorded ΔT was for the nanofluid with the lowest CB concentration, i.e. 0.0015 wt.%, at a distance of 8 cm after 60 minutes. Fig. 4.9 shows the moving average temperature development with time in the five experiments with this concentration at $H = 8$ cm. As seen, the temperature rapidly increased in the first 30 minutes before slowing down. After 45 minutes, the increase escalated again before finally flattening out at around 52 minutes. The resulting temperature increase at the outlet after 60 minutes was 72.6 ± 0.705 °C. The thermal efficiency for this system was 24.9 ± 4.78%, which is an increase of 6.17 ± 2.34% from the system with distilled water.

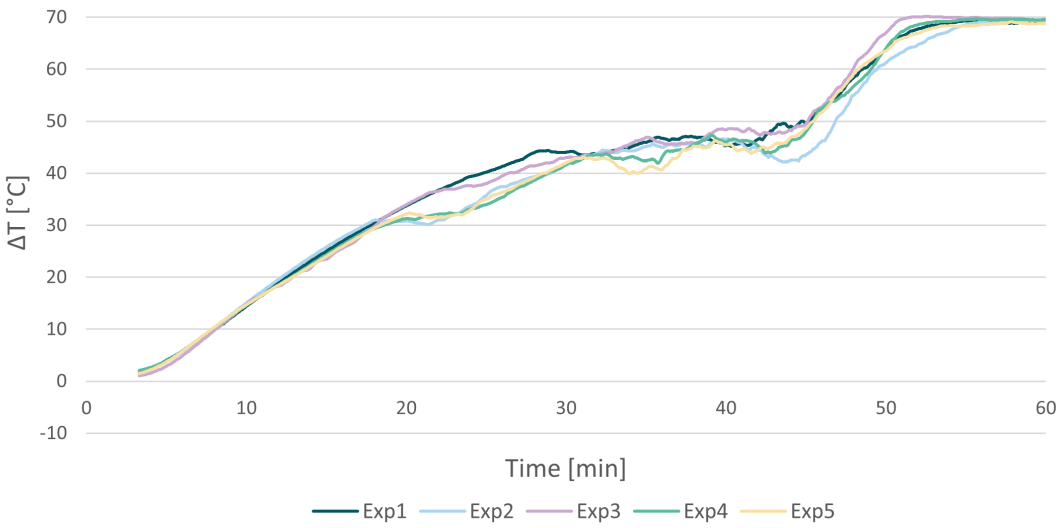

Figure 4.9: Average ΔT at $H = 8$ cm for a concentration of 0.0015 wt.% for each experiment.

A potential explanation for the escalated temperature increase after 45 minutes is the phenomenon of nanobubble boiling [65, 70]. This concept suggests that as boiling temperatures in the fluid are reached, a vapor bubble will be formed and encapsulate each nanoparticle. As vapor is a poor thermal conductor, heat transfer to the surrounding liquid will slow down and create a temperature difference in the fluid. Thermal equilibrium will thus be reached in the entire fluid after a longer period of time than if the entire fluid was continuously heated by the heat flux. In the experimental setup in the present work, the concept of nanobubble boiling will momentarily decrease the heat transfer within the nanofluid section as high temperatures are reached at the surface. As the temperature development of the working fluid is dependent on the heat transfer in the nanofluids, this will slow down the development of the outlet temperature. However, as temperatures continue to increase, heat transfer will continue as thermal equilibrium is reached within the nanofluid layer, thereby increasing the temperature in the working fluid after a period of stagnated temperature. As the boiling of nanofluids was not a part of the scope of this work, this phenomenon will not be investigated further.

High final temperature values were also recorded for the CB nanofluids of concentration 0.005 wt.%. The final average ΔT at the outlet for this concentration was found to be 68.7 $\pm$ 2.60 °C after 60 minutes at $H = 8$ cm. From Fig. 4.10 the temperature for this concentration had a rapid increase during the first 30

minutes before slowly flattening out for the remaining time. After 45 minutes, the five experiments had a somewhat different development caused by a random experimental error, resulting in high uncertainty in the final results. Nonetheless, the thermal efficiency was calculated as 23.5 ± 4.59% and therefore had a thermal enhancement of 25.4 ± 3.79% compared to distilled water.

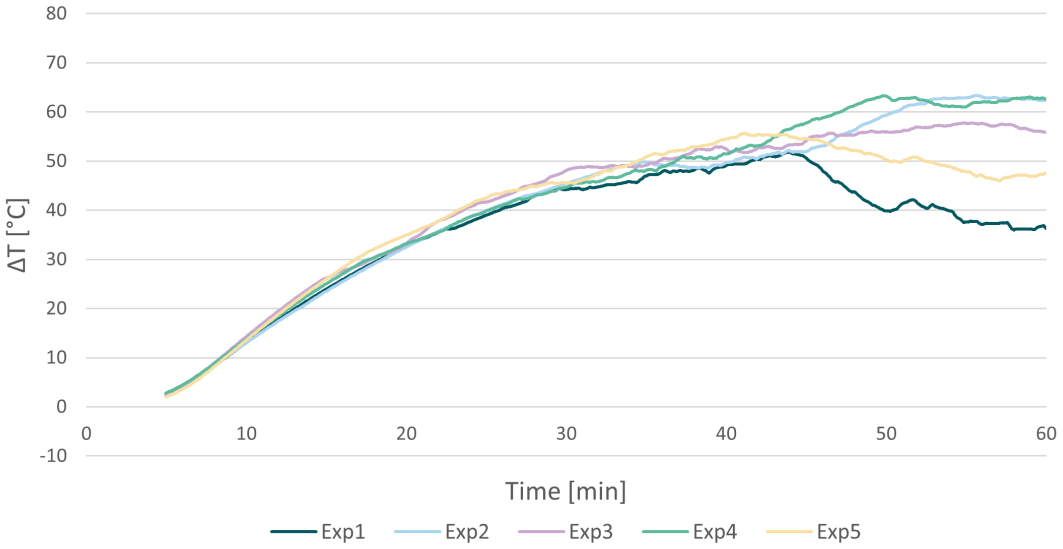

Figure 4.10: Average ΔT at $H = 8$ cm for a concentration of 0.005 wt.% for each experiment.

An investigation of the photothermal properties of graphene nanoplatelets nanofluids in a DASC by Vakili et al. [71] demonstrated improved thermal conductivity and extinction coefficients for nanofluids in the range 0.00025-0.005 wt.%. The nanofluid of concentration 0.005 wt.% exhibited the most effective performance, as it was capable of absorbing almost all of the incoming solar energy. These results are in somewhat agreement with the experimental findings in this thesis, where the fluid with the same concentration proved to have good performance. However, the finding that the fluid with a concentration of 0.005 wt.% did not exhibit the best performance in the present work suggests that system design and the specific type of nanoparticles employed play a role in the observed behavior.

The two distances between the experimental setup and the light source were investigated to further understand the effect distance has on absorbed radiance. It is clear from the results in Fig. 4.6 that the temperature increase was most prominent at the shorter distance, i.e. for $H = 8$ cm. The average increased temperature at

the outlet after 60 minutes was found to be 7.72 °C higher for $H = 8$ cm compared to $H = 12$ cm. The deviation between the two distances in the final temperature was relatively similar for water and all concentrations, except for a small deviation for 0.0015 wt.%.

From Fig. 4.6, all concentrations had a higher final temperature at the shortest distance from the light source. However, the concentration that performed best compared to the reference distilled water experiments was 0.01 wt.% at $H = 12$ cm after 60 minutes. This concentration had, on average, an increase in temperature of 18.8 ± 2.66 °C more than that of water at the same distance after the experiments. This increase resulted in an efficiency of $27.9 \pm 2.33\%$, which was $8.30 \pm 2.88\%$ higher than for water at the same height. The total thermal enhancement was, therefore, $42.3 \pm 4.49\%$. Fig. 4.11 displays the difference in temperature increase between water and each concentration of carbon black at the two distances and suggests a higher thermal enhancement for experiments at $H = 12$ cm.

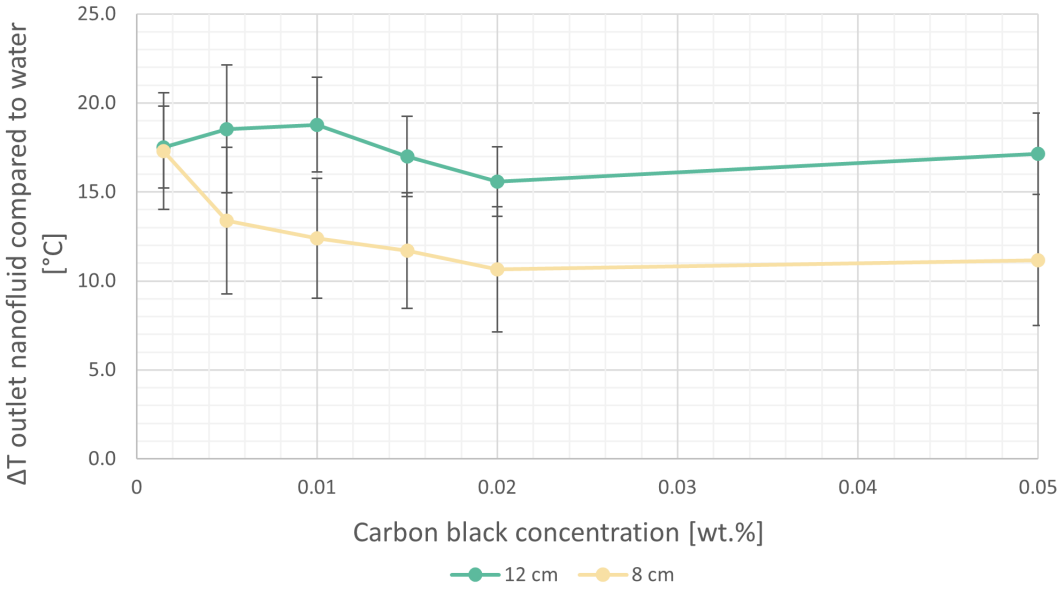

Figure 4.11: Temperature difference, ΔT, between final outlet temperature of nanofluids and water.

Analysis of Thermal Efficiency

Table 4.1 and 4.2 summarizes the solar collector efficiency, gained heat, and enhancement when utilizing distilled water or different carbon black concentrations in base fluid as absorbing fluids. The thermal enhancement was calculated by Eq. (2.26), and was, as shown in the last column, found for all concentrations of nanofluids at both distances from the lamp. Additional temperature development graphs for concentrations 0.01-0.05 wt.% are included in Appendix C.

Table 4.1: The collector efficiency, gained heat and thermal enhancement for all investigated fluids at $H = 12$ cm.

Concentration [wt.%]	**Thermal efficiency [%]**	**Gained heat [J/s]**	**Thermal enhancement [%]**
0	19.6	20.2	-
0.0015	27.6	28.4	40.4
0.005	27.9	28.7	42.0
0.01	27.9	28.8	42.3
0.015	27.0	27.8	37.6
0.02	26.3	27.0	33.8
0.05	26.3	27.1	34.0

Table 4.2: The collector efficiency, gained heat and thermal enhancement for all investigated fluids at $H = 8$ cm.

Concentration [wt.%]	**Thermal efficiency [%]**	**Gained heat [J/s]**	**Thermal enhancement [%]**
0	18.7	25.5	-
0.0015	24.9	33.9	32.9
0.005	23.5	32.0	25.4
0.01	23.1	31.4	23.1
0.015	22.7	31.0	21.3
0.02	22.3	30.4	18.9
0.05	21.9	29.9	16.9

There are several factors that contribute to the improved performance observed in the results [11]. First of all, important heat transfer properties such as thermal conductivity and convective heat transfer coefficient are increased when adding nanoparticles to the base fluid. Secondly, the optical properties of nanofluids are enhanced compared to those of water. As shown, this applies to, among others, the extinction coefficient, which is a measure of a fluid's ability to absorb light. These augmented absorption abilities are mainly due to the increased surface area of the

small nanoparticles. The large surface area to volume ratio of nanoparticles also increases the effective surface area for heat transfer, allowing for higher thermal efficiency.

In their evaluation of the performance of a DASC with nanofluids of three different materials, Otanicar et al. [36] found a 5% enhancement in efficiency when utilizing nanofluids. The increment in efficiency was consistent with increased volume fraction up to 0.5 vol.%, after which the efficiency decreased slightly. Also Han et al. [35] reported thermal enhancement when experimentally assessing the thermal properties of carbon black nanofluids in solar absorption. Increased temperatures were found compared to that of pure water for volume fractions up to 7.7 vol.%.

The increase in thermal efficiency compared to that of water in the present work ranged between 2.7-8.3% for nanofluids of carbon black nanomaterial with concentrations in the range 0.0015-0.05 wt.%, and the enhanced thermal efficiency is thereby consistent with other work. The degree of enhancement, however, proves to be significantly dependent on the particle concentration. During their experimental and numerical study on the performance characteristics of a DASC with MWCNT nanofluids, Delfani et al. [69] noted the extent of thermal enhancement with increasing concentration. The authors found that the enhancement was largest for the lowest concentration investigated (25 ppm), after which the efficiency improved marginally until 100 ppm. Further increments beyond this volume fraction lead to a reversed trend. Although the solar absorption, and thereby the overall performance, is increased for high-volume fractions, the resulting high-temperature region at the top has attendant heat losses to the environment, giving the observed trend. The same conclusion was also drawn by Gupta et al. [72], where the highest efficiency of 39.6% for aluminum nanofluids in a DASC was recorded at a concentration of 0.005 vol.%. At concentrations exceeding this, a decrease in the efficiency was noted.

A similar tendency is seen in the results in Table 4.1 and 4.2, where high thermal enhancement is registered at very low concentrations. At a certain weight fraction, the nanoparticles work as radiation blocking near the surface due to high extinction coefficients, ultimately limiting the heat transfer in the fluid and causing higher thermal losses to the environment. This is likely the cause of the decrease in efficiency seen for higher volume fractions in the present work. In order to achieve an optimal solar collector, it is crucial to thoroughly evaluate the impact of increased thermal efficiency from higher concentrations versus the subsequent heat loss.

4.2.2 Summary

The solar collector in the present work outperformed water for all concentrations of nanofluids with carbon black. Improvement in outlet fluid temperature ranged between 10-19 °C after 60 minutes of exposure to the light source. This equals an improved solar collector efficiency of 2.7-8.3% compared to the reference values with distilled water as the absorbing fluid.

The highest temperature increase, and thereby the most heat gained, was recorded for 0.0015% at $H = 8$ cm. This concentration reached a final change in outlet temperature of 72.6 ± 0.637 °C after 60 minutes, which equals 33.9 ± 0.705 J/s heat gained. However, the absorbing fluid with the highest efficiency and best thermal enhancement compared to water was that of carbon black concentration 0.01 wt.% at $H = 12$ cm. This absorbing fluid had an average collector efficiency of $27.9 \pm 2.33\%$, which equaled an enhancement of $42.3 \pm 8.30\%$ compared to the reference distilled water collector. Both heights reached the highest efficiencies at very low particle concentrations. At larger concentrations, the improvement in efficiency decreased due to radiation blocking and high thermal losses.

Upon evaluating the pressure drop calculated in Section 4.1.3, it becomes evident that the employed experimental set-up in this study yields a favorable outcome. The physical separation between the absorbing and working fluid allows for fluid flow of water associated with minimal pressure drop while still harnessing the absorption benefits of the nanofluids. As a result, the system attains high efficiency. However, it should be noted that temperature development in the nanofluids seems to stagnate after a certain time due to thermal equilibrium. A system with moving nanofluids reduces the likelihood of reaching equilibrium with the environment so that heat transfer to the fluid can continue. Careful consideration where both of these aspects are contemplated is essential when designing and optimizing solar absorption systems.

4.3 Numerical Experiments

The following section presents the simulation results from the numerical analysis in Simcenter STAR-CCM+. Three fluids of different particle concentrations were investigated with an applied volumetric heat source that corresponds to a distance of 10 cm from the heat source used in the laboratory experiments, that is, $I_0 = 6000$ W/m^2. Each simulation was carried out for 60 minutes in physical time in CFD. The temperature was sampled at the inlet and outlet of the geometry, as shown in Fig. 3.6.

4.3.1 Mesh Independence Study

As mentioned, a mesh independence study was conducted in order to find the most optimal mesh for executing the simulations. The objective was to find a mesh that would provide accurate and reliable results while using the minimum amount of computational time. In Table 4.3, the three investigated meshes are listed. Each mesh was simulated for 60 minutes in CFD physical time and then compared. The resulting temperature with the total number of cells is displayed in Fig. 4.12. Based on the final outlet temperature and the computational time, the middle mesh was chosen as the optimal mesh for further simulations.

Table 4.3: Definition with base size and number of cells of the different meshes.

Mesh	Section	Base size	Number of cells
Finest	Fluid	0.001	73287
	Glass	0.0005	289541
	NF	0.001	123549
Middle	Fluid	0.01	28401
	Glass	0.001	289675
	NF	0.01	43491
Poorest	Fluid	0.02	11573
	Glass	0.005	13086
	NF	0.02	17161

4.3.2 Temperature

Fig. 4.13 shows the temperature results as a function of nanofluid concentration from the three executed simulations after 60 minutes in CFD physical time. The figure also includes the applied extinction coefficient for each simulation. These were found by the employed method explained in Section 3.1.4 and were, as displayed, increasing with nanoparticle concentration.

All three simulations exhibit a temperature increase at the outlet of the system. Notably, the highest temperature increase was recorded for a concentration of 0.0015 wt.%, while the lowest was for pure water, which coincides with the results found in the experimental investigation. Additional simulations should be carried out in order to accurately comment on the trend of temperature increase with concentration but were not investigated in the present work due to time limitations. However, it is reasonable to assume from the results that the performance of the flat plane solar collector would improve compared to that of water for nanofluid of higher concentrations until a certain point.

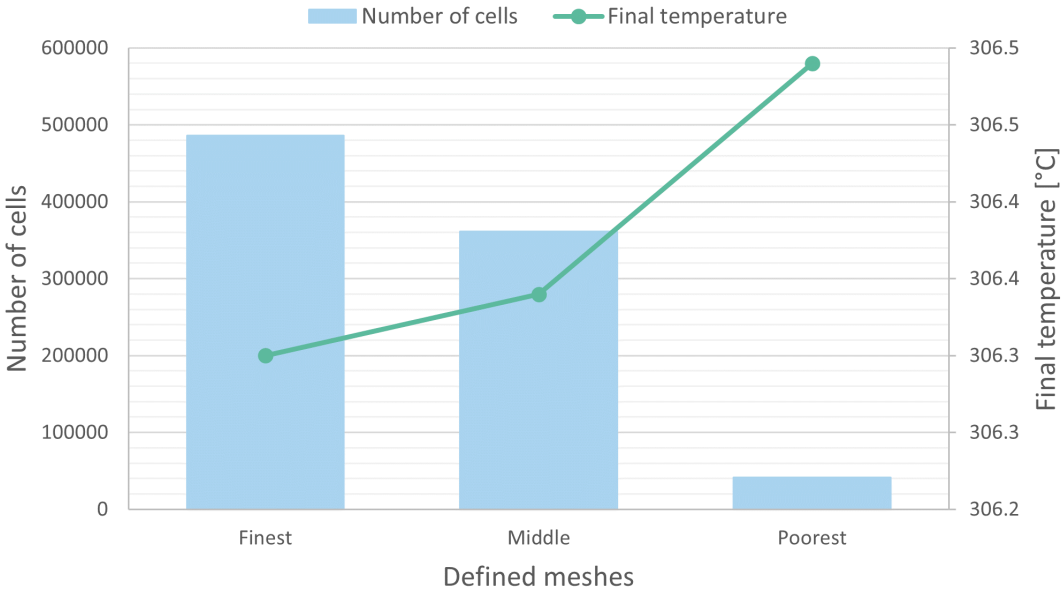

Figure 4.12: Comparison of outlet temperature and number of cells of the different meshes.

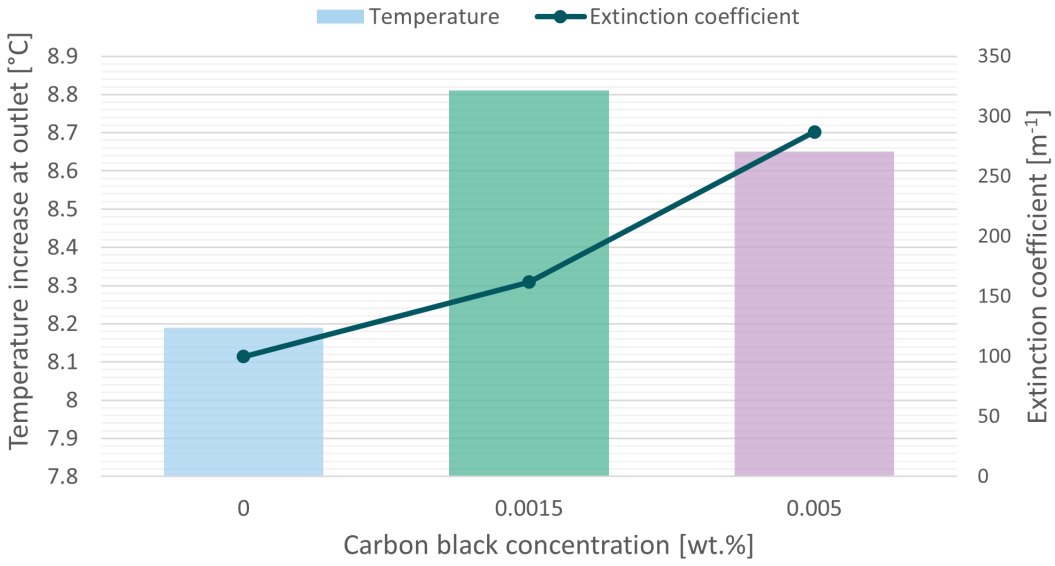

Figure 4.13: Temperature difference at the outlet of each simulation after 60 minutes in CFD physical time with an applied heat source corresponding to a radiance of $I_0 = 6000$ W/m^2. The graph also includes the applied extinction coefficient for each concentration.

The final temperature distribution through each flat plane after the ended simulation is presented in Fig. 4.14. The profiles reveal a similar distribution through each of the three planes. An obvious difference in temperature between the top and bottom layers is observed in all three situations. The largest difference is for 0.005 wt.%, which reached a temperature of 417.68 K at the surface. However, the simulation with this concentration had a lower final temperature at the outlet than the simulation of 0.0015 wt.%.

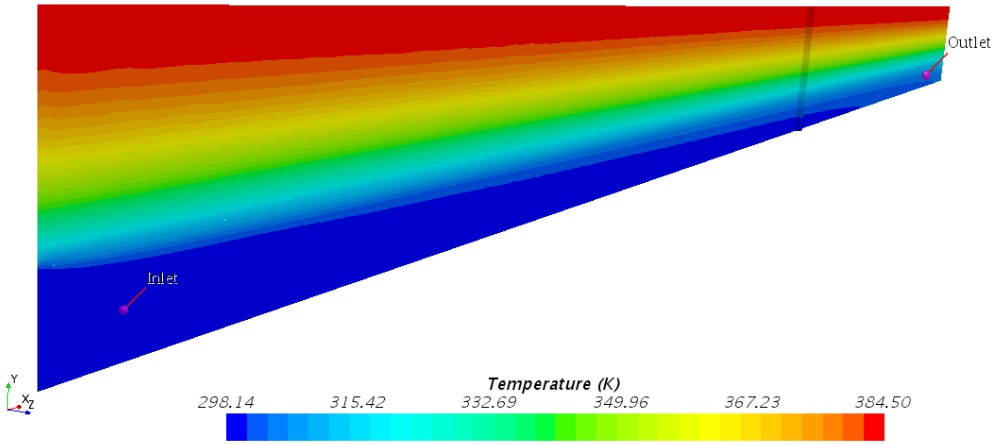

(a) Final temperature distribution after 60 minutes in physical time in CFD for water with $K = 100$ m^{-1}.

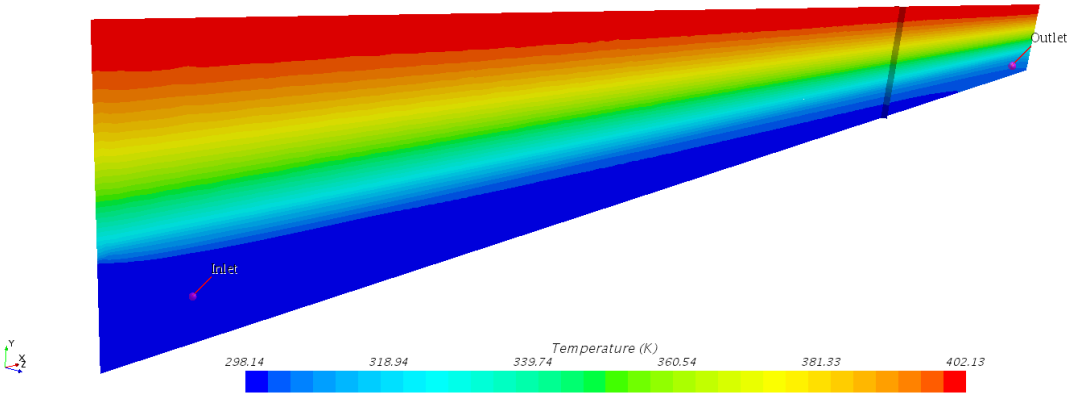

(b) Final temperature distribution after 60 minutes in physical time in CFD for 0.0015 wt.% with $K = 162$ m^{-1}.

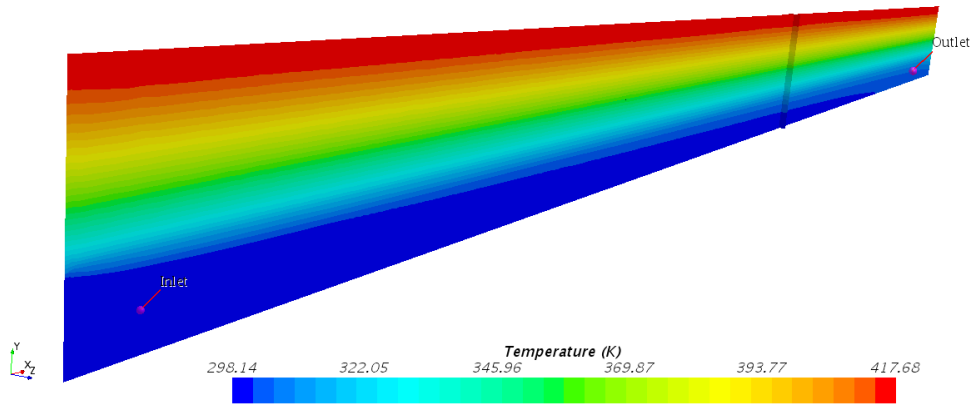

(c) Final temperature distribution after 60 minutes in physical time in CFD for 0.005 wt.% with $K = 287$ m^{-1}.

Figure 4.14: Temperature distribution of pure water and nanofluids of concentration 0.0015 wt.% and 0.005 wt.% through the flat plane geometry after 60 minutes in CFD physical time.

Surface Temperature

As mentioned, the surface temperature differed between the three simulations. The most significant increase was for the fluid with a concentration of 0.005 wt.%, which had an increased surface temperature of 119.53 °C after 60 minutes in CFD physical time. The final surface temperature exceeds the boiling temperature, but phase change was not included in the present model. Compared to the increase in surface temperature of the water, which was 86.35 °C, this equaled an increase of 33.18 °C by utilizing a very small volume fraction of nanoparticles. Also 0.0015 wt.% experienced an increment in surface temperature, with temperature increasing 103.98 °C. Table 4.4 summarizes the final surface temperature of each simulation.

Table 4.4: Surface temperature for water and fluids of concentration 0.0015 wt.% and 0.005 wt.%.

Nanofluid concentration [wt.%]	**Surface temperature [K]**
0	384.50
0.0015	402.13
0.005	417.68

Outlet Temperature

The outlet temperature of each simulated fluid is displayed in Fig. 4.13. As pointed out earlier, both 0.0015 wt.% and 0.005 wt.% experienced higher outlet temperatures after 60 minutes than water. The thermal enhancement was 7.43% and 5.16% compared to that of water for the two concentrations, respectively. In Table 4.5, the final outlet temperatures, as well as the thermal efficiency and enhancement of each fluid, are listed.

Table 4.5: Outlet temperature and corresponding thermal enhancement for water and fluids of concentration 0.0015 wt.% and 0.005 wt.%.

Concentration [wt.%]	**Outlet temperature [K]**	**Thermal efficiency [%]**	**Thermal enhancement [%]**
0	306.34	46.3	-
0.0015	306.96	49.7	7.43
0.005	306.80	48.6	5.16

Fig. 4.15 presents the temperature development of the nanofluids with concentration 0.0015 wt.% as a function of CFD physical time. The development at the outlet had a small delay at the beginning of the simulation while the absorbing fluid exposed to the heat flux was heating up. Next, a temperature increase is observed, resulting in higher temperatures at the outlet. It becomes evident from the figure that the rate of temperature development declines towards the end of the simulation. As with the temperature development in the laboratory experiments, this is a consequence of thermal equilibrium with the surroundings. A similar development was found for water and 0.005 wt.%, which are included in Appendix E.

Analysis of Thermal Efficiency

During his theoretical calculations on optical extinction characteristics of nanofluids in a DASC, Duan [39] estimated the temperature rise given different volume fractions, and hence different extinction coefficients, of plasmonic Ag nanofluids. The results showed an increasing temperature until a volume fraction of 0.05 vol.% with a corresponding extinction coefficient of 5311.63 m^{-1}. After a further increase in volume fraction, the performance started to decline.

A similar trend was observed during the numerical analysis of a nanofluid-based DASC by both Struchalin et al. [57] and Bardsgard et al. [58]. The research by Struchalin et al. revealed an optimal thermal efficiency at a concentration of 0.01 wt.% and K = 401 m^{-1}, with an efficiency increase of 5.8-37.9% with

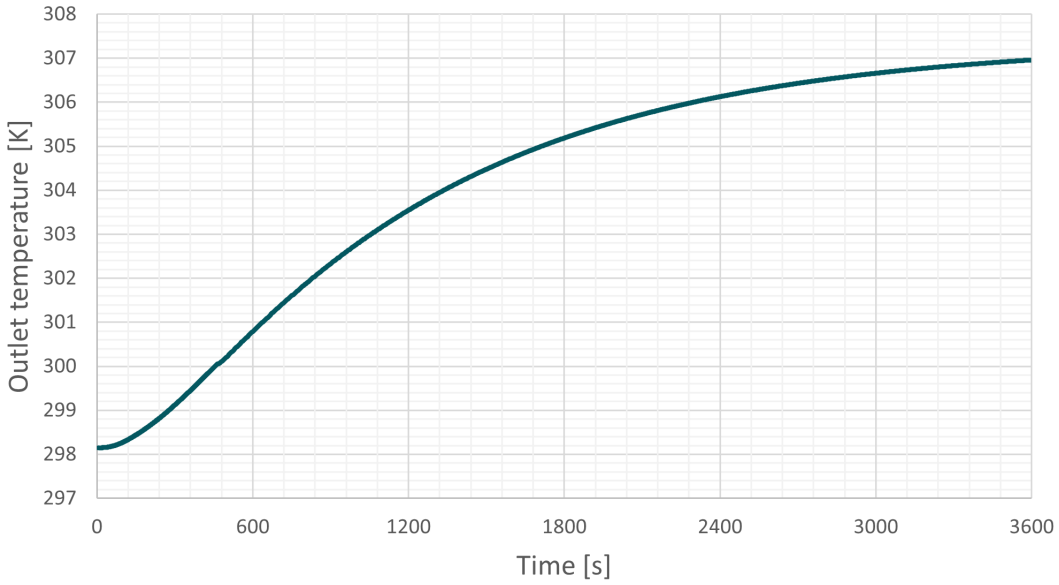

Figure 4.15: Temperature development of 0.0015 wt.% as a function of time.

increasing weight fractions up until this concentration. Bardsgard et al. found optimal efficiency at a volume fraction of 0.3 vol.%. This corresponds to a higher concentration than that found by Struchalin et al. and also a larger extinction coefficient.

The mentioned literature have in common that they point out that at large volume fractions, and thereby high extinction coefficient, the incident solar radiation is absorbed by the surface layer without penetrating deeper into the fluid. This creates high surface temperatures, which ultimately results in high thermal losses to the environment. This thermal leak is the main reason for the decline in the efficiency of systems with high concentrations of nanoparticles.

A similar conclusion can be drawn from the results of the numerical analysis in the present work. As shown, the increment in surface temperature strongly exceeds that of the outlet temperature of each investigated fluid and also continues to increase with higher concentrations. The decrease in outlet temperature of 0.005 wt.% compared to 0.0015 wt.% contradict the trend seen in the surface temperature of the same fluids and is likely due to the excessive convective heat losses as a function of the high extinction coefficient. However, at which concentration the efficiency actually starts to decline for this specific design requires more simulations of even higher weight fractions, as there is not enough basis for drawing a reliable

conclusion about the trend from only three concentrations.

In a numerical analysis of various nanofluids in a DASC, Luo et al. [41] reported increased efficiency with nanoparticle concentration. An increased outlet temperature of 30-100 K resulted in an improved collector efficiency of 2-25% compared to that of the base fluid. An increment in outlet temperature was also shown by Ladjevardi et al. [40] when numerically assessing the convective heat losses and the collector efficiency of a DASC utilizing graphite nanofluids. However, for volume fractions above 0.00025 vol.%, the solar collector also suffered from higher convective heat losses than the collector utilizing pure water. As with the previously mentioned literature, these findings are in good agreement with the results in the present work. Fluids of higher particle concentrations have better efficiency than the collector with pure water but also experience higher heat loss to the environment, thus making low volume fractions most desirable.

As mentioned, the flat plane design in the present section differs from the experimental setup in Section 3.1.1 in both design and light intensity. A comparison between the two is, therefore, challenging and unsatisfactory in some aspects. Still, despite the disparities, some similarities can be discussed between the two. As with the experimental results, the numerical assessment revealed thermal enhancement compared to that of water for nanofluids. The actual enhancement differed, likely caused by the unlike designs and, more specifically, the larger absorption area in the laboratory experiments. A resemblance is also found in the temperature development of the two methods. In both the experimental and the numerical techniques, the fluid seemed to reach a thermal equilibrium towards the end of the examination as a consequence of heat loss to the environment.

4.3.3 Summary

The aim of the numerical analysis was to compare outlet temperature increment and overall performance between three fluids of different compositions. Pure water and two concentrations of nanofluids were exposed to a heat flux of 6000 W/m^2 for 60 minutes in CFD computational time and revealed thermal enhancement at the outlet of 7.43% and 5.16% compared to water for 0.0015 wt.% and 0.005 wt.%, respectively. The fluid with a weight fraction of 0.0015 wt.% exhibited the highest performance among the studied fluids.

Although all fluids had a similar temperature development through the flat plane structure, there were notable differences in the final temperatures at the surface and the outlet. Most prominent was the temperature difference at the surfaces, which was highest for 0.005 wt.% with a final temperature of 417.68 K. Compared,

the final temperatures at the outlet were much lower, with a final temperature of 306.80 K and 5.16% thermal enhancement for the same concentration.

The results found in the literature suggest enhancement at the outlet for fluids of higher concentrations as well. However, beyond a certain concentration, the efficiency of the system is expected to decline as the extinction coefficient reaches high values. This decline occurs due to a thermal equilibrium between the fluid and the environment. Due to limited time, validation of the trend seen in the literature for the utilized design in the present work was not done.

4.4 Uncertainty Analysis

Scientific research is important for advancing technology and knowledge but is also prone to uncertainties and errors that affect the reliability of the results. The following section seeks to highlight and discuss the uncertainties that occurred when producing the results in the present work. Formulas for calculating the uncertainties are presented in Appendix A.

The experimental results were produced from laboratory experiments of seven fluids of different nanoparticle concentrations, which were prepared in the lab. Each fluid was subjected to five experiments to increase the credibility of the results. Different techniques and equipment were used to obtain the measurements, which were then analyzed to draw conclusions.

The accuracy of the instruments used for measurements is crucial for the uncertainty of the final results. Table 3.1 lists the given uncertainty of the equipment used to obtain results. Each fluid sample of different nanoparticle concentrations consisted of independent measurements of base fluid, CB nanoparticles, and SDS. Considering the fixed error of the precision scale, the uncertainty in the concentration of each fluid was calculated by Eq. (A.3) as $\pm$ 2.0%.

Five experiments were conducted on the respective nanofluid concentrations presented in this work to increase the reliability of the results. At the beginning of each experiment, a constant ambient room temperature was pursued. However, small deviations occurred, and the average start room temperature was 21.9 $\pm$ 0.316 °C. Further, uncertainty in inlet and outlet temperature measurements was estimated based on a fixed equipment error and a random sample error calculated by Eq. (A.1) from the five experiments of each fluid. This resulted in a variation error for each final temperature average.

Instrumental uncertainty was also found in the Perciflow Peristaltic pump, which transported the working fluid through the inner pipe of the experimental set-up. The fixed error affected the estimated mass flow rate as well as the random variation in the mean flow from experiments. By Eq. (A.1), the final flow rate was estimated as 403 ± 6.71 mL/h.

Radiance from the halogen lamps was measured by the Linshang Radiometer with an uncertainty of 1 W/m^2. The heat flux was measured three times and averaged at each distance from the light source, producing a sample variance estimated by Eq. (A.1). Calculated extinction coefficients were also affected by instrumental uncertainty in the radiometer and sample error in the average I_0 based on three radiance measurements. By Eq. (A.3), the uncertainty in extinction coefficient was calculated for each separate value.

The final thermal efficiency and enhancement of each fluid were deemed highly susceptible to uncertainty, as these parameters consist of the most independent variables. The efficiencies were calculated by Eq. (2.25), with associated uncertainty in mass flow, inlet and outlet temperature, and incident solar radiation. Similarly, the thermal enhancement, calculated from Eq. (2.26), had uncertainty in mass flow and temperature results. Consequently, the uncertainty in efficiency and enhancement was found by Eq. (A.3) for each concentration.

Chapter 5

Conclusion

In this thesis, the performance of a DASC with nanofluids of different carbon black concentrations as the absorbing fluid was experimentally and numerically investigated. The constructed systems were subjected to a light source for 60 minutes while the temperature development at the inlet and outlet of the systems was monitored. The temperature results were then analyzed and compared to find the optimal concentration with the best efficiency. The light source was simulated by two floodlight halogen lamps where the heat flux was measured for three distances from the lamps. All nanofluid samples used in the laboratory experiments contained a surfactant (SDS) to increase the stability of the fluid by preventing agglomeration.

Five laboratory experiments were conducted for each fluid composition at two distances from the light source, resulting in a total of 70 experiments. All six investigated nanofluids showed improved efficiencies compared to distilled water. The highest final outlet temperature was found for the nanofluid with 0.0015 wt.% CB concentration at 8 cm from the lamps. A temperature increase of 72.6 $\pm$ 0.705 °C after 60 minutes corresponded to an efficiency of 24.9 $\pm$ 4.78% and a thermal enhancement of 32.9 $\pm$ 4.17% compared to the reference distilled water results. The overall superior nanofluid was that of concentration 0.01 wt.% at 12 cm from the lamp. This fluid had the greatest efficiency of 27.9 $\pm$ 2.33%, which was calculated as 42.3 $\pm$ 4.49% thermal enhancement. All fluids of the same concentration had higher thermal efficiencies at the longer distance from the lamp.

A numerical analysis was executed in Simcenter STAR-CCM+ for a simplified flat-plane geometry containing water and two fluids corresponding to carbon black nanofluids of concentration 0.0015 wt.% and 0.005 wt.%. A volumetric heat source with a heat flux of 6000 W/m^2 was applied to simulate a distance of 10 cm from the light source. The extinction coefficient for each fluid was also experimentally estimated and applied. The simulations ran for 60 minutes in CFD physical time, after which the final temperatures were analyzed. The results revealed thermal enhancement for both nanofluids, with the highest enhancement of 7.43% for 0.0015 wt.%. In addition, a significant difference in temperature increment was noted between the surface and the outlet for each fluid.

The increment in temperatures in both the experimental and the numerical sections is a consequence of the improved properties of nanofluids. Important properties within heat transfer applications, such as thermal conductivity and convective heat transfer coefficient, are enhanced when dispersing nanoparticles in the base fluid, upgrading the application's performance. Another contributing factor is the higher extinction coefficient, allowing more incident solar radiation to be absorbed by the fluid. However, a high extinction coefficient is associated with high convection heat loss to the environment, which ultimately lowers thermal efficiency. Thus, carefully selecting the optimal nanoparticle concentration is crucial to mitigate such losses.

The experimental and numerical evaluation of nanofluids at varying concentrations in a DASC highlights the potential enhanced energy conversion and savings in diverse heat applications. The superior thermal efficiency exhibited by these fluids demonstrates a promising avenue for reducing energy consumption and promoting sustainable energy practices. Nevertheless, consideration of the cost implications of utilizing nanofluids, particularly in large-scale applications, is essential to understand their viability and competitiveness against other energy-saving solutions. Additionally, nanoparticles' potential health implications and environmental impact must be thoroughly examined. Future research should aim to further address their benefits and limitations to fully harness the potential of nanofluids in a greener energy sector.

Chapter 6

Future Work

Although the research on nanofluids and their potential within heat transfer applications have grown extensively in the last decade, several topics should be investigated further before utilizing them commercially. The list below is a suggestion for future work related to the scope of this thesis:

- Further investigation of long-term stability of CB nanofluids under the influence of different surfactants and environmental conditions.

- Study the impact of varying the CB concentration closer by additional laboratory and numerical experiments of nanofluid concentrations beyond those in this thesis.

- Develop a more realistic numerical model by constructing a geometry similar to the experimental setup. Improve the accuracy of the numerical model by including the outer glass wall and more reliable values for the thermal conductivity and the convective heat transfer.

- Investigation of the performance of CB nanoparticles in different base fluids, i.e. thermal oil-based nanofluids.

- Perform an economic analysis to understand the cost-competitiveness and the economic feasibility of implementing the present system in practical applications by considering factors such as system efficiency, potential energy savings, and cost of nanomaterial.

Bibliography

[1] *AR6 Synthesis Report: Climate Change 2023*. en. URL: https://www.ipcc.ch/report/ar6/syr/ (visited on 04/13/2023).

[2] *World Energy Outlook 2022 – Analysis - IEA*. URL: https://www.iea.org/reports/world-energy-outlook-2022 (visited on 04/12/2023).

[3] *FN: Verdens befolkning fortsetter å vokse, men tempoet avtar*. no$_N$*O*. July 2022. URL: https://www.fn.no/nyheter/fn-verdens-befolkning-fortsetter-aa-vokse-men-tempoet-avtar (visited on 04/13/2023).

[4] *Solar energy — Definition, Uses, Advantages, & Facts — Britannica*. en. Apr. 2023. URL: https://www.britannica.com/science/solar-energy (visited on 04/12/2023).

[5] Jens Christiansen. "Global Market Outlook for Solar Power". en. In: (2022).

[6] United Nations. *What is renewable energy?* en. Publisher: United Nations. URL: https://www.un.org/en/climatechange/what-is-renewable-energy (visited on 04/27/2023).

[7] *2H 2022 Levelized Cost of Electricity Update*. en-US. Section: Report. Dec. 2022. URL: https://about.bnef.com/blog/2h-2022-levelized-cost-of-electricity-update/ (visited on 04/27/2023).

[8] Adeola Borode, Noor Ahmed, and Peter Olubambi. "A review of solar collectors using carbon-based nanofluids". en. In: *Journal of Cleaner Production* 241 (Dec. 2019), p. 118311. ISSN: 0959-6526. DOI: 10.1016/j.jclepro.2019.118311. URL: https://www.sciencedirect.com/science/article/pii/S0959652619331816 (visited on 11/23/2022).

[9] *Differences Between Solar PV and Solar Thermal — GreenMatch*. en-GB. URL: https://www.greenmatch.co.uk/blog/2016/04/differences-between-solar-photovoltaics-and-solar-thermal (visited on 04/27/2023).

[10] Salma Parvin, Rehena Nasrin, and M. A. Alim. "Heat transfer and entropy generation through nanofluid filled direct absorption solar collector". en. In: *International Journal of Heat and Mass Transfer* 71 (Apr. 2014), pp. 386–395. ISSN: 0017-9310. DOI: 10.1016/j.ijheatmasstransfer.2013.12.

043. URL: https://www.sciencedirect.com/science/article/pii/S0017931013010879 (visited on 11/17/2022).

[11] Pankaj Raj and Sudhakar Subudhi. "A review of studies using nanofluids in flat-plate and direct absorption solar collectors". en. In: *Renewable and Sustainable Energy Reviews* 84 (Mar. 2018), pp. 54–74. ISSN: 1364-0321. DOI: 10.1016/j.rser.2017.10.012. URL: https://www.sciencedirect.com/science/article/pii/S1364032117313874 (visited on 11/17/2022).

[12] Nipun Goel, Robert A. Taylor, and Todd Otanicar. "A review of nanofluid-based direct absorption solar collectors: Design considerations and experiments with hybrid PV/Thermal and direct steam generation collectors". en. In: *Renewable Energy* 145 (Jan. 2020), pp. 903–913. ISSN: 0960-1481. DOI: 10.1016/j.renene.2019.06.097. URL: https://www.sciencedirect.com/science/article/pii/S0960148119309206 (visited on 11/29/2022).

[13] R. Saidur et al. "Evaluation of the effect of nanofluid-based absorbers on direct solar collector". en. In: *International Journal of Heat and Mass Transfer* 55.21 (Oct. 2012), pp. 5899–5907. ISSN: 0017-9310. DOI: 10.1016/j.ijheatmasstransfer.2012.05.087. URL: https://www.sciencedirect.com/science/article/pii/S0017931012004188 (visited on 11/17/2022).

[14] Himanshu Tyagi, Patrick Phelan, and Ravi Prasher. "Predicted Efficiency of a Low-Temperature Nanofluid-Based Direct Absorption Solar Collector". In: *Journal of Solar Energy Engineering* 131.4 (Sept. 2009). ISSN: 0199-6231. DOI: 10.1115/1.3197562. URL: https://doi.org/10.1115/1.3197562 (visited on 12/13/2022).

[15] Caiyan Qin et al. "Optimization of a direct absorption solar collector with blended plasmonic nanofluids". en. In: *Solar Energy* 150 (July 2017), pp. 512–520. ISSN: 0038-092X. DOI: 10.1016/j.solener.2017.05.007. URL: https://www.sciencedirect.com/science/article/pii/S0038092X17303845 (visited on 12/06/2022).

[16] Todd P. Otanicar, Patrick E. Phelan, and Jay S. Golden. "Optical properties of liquids for direct absorption solar thermal energy systems". en. In: *Solar Energy* 83.7 (July 2009), pp. 969–977. ISSN: 0038-092X. DOI: 10.1016/j.solener.2008.12.009. URL: https://www.sciencedirect.com/science/article/pii/S0038092X08003496 (visited on 05/11/2023).

[17] Khalil Khanafer and Kambiz Vafai. "A review on the applications of nanofluids in solar energy field". en. In: *Renewable Energy* 123 (Aug. 2018), pp. 398–406. ISSN: 0960-1481. DOI: 10.1016/j.renene.2018.01.097. URL: https://www.sciencedirect.com/science/article/pii/S0960148118301071 (visited on 11/29/2022).

[18] Stephen U S Choi and J A Eastman. "ENHANCING THERMAL CONDUCTIVITY OF FLUIDS WITH NANOPARTICLES". en. In: (), p. 9.

[19] Wei Yu and Huaqing Xie. “A Review on Nanofluids: Preparation, Stability Mechanisms, and Applications”. en. In: *Journal of Nanomaterials* 2012 (2012), pp. 1–17. ISSN: 1687-4110, 1687-4129. DOI: 10.1155/2012/435873. URL: http://www.hindawi.com/journals/jnm/2012/435873/ (visited on 10/25/2022).

[20] Zafar Said et al. “Recent advances on the fundamental physical phenomena behind stability, dynamic motion, thermophysical properties, heat transport, applications, and challenges of nanofluids”. en. In: *Physics Reports*. Recent advances on the fundamental physical phenomena behind stability, dynamic motion, thermophysical properties, heat transport, applications, and challenges of nanofluids 946 (Feb. 2022), pp. 1–94. ISSN: 0370-1573. DOI: 10.1016/j.physrep.2021.07.002. URL: https://www.sciencedirect.com/science/article/pii/S0370157321002775 (visited on 11/24/2022).

[21] S.A. Angayarkanni and John Philip. “Review on thermal properties of nanofluids: Recent developments”. en. In: *Advances in Colloid and Interface Science* 225 (Nov. 2015), pp. 146–176. ISSN: 00018686. DOI: 10.1016/j.cis.2015.08.014. URL: https://linkinghub.elsevier.com/retrieve/pii/S0001868615001633 (visited on 10/25/2022).

[22] Tahereh B. Gorji and A. A. Ranjbar. “Thermal and exergy optimization of a nanofluid-based direct absorption solar collector”. en. In: *Renewable Energy* 106 (June 2017), pp. 274–287. ISSN: 0960-1481. DOI: 10.1016/j.renene.2017.01.031. URL: https://www.sciencedirect.com/science/article/pii/S0960148117300319 (visited on 11/29/2022).

[23] Mohammad Hossein Ahmadi et al. “A review of thermal conductivity of various nanofluids”. en. In: *Journal of Molecular Liquids* 265 (Sept. 2018), pp. 181–188. ISSN: 0167-7322. DOI: 10.1016/j.molliq.2018.05.124. URL: https://www.sciencedirect.com/science/article/pii/S0167732218304264 (visited on 01/19/2023).

[24] H. Javaniyan Jouybari, M. Eshagh Nimvari, and S. Saedodin. “Thermal performance evaluation of a nanofluid-based flat-plate solar collector”. en. In: *Journal of Thermal Analysis and Calorimetry* 137.5 (Sept. 2019), pp. 1757–1774. ISSN: 1588-2926. DOI: 10.1007/s10973-019-08077-z. URL: https://doi.org/10.1007/s10973-019-08077-z (visited on 11/24/2022).

[25] Sayantan Mukherjee and Somjit Paria. “Preparation and Stability of Nanofluids-A Review”. In: *IOSR Journal of Mechanical and Civil Engineering (IOSR-JMCE)* 9 (Oct. 2013), pp. 63–69. DOI: 10.9790/1684-0926369.

[26] Nurettin Sezer, Muataz A. Atieh, and Muammer Koç. “A comprehensive review on synthesis, stability, thermophysical properties, and characterization of nanofluids”. en. In: *Powder Technology* 344 (Feb. 2019), pp. 404–431. ISSN: 0032-5910. DOI: 10.1016/j.powtec.2018.12.016. URL: https:

//www.sciencedirect.com/science/article/pii/S0032591018310532 (visited on 11/17/2022).

[27] Yujin Hwang et al. "Production and dispersion stability of nanoparticles in nanofluids". en. In: *Powder Technology* 186.2 (Aug. 2008), pp. 145–153. ISSN: 0032-5910. DOI: 10.1016/j.powtec.2007.11.020. URL: https://www.sciencedirect.com/science/article/pii/S0032591007005694 (visited on 01/19/2023).

[28] Georgios M. Kontogeorgis and Søren Kiil. *Introduction to Applied Colloid and Surface Chemistry*. John Wiley & Sons, Ltd., 2016.

[29] Hugh D. Young and Roger A. Freedman. *University Physics with Modern Physics*. Fourteenth.

[30] Lin Qiu et al. "A review of recent advances in thermophysical properties at the nanoscale: From solid state to colloids". en. In: *Physics Reports*. A review of recent advances in thermophysical properties at the nanoscale: From solid state to colloids 843 (Feb. 2020), pp. 1–81. ISSN: 0370-1573. DOI: 10.1016/j.physrep.2019.12.001. URL: https://www.sciencedirect.com/science/article/pii/S0370157319304016 (visited on 05/01/2023).

[31] Ifeoluwa Wole-osho et al. "Nanofluids in Solar Thermal Collectors: Review and Limitations". en. In: *International Journal of Thermophysics* 41.11 (Sept. 2020), p. 157. ISSN: 1572-9567. DOI: 10.1007/s10765-020-02737-1. URL: https://doi.org/10.1007/s10765-020-02737-1 (visited on 11/29/2022).

[32] *Viscosity — Definition, Facts, Formula, Units, & Examples — Britannica*. en. Feb. 2023. URL: https://www.britannica.com/science/viscosity (visited on 03/23/2023).

[33] Kazem Bashirnezhad et al. "Viscosity of nanofluids: A review of recent experimental studies". en. In: *International Communications in Heat and Mass Transfer* 73 (Apr. 2016), pp. 114–123. ISSN: 0735-1933. DOI: 10.1016/j.icheatmasstransfer.2016.02.005. URL: https://www.sciencedirect.com/science/article/pii/S0735193316300422 (visited on 02/15/2023).

[34] G. K. Batchelor. "The effect of Brownian motion on the bulk stress in a suspension of spherical particles". en. In: *Journal of Fluid Mechanics* 83.1 (Nov. 1977). Publisher: Cambridge University Press, pp. 97–117. ISSN: 1469-7645, 0022-1120. DOI: 10.1017/S0022112077001062. URL: https://www.cambridge.org/core/journals/journal-of-fluid-mechanics/article/effect-of-brownian-motion-on-the-bulk-stress-in-a-suspension-of-spherical-particles/72B16FA20D2A14415CDED6A4F042809F (visited on 05/11/2023).

[35] Dongxiao Han et al. "Thermal properties of carbon black aqueous nanofluids for solar absorption". en. In: *Nanoscale Research Letters* 6.1 (Dec. 2011), p. 457. ISSN: 1556-276X. DOI: 10.1186/1556-276X-6-457. URL: https:

//nanoscalereslett.springeropen.com/articles/10.1186/1556-276X-6-457 (visited on 10/25/2022).

[36] Todd P. Otanicar et al. "Nanofluid-based direct absorption solar collector". en. In: *Journal of Renewable and Sustainable Energy* 2.3 (May 2010), p. 033102. ISSN: 1941-7012. DOI: 10.1063/1.3429737. URL: http://aip.scitation.org/doi/10.1063/1.3429737 (visited on 01/10/2023).

[37] Alibakhsh Kasaeian et al. "Performance evaluation and nanofluid using capability study of a solar parabolic trough collector". en. In: *Energy Conversion and Management* 89 (Jan. 2015), pp. 368–375. ISSN: 0196-8904. DOI: 10.1016/j.enconman.2014.09.056. URL: https://www.sciencedirect.com/science/article/pii/S0196890414008577 (visited on 03/20/2023).

[38] M. Karami et al. "A new application of carbon nanotubes nanofluid as working fluid of low-temperature direct absorption solar collector". en. In: *Solar Energy Materials and Solar Cells* 121 (Feb. 2014), pp. 114–118. ISSN: 0927-0248. DOI: 10.1016/j.solmat.2013.11.004. URL: https://www.sciencedirect.com/science/article/pii/S0927024813005746 (visited on 01/10/2023).

[39] Huiling Duan. "Analysis on the extinction properties of nanofluids for direct solar absorption". en. In: *Physica E: Low-dimensional Systems and Nanostructures* 120 (June 2020), p. 114046. ISSN: 1386-9477. DOI: 10.1016/j.physe.2020.114046. URL: https://www.sciencedirect.com/science/article/pii/S1386947719317369 (visited on 02/10/2023).

[40] S. M. Ladjevardi et al. "Applicability of graphite nanofluids in direct solar energy absorption". en. In: *Solar Energy* 94 (Aug. 2013), pp. 327–334. ISSN: 0038-092X. DOI: 10.1016/j.solener.2013.05.012. URL: https://www.sciencedirect.com/science/article/pii/S0038092X13001953 (visited on 01/10/2023).

[41] Zhongyang Luo et al. "Performance improvement of a nanofluid solar collector based on direct absorption collection (DAC) concepts". en. In: *International Journal of Heat and Mass Transfer* 75 (Aug. 2014), pp. 262–271. ISSN: 0017-9310. DOI: 10.1016/j.ijheatmasstransfer.2014.03.072. URL: https://www.sciencedirect.com/science/article/pii/S0017931014002786 (visited on 01/10/2023).

[42] Yunus A. Cengel and Michael A. Boles. *Thermodynamics: An Engineering Approach*. 2nd. McGraw-Hill, 1994.

[43] Warren L. McCabe, Julian C. Smith, and Peter Harriott. *Unit Operations of Chemical Engineering*. 7th. McGraw-Hill, 2005.

[44] Nick Connor. *What is Radiation Heat Transfer - Definition*. en-us. May 2019. URL: https://www.thermal-engineering.org/what-is-radiation-heat-transfer-definition/ (visited on 01/11/2023).

[45] Robert L. Jaffe and Washington Taylor. *The Physics of Energy*. Cambridge University Press, 2018.

[46] Nick Connor. *What is Heat Capacity - Specific Heat Capacity - Definition*. en-us. May 2019. URL: https://www.thermal-engineering.org/what-is-heat-capacity-specific-heat-capacity-definition/ (visited on 01/23/2023).

[47] Jolanta Sobczak et al. "Thermophysical profile of ethylene glycol based nanofluids containing two types of carbon black nanoparticles with different specific surface areas". en. In: *Journal of Molecular Liquids* 326 (Mar. 2021), p. 115255. ISSN: 0167-7322. DOI: 10.1016/j.molliq.2020.115255. URL: https://www.sciencedirect.com/science/article/pii/S0167732220374973 (visited on 01/24/2023).

[48] Yoichi Takahashi and Edgar F. Westrum. "Glassy Carbon low-temperature thermodynamic properties". en. In: *The Journal of Chemical Thermodynamics* 2.6 (Nov. 1970), pp. 847–854. ISSN: 0021-9614. DOI: 10.1016/0021-9614(70)90028-5. URL: https://www.sciencedirect.com/science/article/pii/0021961470900285 (visited on 03/21/2023).

[49] A. I Lutcov, V. I Volga, and B. K Dymov. "Thermal conductivity, electric resistivity and specific heat of dense graphites". en. In: *Carbon* 8.6 (Dec. 1970), pp. 753–760. ISSN: 0008-6223. DOI: 10.1016/0008-6223(70)90100-4. URL: https://www.sciencedirect.com/science/article/pii/0008622370901004 (visited on 03/21/2023).

[50] Pham Van Trinh et al. "Experimental study on the thermal conductivity of ethylene glycol-based nanofluid containing Gr-CNT hybrid material". en. In: *Journal of Molecular Liquids* 269 (Nov. 2018), pp. 344–353. ISSN: 0167-7322. DOI: 10.1016/j.molliq.2018.08.071. URL: https://www.sciencedirect.com/science/article/pii/S0167732218314326 (visited on 03/22/2023).

[51] S. khosrojerdi, A. M. Lavasani, and M. Vakili. "Experimental study of photothermal specifications and stability of graphene oxide nanoplatelets nanofluid as working fluid for low-temperature Direct Absorption Solar Collectors (DASCs)". en. In: *Solar Energy Materials and Solar Cells* 164 (May 2017), pp. 32–39. ISSN: 0927-0248. DOI: 10.1016/j.solmat.2017.02.007. URL: https://www.sciencedirect.com/science/article/pii/S0927024817300582 (visited on 03/22/2023).

[52] Vikrant Khullar et al. "Harvesting solar thermal energy through nanofluid-based volumetric absorption systems". en. In: *International Journal of Heat and Mass Transfer* 77 (Oct. 2014), pp. 377–384. ISSN: 0017-9310. DOI: 10.1016/j.ijheatmasstransfer.2014.05.023. URL: https://www.sciencedirect.com/science/article/pii/S0017931014004232 (visited on 01/17/2023).

[53] Linna V. Nguyen et al. "Direct absorption solar collector: Use of nanofluids and biodegradable colloids". en. In: *International Journal of Thermal Sciences* 190 (Aug. 2023), p. 108292. ISSN: 1290-0729. DOI: 10.1016/j.ijthermalsci.2023.108292. URL: https://www.sciencedirect.com/science/article/pii/S1290072923001539 (visited on 04/30/2023).

[54] Edda Torsdottir Ulset. "Utilizing Solar Vapour Energy by Use of Nanofluids in a Direct Absorption Solar Collector". eng. Accepted: 2018-04-18T14:00:19Z. MA thesis. The University of Bergen, Jan. 2018. URL: https://bora.uib.no/bora-xmlui/handle/1956/17628 (visited on 01/24/2023).

[55] Nick Connor. *What is Reynolds Number - Definition*. en-us. May 2019. URL: https://www.thermal-engineering.org/what-is-reynolds-number-definition/ (visited on 03/30/2023).

[56] A. Kosinska, B. V. Balakin, and P. Kosinski. "Use of biodegradable colloids and carbon black nanofluids for solar energy applications". In: *AIP Advances* 11.5 (May 2021). Publisher: American Institute of Physics, p. 055214. DOI: 10.1063/5.0053258. URL: https://aip.scitation.org/doi/10.1063/5.0053258 (visited on 02/10/2023).

[57] P. G. Struchalin et al. "Performance of a tubular direct absorption solar collector with a carbon-based nanofluid". en. In: *International Journal of Heat and Mass Transfer* 179 (Nov. 2021), p. 121717. ISSN: 0017-9310. DOI: 10.1016/j.ijheatmasstransfer.2021.121717. URL: https://www.sciencedirect.com/science/article/pii/S0017931021008231 (visited on 03/23/2023).

[58] Runa By Bårdsgård et al. "Eulerian CFD model of direct absorption solar collector with nanofluid". eng. In: *033701* (2020). Accepted: 2021-05-27T08:41:16Z Publisher: AIP. ISSN: 1941-7012. DOI: 10.1063/1.5144737. URL: https://bora.uib.no/bora-xmlui/handle/11250/2756545 (visited on 01/25/2023).

[59] Maryam Karami, Shahram Delfani, and Mostafa Esmaeili. "Effect of V-shaped rib roughness on the performance of nanofluid-based direct absorption solar collectors". en. In: *Journal of Thermal Analysis and Calorimetry* 138.1 (Oct. 2019), pp. 559–572. ISSN: 1388-6150, 1588-2926. DOI: 10.1007/s10973-019-08129-4. URL: http://link.springer.com/10.1007/s10973-019-08129-4 (visited on 01/10/2023).

[60] Robert A. Taylor et al. "Nanofluid optical property characterization: towards efficient direct absorption solar collectors". en. In: *Nanoscale Research Letters* 6.1 (Mar. 2011), p. 225. ISSN: 1556-276X. DOI: 10.1186/1556-276X-6-225. URL: https://doi.org/10.1186/1556-276X-6-225 (visited on 03/23/2023).

[61] Z. Said et al. "Analyses of exergy efficiency and pumping power for a conventional flat plate solar collector using SWCNTs based nanofluid". en. In: *Energy and Buildings* 78 (Aug. 2014), pp. 1–9. ISSN: 0378-7788. DOI: 10.1016/j.enbuild.2014.03.061. URL: https://www.sciencedirect.com/science/article/pii/S0378778814002813 (visited on 04/11/2023).

[62] SimScale. *What is CFD — What is Computational Fluid Dynamics?* en. URL: https://www.simscale.com/docs/simwiki/cfd-computational-fluid-dynamics/what-is-cfd-computational-fluid-dynamics/ (visited on 01/25/2023).

[63] Clayton T. Crowe et al. *Multiphase Flows with Droplets and Particles*. Second. CRC Press, Taylor and Francis Group, 2012.

[64] STAR-CCM+. *Siemens Software Simcenter.*

[65] Edda T. Ulset et al. "Photothermal boiling in aqueous nanofluids". en. In: *Nano Energy* 50 (Aug. 2018), pp. 339–346. ISSN: 2211-2855. DOI: 10.1016/j.nanoen.2018.05.050. URL: https://www.sciencedirect.com/science/article/pii/S2211285518303653 (visited on 01/18/2023).

[66] *Solar power meterLS122 infrared power meter manufacturer-Linshang*. URL: https://www.linshangtech.com/product/LS122_EN.html (visited on 02/22/2023).

[67] *Operation manual - Peristaltic pump - tubing pump*. URL: https://www.lambda-instruments.com/fileadmin/user_upload/PDF/LAMBDA_Pumps/Peristaltic_Pump-Tubing_Pump_LAMBDA_MAXIFLOW_Operation_Manual.pdf.

[68] Amirhossein Zamzamian et al. "Experimental investigation of forced convective heat transfer coefficient in nanofluids of Al2O3/EG and CuO/EG in a double pipe and plate heat exchangers under turbulent flow". en. In: *Experimental Thermal and Fluid Science* 35.3 (Apr. 2011), pp. 495–502. ISSN: 0894-1777. DOI: 10.1016/j.expthermflusci.2010.11.013. URL: https://www.sciencedirect.com/science/article/pii/S089417771000227X (visited on 03/28/2023).

[69] S. Delfani, M. Karami, and M. A. Akhavan- Behabadi. "Performance characteristics of a residential-type direct absorption solar collector using MWCNT nanofluid". en. In: *Renewable Energy* 87 (Mar. 2016), pp. 754–764. ISSN: 0960-1481. DOI: 10.1016/j.renene.2015.11.004. URL: https://www.sciencedirect.com/science/article/pii/S0960148115304237 (visited on 11/29/2022).

[70] Albert Polman. "Solar Steam Nanobubbles". en. In: *ACS Nano* 7.1 (Jan. 2013), pp. 15–18. ISSN: 1936-0851, 1936-086X. DOI: 10.1021/nn305869y. URL: https://pubs.acs.org/doi/10.1021/nn305869y (visited on 05/10/2023).

[71] M. Vakili et al. “Photothermal properties of graphene nanoplatelets nanofluid for low-temperature direct absorption solar collectors”. en. In: *Solar Energy Materials and Solar Cells* 152 (Aug. 2016), pp. 187–191. ISSN: 0927-0248. DOI: 10.1016/j.solmat.2016.01.038. URL: https://www.sciencedirect.com/science/article/pii/S0927024816000519 (visited on 05/10/2023).

[72] Hemant Kumar Gupta, Ghanshyam Das Agrawal, and Jyotirmay Mathur. “An experimental investigation of a low temperature Al2O3-H2O nanofluid based direct absorption solar collector”. en. In: *Solar Energy* 118 (Aug. 2015), pp. 390–396. ISSN: 0038-092X. DOI: 10.1016/j.solener.2015.04.041. URL: https://www.sciencedirect.com/science/article/pii/S0038092X15002479 (visited on 05/11/2023).

[73] Jay L. Devore and Kenneth N. Berk. *Modern Mathematical Statistics with Applications*. Second. Springer, 2018.

[74] *Averaging, Errors and Uncertainty*. URL: https://www.physics.upenn.edu/sites/default/files/Managing%20Errors%20and%20Uncertainty.pdf.

[75] *Water - Specific Heat vs. Temperature*. URL: https://www.engineeringtoolbox.com/specific-heat-capacity-water-d_660.html (visited on 05/09/2023).

[76] *Water - Density, Specific Weight and Thermal Expansion Coefficients*. URL: https://www.engineeringtoolbox.com/water-density-specific-weight-d_595.html (visited on 05/09/2023).

Appendices

Appendix A

Uncertainty in Measurements

The following equations were used to estimate the uncertainty in the experimental results.

Mean

The sample mean $\bar{x}$ is defined as [73]

$$\bar{x} = \frac{x_1 + x_2 + \ldots + x_n}{n} = \frac{1}{n}\sum_{i=1}^{n} x_i, \tag{A.1}$$

where, $x_1, x_2, \ldots, x_n$ are the observations.

Standard deviation

Standard deviation is defined as

$$S = \sqrt{\frac{1}{n}\sum_{i=1}^{n}(x_i - \bar{x})^2}, \tag{A.2}$$

where n is the number of observations.

Independent Variables

For an experimental quantity f consisting of independent variables $x, y, z, \ldots, i$ with corresponding uncertainties $\Delta x, \Delta y, \Delta z, \ldots, \Delta i$ the standard deviation is given by [74]

$$\Delta f = \sqrt{\left(\frac{\delta f}{\delta x}\Delta x\right)^2 + \left(\frac{\delta f}{\delta y}\Delta y\right)^2 + \left(\frac{\delta f}{\delta z}\Delta z\right)^2 + \cdots + \left(\frac{\delta f}{\delta i}\Delta i\right)^2}, \tag{A.3}$$

where Δf is the standard deviation of f.

Appendix B

Data from Experiments

The data displayed in this appendix is obtained by the experimental method explained in Section 3.1.4.

B.1 12 cm from Light Source

Experiment	$\mathbf{T_{o,start}}$ [°C]	$\mathbf{T_{o,end}}$ [°C]	$\mathbf{\Delta T}$ [°C]
1	22.9	65.0	42.1
2	20.3	64.6	44.3
3	21.6	66.9	45.3
4	21.6	62.2	40.6
5	23.0	66.8	43.8
Average	21.9	65.1	43.2

Table B.1: Experimental temperature results from each experiment with distilled water.

Experiment	$\mathbf{T_{o,start}}$ [°C]	$\mathbf{T_{o,end}}$ [°C]	$\mathbf{\Delta T}$ [°C]
1	22.8	81.3	58.5
2	21.6	84.2	62.6
3	22.2	84.5	62.3
4	24.3	83.4	59.1
5	22.4	83.7	61.3
Average	22.7	83.4	60.8

Table B.2: Experimental temperature results from each experiment with a nanofluid concentration of 0.0015 wt.%.

Experiment	$\mathbf{T_{o,start}}$ [°C]	$\mathbf{T_{o,end}}$ [°C]	$\mathbf{\Delta T}$ [°C]
1	21.8	87.9	66.1
2	22.0	85.4	63.4
3	23.4	82.2	58.8
4	22.4	81.1	58.7
5	22.3	83.5	61.2
Average	22.4	84.0	61.6

Table B.3: Experimental temperature results from each experiment with a nanofluid concentration of 0.005 wt.%.

Experiment	$\mathbf{T_{o,start}}$ [°C]	$\mathbf{T_{o,end}}$ [°C]	$\mathbf{\Delta T}$ [°C]
1	22.9	85.0	62.1
2	21.7	84.9	63.2
3	23.1	82.3	59.2
4	21.6	86.6	65.0
5	22.9	83.4	60.5
Average	22.4	84.4	62.0

Table B.4: Experimental temperature results from each experiment with a nanofluid concentration of 0.01 wt.%.

Experiment	$\mathbf{T_{o,start}}$ [°C]	$\mathbf{T_{o,end}}$ [°C]	$\mathbf{\Delta T}$ [°C]
1	22.4	83.9	61.5
2	23.0	80.5	57.5
3	19.4	80.5	61.1
4	21.8	81.7	59.9
5	22.8	83.9	61.1
Average	21.9	82.1	60.2

Table B.5: Experimental temperature results from each experiment with a nanofluid concentration of 0.015 wt.%.

Experiment	$\mathbf{T_{o,start}}$ [°C]	$\mathbf{T_{o,end}}$ [°C]	$\mathbf{\Delta T}$ [°C]
1	20.6	80.2	59.6
2	21.6	79.2	57.6
3	23.4	82.9	59.5
4	20.2	79.7	59.5
5	22.1	79.9	57.8
Average	21.6	80.4	58.8

Table B.6: Experimental temperature results from each experiment with a nanofluid concentration of 0.02 wt.%.

Experiment	$\mathbf{T_{o,start}}$ [°C]	$\mathbf{T_{o,end}}$ [°C]	$\mathbf{\Delta T}$ [°C]
1	22.9	83.0	60.1
2	21.2	83.3	62.1
3	21.5	83.6	62.1
4	24.2	82.9	58.7
5	22.6	81.4	58.8
Average	22.5	82.8	60.4

Table B.7: Experimental temperature results from each experiment with a nanofluid concentration of 0.05 wt.%.

B.2 8 cm from Light Source

Experiment	$\mathbf{T_{o,start}}$ [°C]	$\mathbf{T_{o,end}}$ [°C]	$\mathbf{\Delta T}$ [°C]
1	22.0	74.9	52.9
2	23.2	73.5	50.3
3	21.7	75.7	54.0
4	20.8	78.7	57.9
5	20.8	78.6	57.8
Average	21.7	76.3	54.6

Table B.8: Experimental temperature results from each experiment with distilled water.

Experiment	$\mathbf{T_{o,start}}$ [°C]	$\mathbf{T_{o,end}}$ [°C]	$\mathbf{\Delta T}$ [°C]
1	23.7	96.0	72.3
2	23.9	96.1	72.2
3	22.5	96.0	73.5
4	24.3	96.2	71.9
5	22.8	96.1	73.3
Average	23.4	96.1	72.6

Table B.9: Experimental temperature results from each experiment with a nanofluid concentration of 0.0015 wt.%.

Experiment	$\mathbf{T_{o,start}}$ [°C]	$\mathbf{T_{o,end}}$ [°C]	$\mathbf{\Delta T}$ [°C]
1	22.3	94.6	72.3
2	21.6	89.2	67.6
3	23.1	94.4	71.3
4	22.0	88.7	66.7
5	22.6	88.4	65.8
Average	22.3	91.1	68.7

Table B.10: Experimental temperature results from each experiment with a nanofluid concentration of 0.005 wt.%.

Experiment	$\mathbf{T_{o,start}}$ [°C]	$\mathbf{T_{o,end}}$ [°C]	$\mathbf{\Delta T}$ [°C]
1	21.4	90.4	69.0
2	21.6	90.5	68.9
3	22.6	89.1	66.5
4	21.5	88.6	67.1
5	22.2	89.4	67.2
Average	21.9	89.6	67.7

Table B.11: Experimental temperature results from each experiment with a nanofluid concentration of 0.01 wt.%.

Experiment	$\mathbf{T_{o,start}}$ [°C]	$\mathbf{T_{o,end}}$ [°C]	$\mathbf{\Delta T}$ [°C]
1	21.6	89.3	67.7
2	23.8	90.1	66.3
3	21.7	88.5	66.8
4	22.6	90.0	67.4
5	21.7	88.8	67.1
Average	22.3	89.3	67.1

Table B.12: Experimental temperature results from each experiment with a nanofluid concentration of 0.015 wt.%.

Experiment	$\mathbf{T_{o,start}}$ [°C]	$\mathbf{T_{o,end}}$ [°C]	$\mathbf{\Delta T}$ [°C]
1	24.3	89.0	64.7
2	23.0	87.7	64.7
3	21.8	87.6	65.8
4	19.4	88.1	68.7
5	21.4	87.5	66.1
Average	22.0	88.0	66.0

Table B.13: Experimental temperature results from each experiment with a nanofluid concentration of 0.02 wt.%.

Experiment	$\mathbf{T_{o,start}}$ [°C]	$\mathbf{T_{o,end}}$ [°C]	$\mathbf{\Delta T}$ [°C]
1	22.2	87.5	65.3
2	23.5	87.9	64.4
3	21.4	87.5	66.1
4	22.1	89.3	67.2
5	19.1	88.7	69.6
Average	21.7	88.2	66.5

Table B.14: Experimental temperature results from each experiment with a nanofluid concentration of 0.05 wt.%.

Appendix C

Temperature Development from Experimental Results

The results in the following figures are produced by the method explained in Section 3.1.4 and the data from Appendix B.

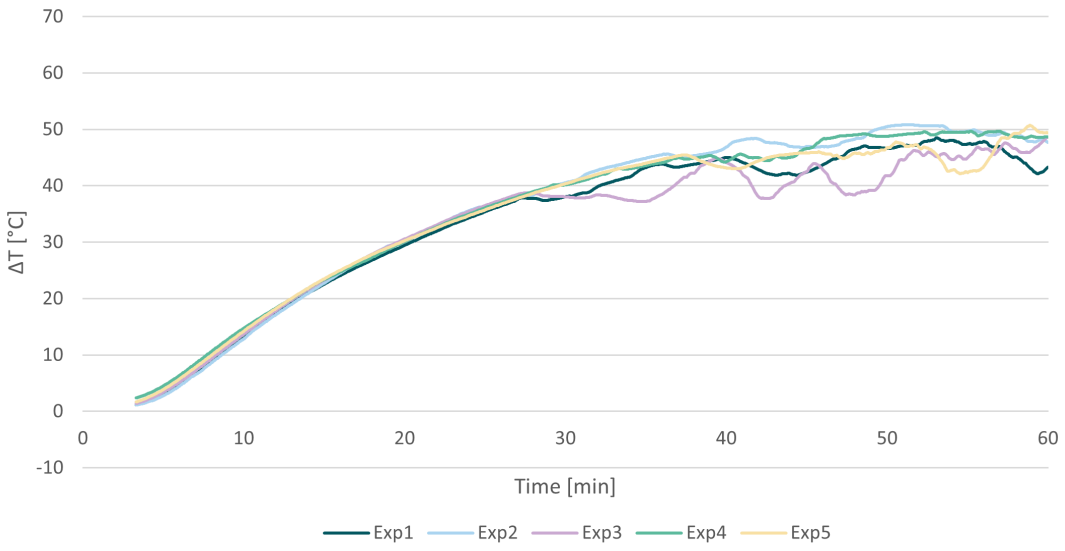

Figure C.1: Average ΔT at $H = 12$ cm for a concentration of 0.0015 wt.% for each experiment.

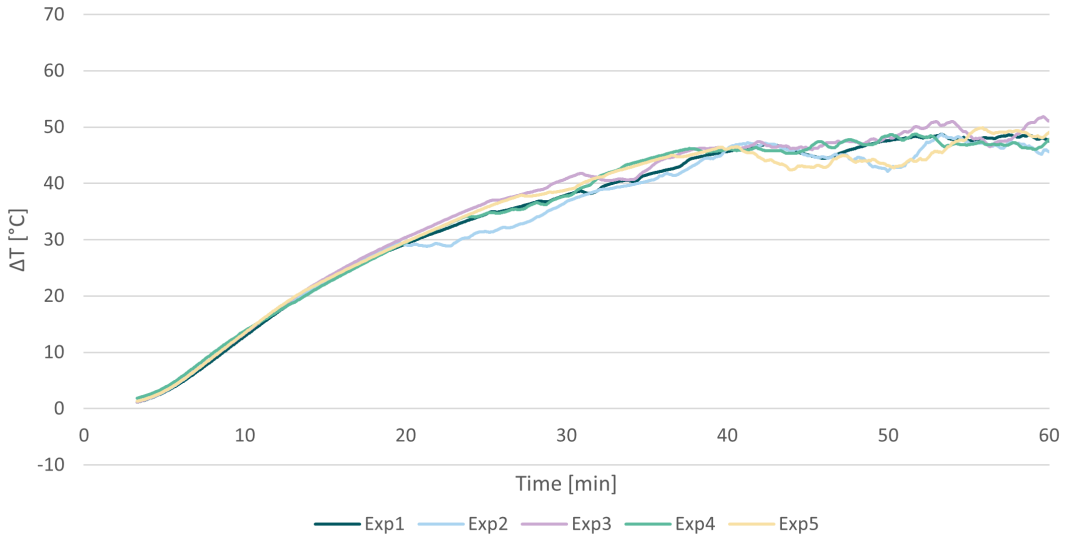

Figure C.2: Average ΔT at $H = 12$ cm for a concentration of 0.005 wt.% for each experiment.

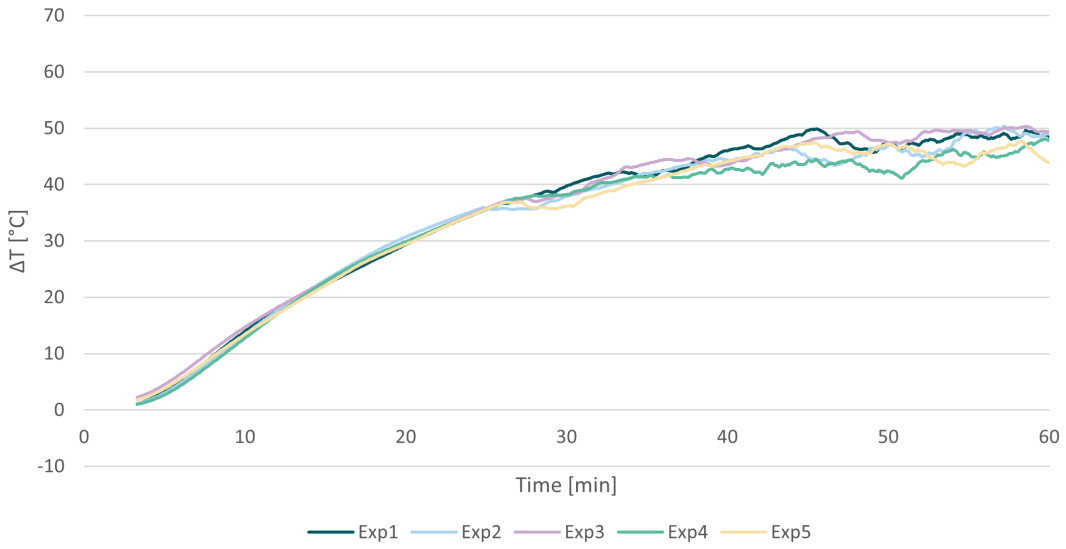

Figure C.3: Average ΔT at $H = 12$ cm for a concentration of 0.01 wt.% for each experiment.

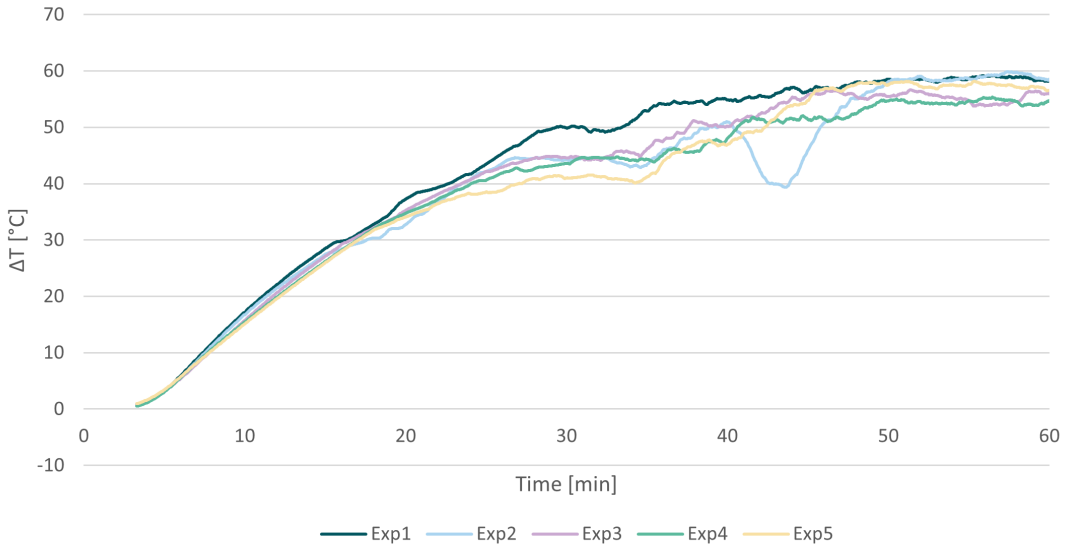

Figure C.4: Average ΔT at $H = 8$ cm for a concentration of 0.01 wt.% for each experiment.

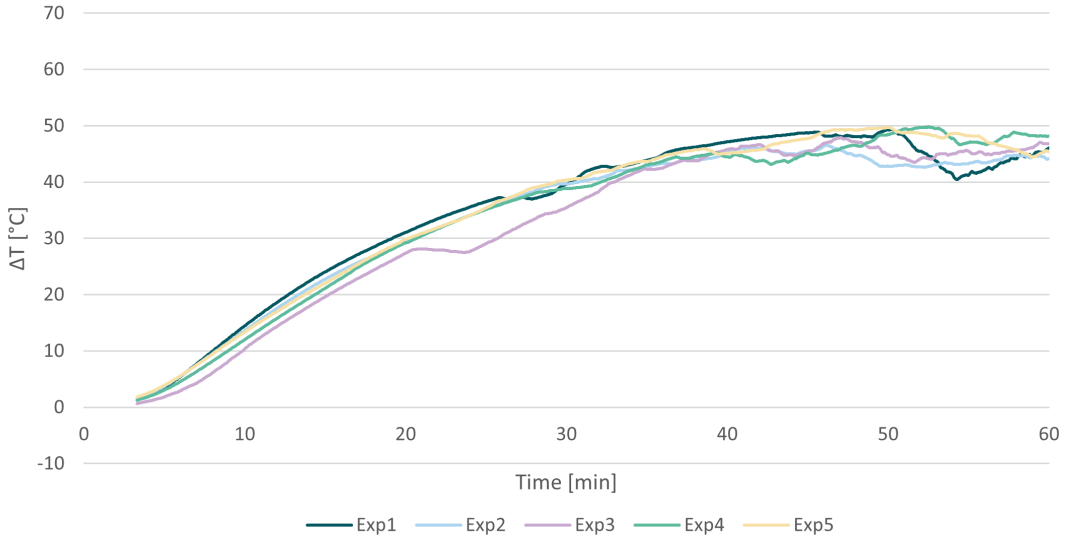

Figure C.5: Average ΔT at $H = 12$ cm for a concentration of 0.015 wt.% for each experiment.

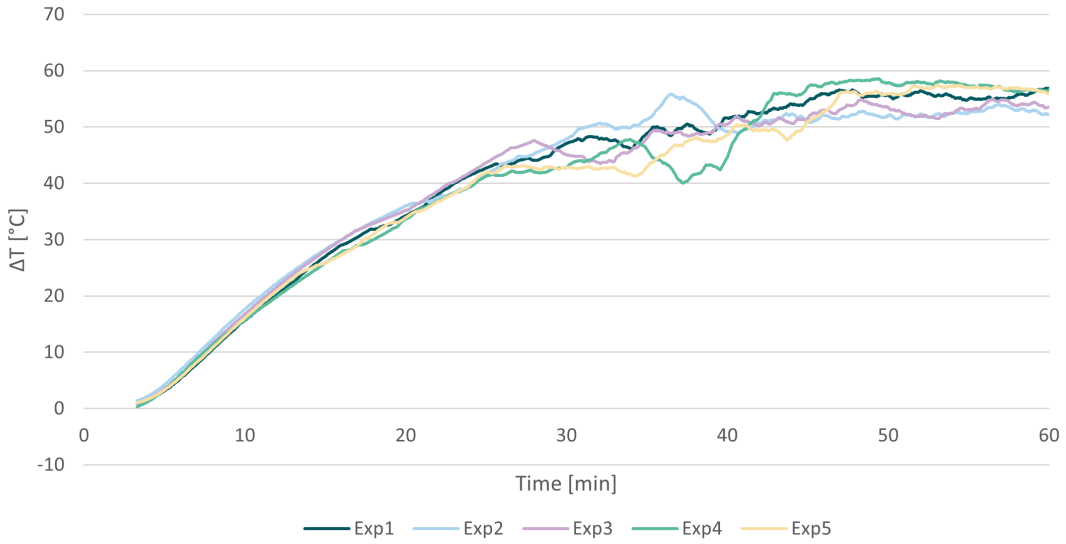

Figure C.6: Average ΔT at $H = 8$ cm for a concentration of 0.015 wt.% for each experiment.

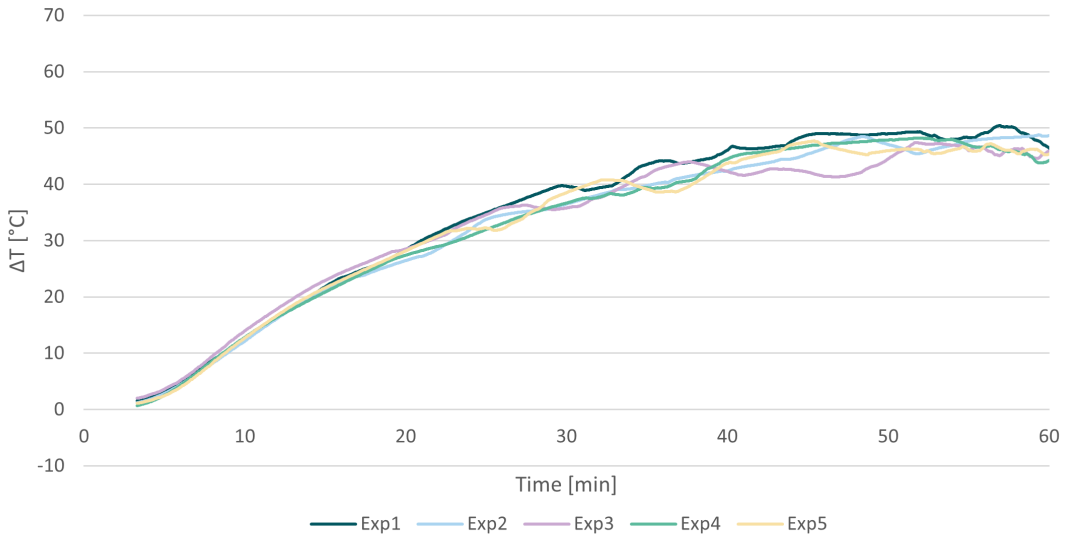

Figure C.7: Average ΔT at $H = 12$ cm for a concentration of 0.02 wt.% for each experiment.

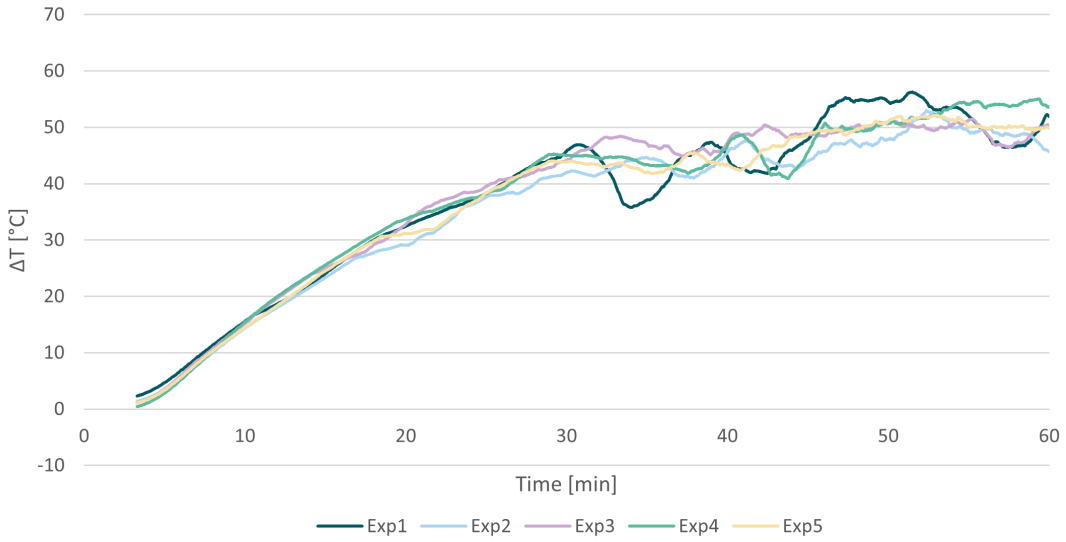

Figure C.8: Average ΔT at $H = 8$ cm for a concentration of 0.02 wt.% for each experiment.

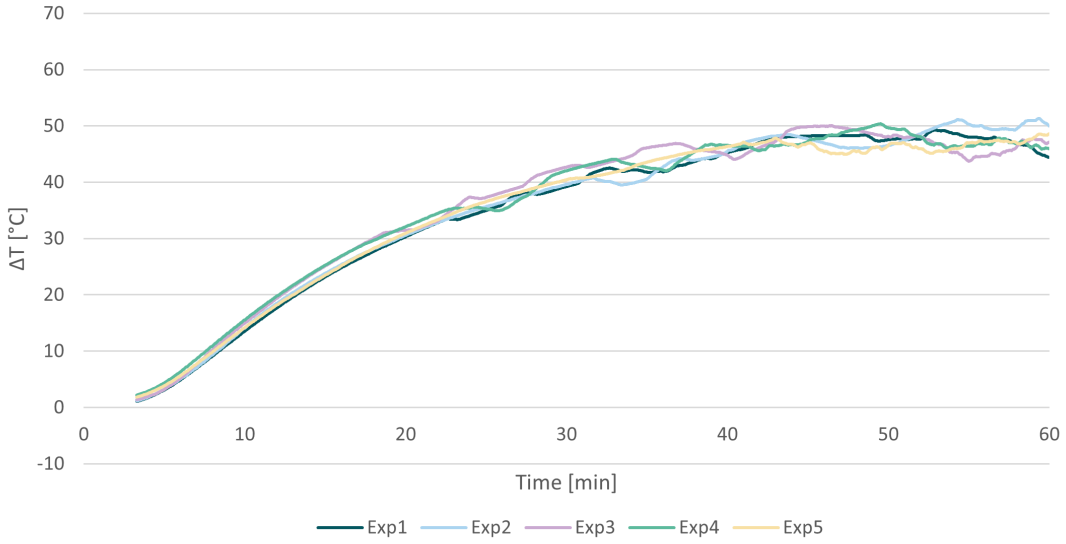

Figure C.9: Average ΔT at $H = 12$ cm for a concentration of 0.05 wt.% for each experiment.

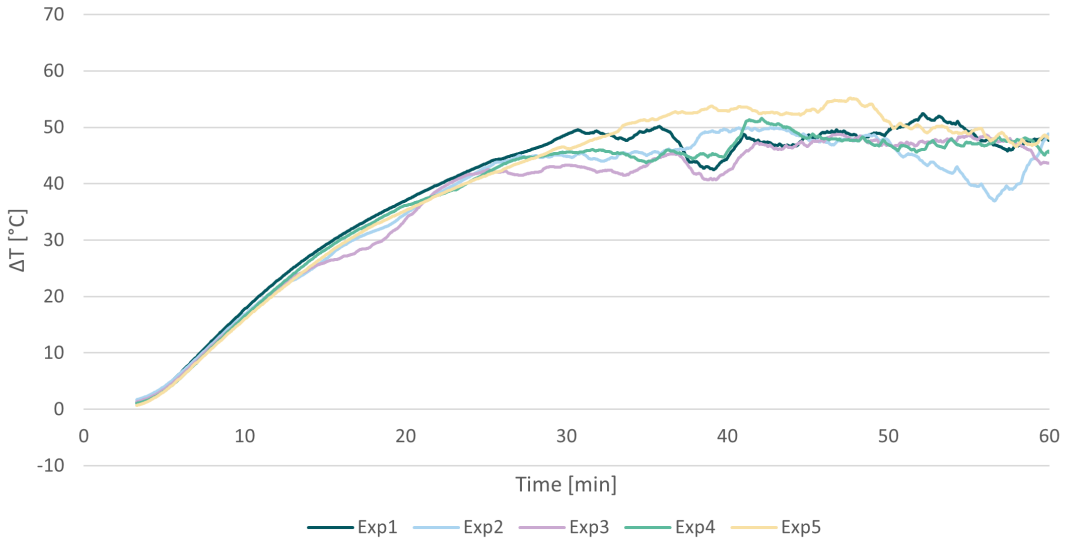

Figure C.10: Average ΔT at $H = 8$ cm for a concentration of 0.05 wt.% for each experiment.

Appendix D

Summary of Average Outlet Temperature

Fig. D.1 and D.2 present the average outlet temperature of each experiment.

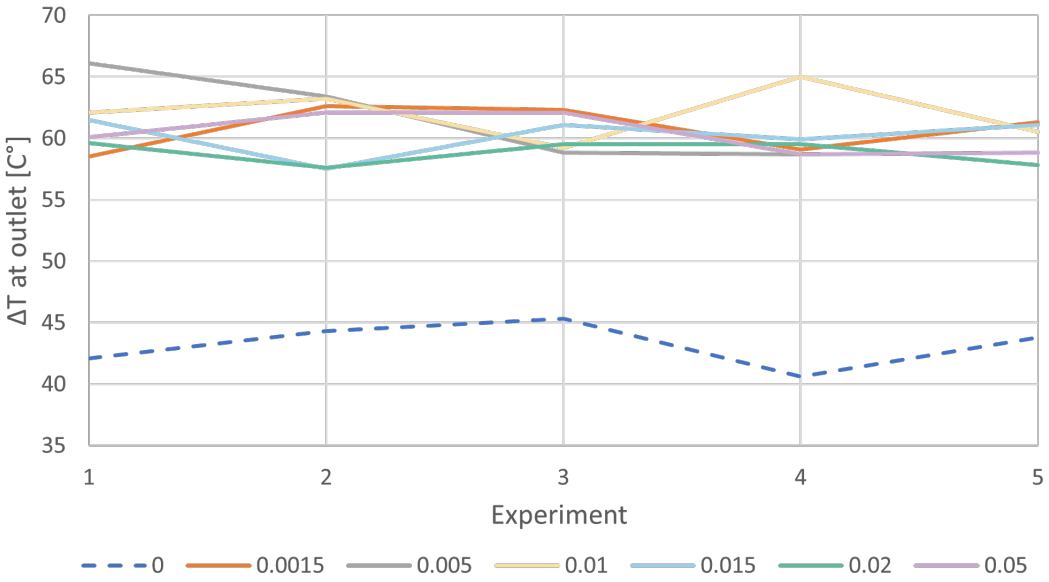

Figure D.1: Temperature difference, ΔT at the outlet after 60 minutes for $H =$ 12 cm for each experiment of the different concentrations of CB.

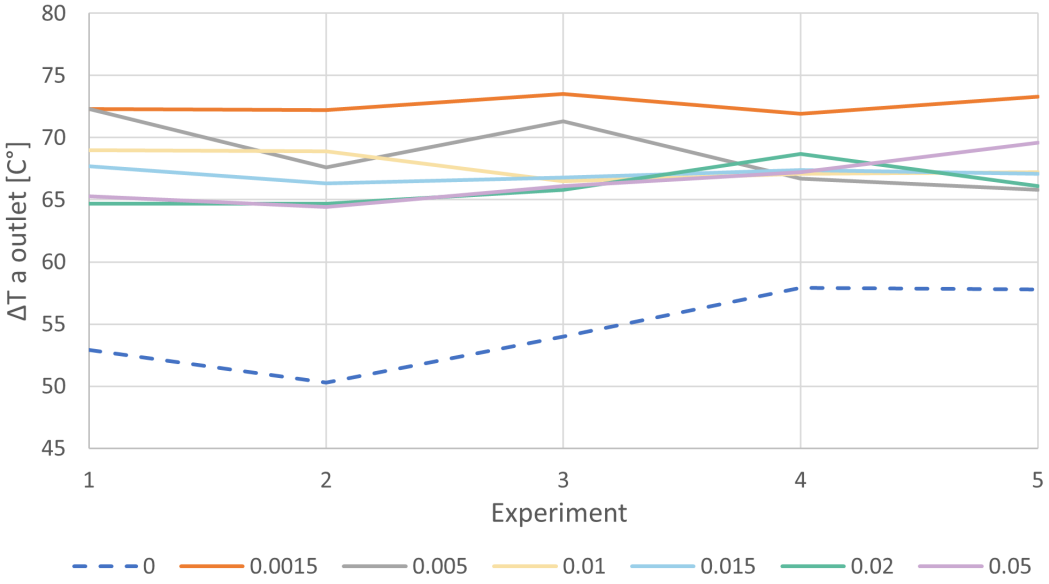

Figure D.2: Temperature difference, ΔT at the outlet after 60 minutes for $H = 8$ cm for each experiment of the different concentrations of CB.

Appendix E

Temperature Development from Numerical Analysis

The following results are produced by the method explained in Section 3.2.

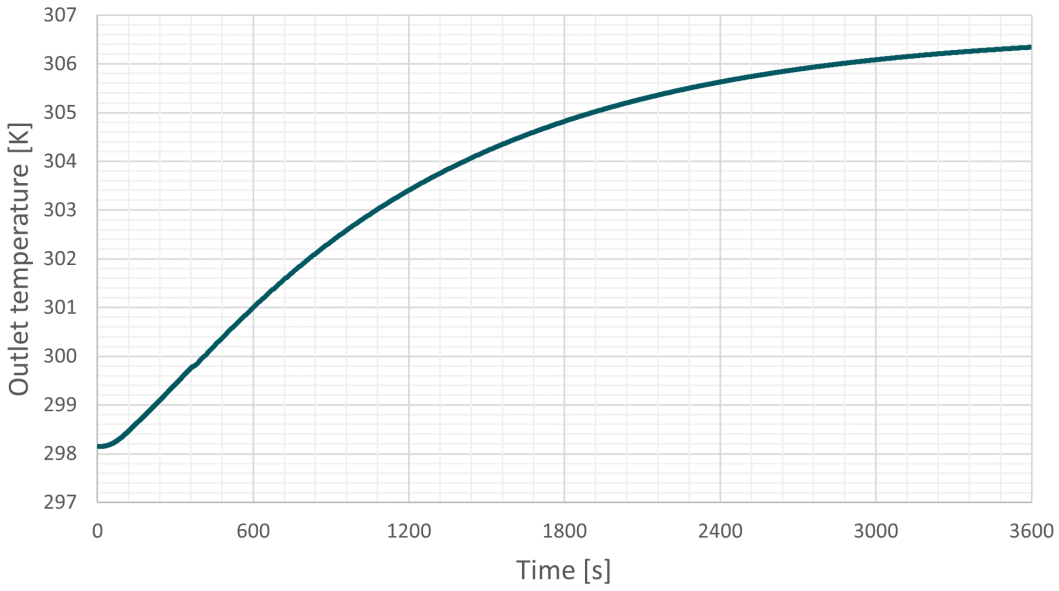

Figure E.1: Temperature development of water as a function of time.

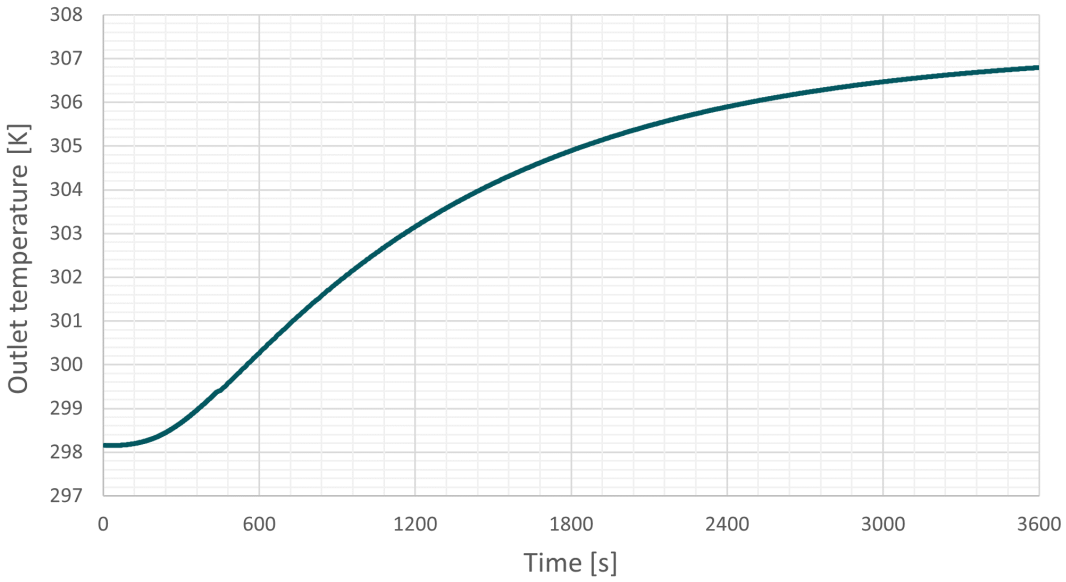

Figure E.2: Temperature development for a concentration of 0.005 wt.% as a function of time.

Appendix F

Background Data for Calculations

This section lists the most important background data for calculations.

F.1 Basic Properties

Table F.1: Background data for calculations.

Input	**Value**	**Unit**	**Reference**
Specific heat capacity, water $C_{p,bf}$	4180	J/kg K	[75]
Specific heat capacity, CB $C_{p,np}$	710	J/kg K	[54]
Density, water ρ_{bf}	997	kg/m^3	[76]
Bulk density, CB ρ_{np}	2250	kg/m^3	[54]
Bulk density, SDS ρ_{SDS}	1010	kg/m^3	[54]

Table F.1 includes the values used as a basis for further calculations. As an extension, Table F.2 lists some of the basic properties of fluids calculated based on these values by different models. The volume fraction, density, dynamic viscosity, and specific heat capacity are calculated based on Eq. (2.2), Eq. (2.1), Eq. (2.3), and Eq. (2.13), respectively.

Table F.2: Some basic properties for each fluid composition.

Fluid [wt.%]	**Volume fraction [%]**	**Density [kg/m^3]**	**Dynamic viscosity [Pa s]**	**Specific heat capacity [J/kg K]**
0	0	997.00	0.0008891	4180
0.0015	0.001	997.89	0.001047	4174
0.005	0.002	999.90	0.001402	4162
0.01	0.004	1002.57	0.001876	4145
0.015	0.007	1005.46	0.002390	4128
0.02	0.009	1008.14	0.002864	4111
0.05	0.022	1024.84	0.005828	4011

F.2 Pressure Drop and Pumping Power

The values in Table F.3 are used to calculate the pressure drop and pumping power by Eq. (2.21) and Eq. (2.29).

Table F.3: Data for pressure drop and pumping power calculations.

Input	**Value**	**Unit**	**Reference**
Dynamic Viscosity, μ	wt.% dependent	Pa s	Table F.2
Velocity, $\bar{V}$	0.003969	m/s	Calculations
Length, L	0.46	m	System dimensions
Inner diameter, D_i	0.01	m	System dimensions

F.3 Collector Efficiency and Enhancement

The values in Table F.4 are used to calculate the efficiency and enhancement by Eq. (2.25) and Eq. (2.26).

Table F.4: Data for collector efficiency and enhancement calculations.

Input	**Value**	**Unit**	**Reference**
Mass flow rate, $\dot{m}$	0.000111886	kg/s	Calculations
Specific heat capacity, C_p	wt.% dependent	kJ/kg K	Table F.2
Collector area, A_c	0.01938	m^2	System dimensions
Radiation intensity (8cm), I_0	7030	W/m^2	Section 3.1.3
Radiation intensity (10cm), I_0	6000	W/m^2	Section 3.1.3
Radiation intensity (12cm), I_0	5300	W/m^2	Section 3.1.3

Appendix G

Extinction Coefficient

Fig. G.1 and G.2 display the estimated extinction coefficient by the method explained in Section 3.1.4 for distilled water and two concentrations of nanofluids at $H = 8$ cm and $H = 12$ cm from the light source.

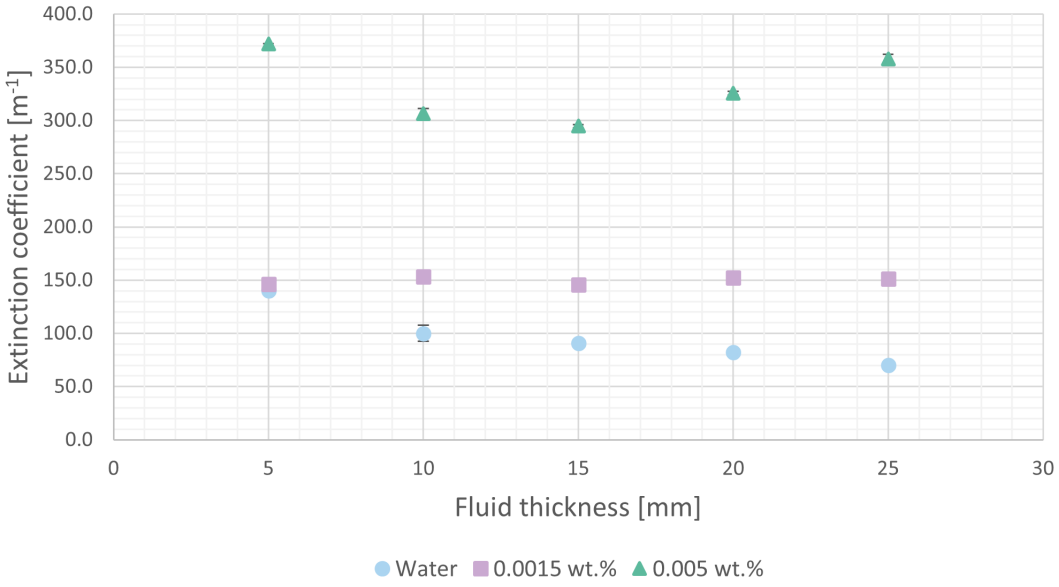

Figure G.1: The estimated extinction coefficient for water and two concentrations of carbon black nanofluids at $H = 8$ cm with error bars.

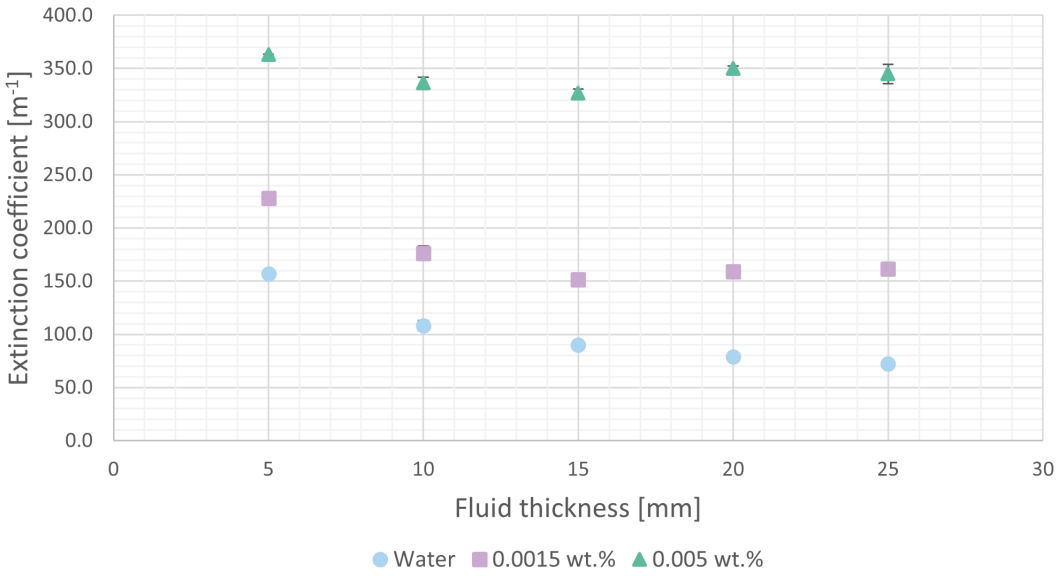

Figure G.2: The estimated extinction coefficient for water and two concentrations of carbon black nanofluids at $H = 12$ cm with error bars.

Appendix H

Light Distribution

Fig. H.1, H.2, and H.3 present the remaining results of the investigation on intensity distribution across the beam of the light source for different heights, presented in Section 3.1.3.

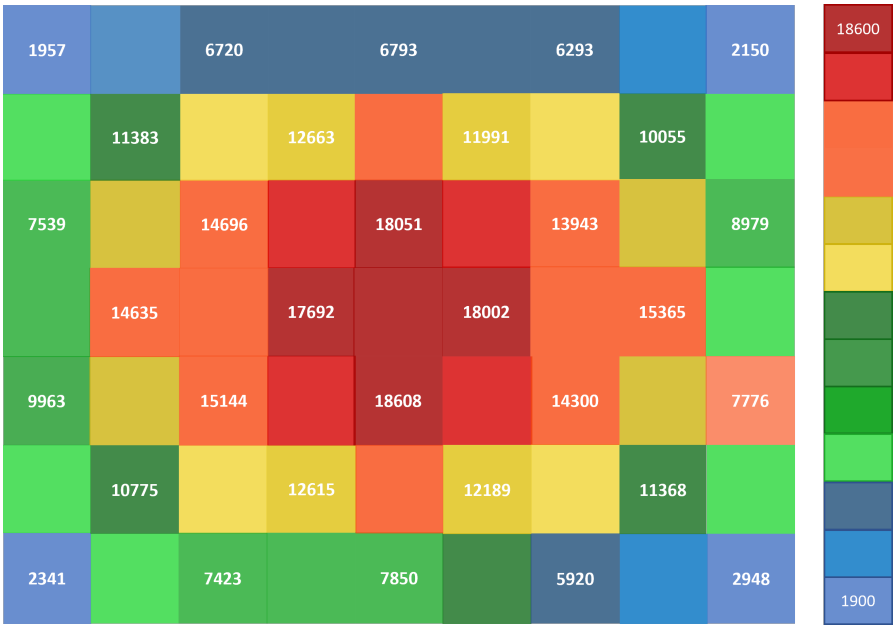

Figure H.1: Intensity distribution in [W/m^2] at a distance of 0 cm from the light source.

Figure H.2: Intensity distribution in [W/m^2] at a distance of 8 cm from the light source.

Figure H.3: Intensity distribution in [W/m^2] at a distance of 12 cm from the light source.

Appendix I

Extended Abstract Accepted at *The International Micro and Nano Flow Conference 2023*

Attached is an extended abstract with selected results from the present work. The piece was submitted and accepted for the upcoming MNF2023 conference.

Exploring the Use of Stationary Nanofluids in a Direct Absorption Solar Collector System

Agathe Bjelland Eriksen[1], Pawel Kosinski[1,*], Boris V. Balakin[2], Anna Kosinska[2]

1 Department of Physics and Technology, University of Bergen, Bergen, Norway
2 Department of Mechanical and Marine Engineering, Western Norway University of Applied Sciences, Bergen, Norway

* Corresponding author: Tel.: +47 55582817; Email: pawel.kosinski@uib.no

Abstract. The Direct Absorption Tube Solar Collector (DASC) is a commonly used device for harnessing solar radiation, which absorbs incident radiation using a heat transfer fluid containing particles. To address some of the challenges associated with pumping nanofluids, a novel system involving a stationary nanofluid located in an irradiated transparent tube was studied. Six different concentrations of carbon black were investigated, with the highest performance observed for a nanofluid concentration above 0.0015%.

Keywords: nanofluid, direct absorption solar collectors, solar energy

1. Introduction

Nanofluids (fluids containing materials of nano-sized solid particles) are used to improve the performance of solar collectors because of their favorable absorption properties. With the goal of boosting the efficiency of solar energy harvesting devices, research into the use of nanofluids is a crucial area of study [1].

The Direct Absorption Tube Solar Collector (DASC) is an effective way to harness solar radiation using a transport medium. Unlike conventional solar collectors, DASC absorbs the incident radiation directly by a heat transfer fluid containing particles [2].

The most common design involves irradiation of nanofluid as it flows. The heated nanofluid is later transferred to a heat exchanger where it releases heat to water. Nevertheless, this strategy requires pumping of nanofluids that may influence the lifetime of pumps, erosion of the piping etc. Therefore, in the present research, we studied a stationary nanofluid located in an irradiated transparent tube. The heated water passed through the nanofluid. Thus, this novel system is essentially less complex than the existing DASCs.

2. Experimental set-up

In our experiments, a two-step process for preparing nanofluids was employed. All the experiments used ENSACO 350G carbon black with an equal amount of sodium dodecyl sulfate (SDS) for stabilizing the obtained nanofluids. Both carbon black and CB were dispersed in distilled water. The mixture was stirred for 20 minutes using a magnetic stirrer, and then sonicated for 60 minutes in a Branson 3510 ultrasonic bath with the frequency of 50-60 kHz.

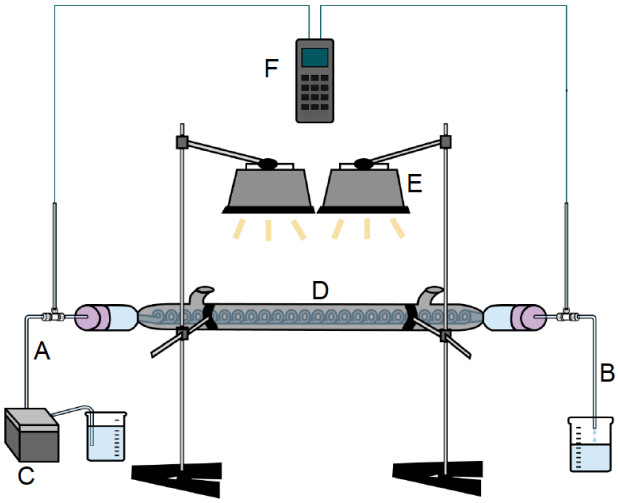

Fig. 1 Schematic of the experimental set-up

In this research, six different concentrations of carbon black were manufactured: 0.0015 wt.%, 0.005 wt.%, 0.01 wt.%, 0.015 wt.%, 0.02 wt.%, and 0.05 wt.%.
The experimental set-up is depicted in Fig. 1. The working fluid (water) was pumped through the system from point A to B using a Preciflow LAMBDA peristaltic pump (denoted as C). The flow rate was 360 ml/h.
The working fluid entered a system (denoted by D) consisting of an outer glass tube (outer diameter 38 mm, length 50 cm) filled with nanofluid, irradiated by two 400W halogen lamps (denoted by E). The distance between the glass tube and lamps was 8 or 12 cm.
This fluid was transported in an internal pipe (inner diameter 5 mm) spiraling inside the shell with a pitch of 10 mm. The coil had an external diameter of 30 mm. The absorbed heat resulted in a temperature increase of the nanofluid, which heated the working fluid. The glass shell was equipped with two openings extended by short rubber pipes for filling the system with nanofluid. This also allowed the nanofluid to freely expand due to the temperature rise. In addition, the pipes at the inlet and outlet contained T-junctions for measuring the temperatures using K-type thermocouples. For temperature logging, the Multilogger Thermometer from Omega Engineering was used (denoted as F in the figure). During the experiments, the temperatures at the inlet and outlet were recorded every 2 seconds. The experiments lasted for 60 minutes. The average room temperature was 22ºC at the experiment start.

3. Results and conclusions

At first, for illustration Figure 2 depicts the history of temperature difference between the outlet and inlet for the case where the carbon black concentration was 0.0015%. The figure presents results for five experiments.
Furthermore, Figure 3 collects all studied results and shows the final temperature difference (after 60 min, as indicated above). The figure compares the nanofluid concentration, as well as the distance between the lamps and irradiated set-up.
The first conclusion is that all the investigated nanofluids outperformed water, and the maximum performance was observed for nanofluid concentration above 0.0015%. It is interesting to note that previous findings (e.g. [3]) reported an increase in heat transfer performance for nanoparticles at an optimal concentration of 0.005%, although they focused on a different geometry with a flowing nanofluid. Therefore, their results are consistent with ours.

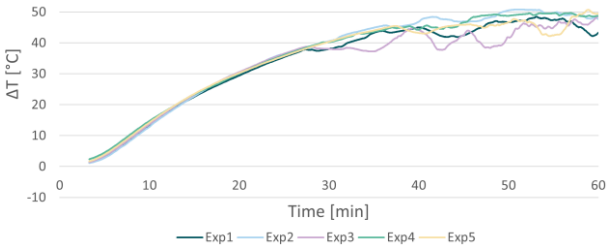

Fig. 2 History of temperature increase for carbon black concentration 0.0015% for five different experiments.

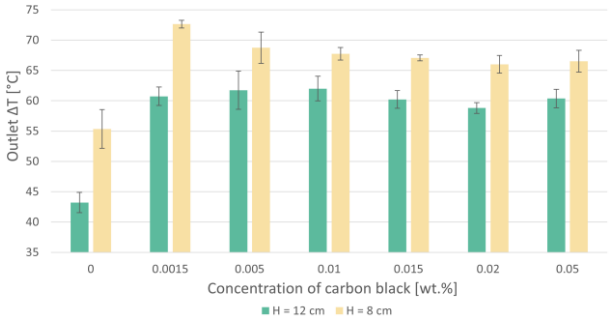

Fig. 3 The obtained temperature difference for various nanofluid concentrations and distances of the set-up from the irradiating lamps.

References

[1] A.K. Hamzat, M.I. Omisanya, A.Z. Sahin, O.R. Oyetunji, N.A. Olaitan: Energy Conversion and Management 266 (2022) 115790
[2] J.E. Minardi, H.N. Chuang: Solar Energy 17 (1975) 179–83
[3] P. G. Struchalin, V. S. Yunin, K. V. Kutsenko, O. V. Nikolaev, A. A. Vologzhannikova, M. P. Shevelyova, O. S. Gorbacheva, B. V. Balakin: International Journal of Heat and Mass Transfer 179 (2021) 12171